



저작자표시-비영리-변경금지 2.0 대한민국

이용자는 아래의 조건을 따르는 경우에 한하여 자유롭게

- 이 저작물을 복제, 배포, 전송, 전시, 공연 및 방송할 수 있습니다.

다음과 같은 조건을 따라야 합니다:



저작자표시. 귀하는 원저작자를 표시하여야 합니다.



비영리. 귀하는 이 저작물을 영리 목적으로 이용할 수 없습니다.



변경금지. 귀하는 이 저작물을 개작, 변형 또는 가공할 수 없습니다.

- 귀하는, 이 저작물의 재이용이나 배포의 경우, 이 저작물에 적용된 이용허락조건을 명확하게 나타내어야 합니다.
- 저작권자로부터 별도의 허가를 받으면 이러한 조건들은 적용되지 않습니다.

저작권법에 따른 이용자의 권리는 위의 내용에 의하여 영향을 받지 않습니다.

이것은 [이용허락규약\(Legal Code\)](#)을 이해하기 쉽게 요약한 것입니다.

[Disclaimer](#)

Doctoral Thesis

Doping and morphology engineering of hematite
photoanodes for hydrogen production

Ki-Yong Yoon

School of Energy and Chemical Engineering
(Chemical Engineering)

Ulsan National Institute of Science and Technology

2022

Doping and morphology engineering of hematite photoanodes for hydrogen production

Ki-Yong Yoon

School of Energy and Chemical Engineering
(Chemical Engineering)

Ulsan National Institute of Science and Technology

Doping and morphology engineering of hematite photoanodes for hydrogen production

A thesis/dissertation submitted to
Ulsan National Institute of Science and Technology
in partial fulfillment of the
requirements for the degree of
Doctor of Philosophy

Ki-Yong Yoon

06.20.2022 of submission

Approved by



Advisor

Ji-Hyun Jang

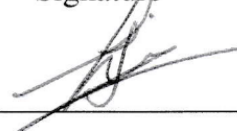
Doping and morphology engineering of hematite photoanodes for hydrogen production

Ki-Yong Yoon

This certifies that the thesis/dissertation of Ki-Yong Yoon is approved.

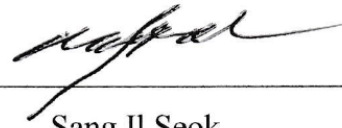
06.20.2022 of submission

Signature



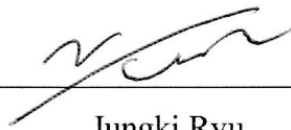
Advisor: Ji-Hyun Jang

Signature



Sang Il Seok

Signature



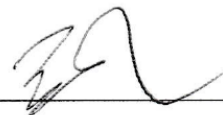
Jungki Ryu

Signature



Jun Hee Lee

Signature



Ji-Wook Jang

Abstract

The interest in hydrogen energy is rapidly increasing worldwide for developing renewable and clean energy. Among various hydrogen production methods, green hydrogen source produced by solar energy is a promising way with zero emission. Photoelectrochemical (PEC) water splitting system is widely considered as one of most promising systems to generate green hydrogen since PEC system can produce green hydrogen by using water and solar energy, and when hydrogen energy is used, it can form the most ideal energy cycle. The categories of PEC system can be broadly divided into two parts: photoanode and photocathode. We have focused photoanode part by using α -Fe₂O₃ called as hematite. Hematite is one of the cheapest materials used as a photoanode and has outstanding potential to theoretically achieve an efficiency of 15% solar-to-hydrogen (STH) conversion efficiency. In hematite-based photoanode, a variety of categories can be formed such as substrate, underlayer, overlayer, doping, oxygen evolution co-catalyst (OEC), and surface treatment. Herein, in the OEC part, we present an approach to minimize the light shielding effect by OEC in hematite surface. By successfully selectively adsorbing the developed Ti doped FeOOH (Ti-FeOOH) co-catalyst into the inner surface (inside pores) of hematite, Ti-FeOOH/Ti doped porous hematite (Ti-PH) shows a photocurrent density of 4.06 mA cm⁻² at 1.23 V vs. reversible hydrogen electrode (RHE) with good stability for 36 hours. In addition, we have focused on enhancing the performance of hematite itself and have been studying the synergy effect that can achieve structural evolution and doping through surface treatment at the same time as well as problems that may occur in the fabrication process. We cover two case of Si doping and Ge doping, respectively, and show the effects of dopants on hematite. Both cases utilize the overlayers of SiO_x and GeO₂, and Sn diffusion into hematite from the fluorine-doped tin oxide (FTO) coated glass can be suppressed when the overlayers are used. In the case of Si doping, we demonstrate the deep mechanism by which Si can be easily doped with Si and Ti interaction with efficient structural evolution. NiFeO_x coated Si and Ti co-doped hematite shows 4.3 mA cm⁻² at 1.23 V vs. RHE without any demanding fabrication process. In the case of Ge doping, we present that when Sn doping from FTO is suppressed, Ge is less affected by Sn and can make more efficient Ge doping effect. After decorating NiFeO_x co-catalyst, NiFeO_x/Ge doped porous hematite (Ge-PH) shows a photocurrent density of 4.6 mA cm⁻² at 1.23 V vs. RHE and our tandem device with a perovskite solar cell (PSC) achieves 4.8% STH efficiency. Our works suggests a straightforward way to develop efficiently doped hematite, that can be easily expanded to other doping systems for green hydrogen production.

Contents

Chapter 1. Introduction: hydrogen energy.....	1
1.1 Hydrogen: grey, blue and green hydrogen.....	1
1.2 Understanding the photoelectrochemical water splitting.....	7
1.3 Hematite ($\alpha\text{-Fe}_2\text{O}_3$): promising n-type semiconductor for PEC water oxidation	11
1.4 References	21
Chapter 2. Porous hematite synthesis with Ti doped FeOOH OER co-catalyst for efficient photoelectrochemical water splitting system.....	26
2.1. Introduction	26
2.2 Experimental section	29
2.2.1 Fabrication of Ti-H photoanode	29
2.2.2 Fabrication of Ti-PH photoanode.....	29
2.2.3 Fabrication of FeOOH decorated Ti-PH or Ti-FeOOH decorated Ti-PH photoanode..	29
2.2.4 PEC measurements.....	29
2.3 Results and Discussion	30
2.4 Conclusion	48
2.5 References	49
Chapter 3. Insight into the dopability of hematite photoanode for an efficient water splitting ..	52
3.1 Introduction	52
3.2 Experimental section	53
3.2.1 Fabrication of Si- Fe_2O_3 or Si:Ti- Fe_2O_3 electrodes	53
3.2.2 Fabrication of NiFeO _x coated Si:Ti- Fe_2O_3 electrodes	53
3.2.3 PEC measurements.....	53
3.2.4 DFT calculation details.....	53
3.3 Results and Discussion	55
3.4 Conclusion	81
3.5 References	82
Chapter 4. NiFeO_x decorated Ge-hematite/perovskite for an efficient tandem water splitting system.....	85
4.1 Introduction	85
4.2 Experimental section	86
4.2.1 Fabrication of Fe_2O_3 and Ge doped hematite (Ge-H) photoanode	86

4.2.2 Fabrication of Ge doped porous hematite (Ge-PH) photoanode	86
4.2.3 Fabrication of NiFeO _x decorated Ge-PH photoanode	86
4.2.4 PEC measurements	86
4.2.5 Synthesis of methylammonium iodide (MAI).....	87
4.2.6 Synthesis of FAPbI ₃ and MAPbBr ₃ powders.....	87
4.2.7 Photovoltaic device fabrication	87
4.2.8 DFT calculation details.....	88
4.3 Results and Discussion	90
4.4 Conclusion	107
4.5 References	108
Publication list.....	111
Acknowledgment.....	112

List of Figures

Figure 1.1. Comparison of (a) specific energy and (b) energy density for various energy sources.

Figure 1.2. The schematic image for grey, blue, and green hydrogen production systems.

Figure 1.3. Schematic image of water electrolysis with advantages and disadvantages. (b) Schematic image of needed energy for OER and HER reaction of theoretical and actual catalysts. (c) Energy needed for water splitting and alternative energy sources.

Figure 1.4. Various energy resources existing on Earth.

Figure 1.5. Photoelectrochemical water splitting system for green hydrogen production using solar energy and water and the necessary factors to improve the system efficiency.

Figure 1.6. Various semiconductor candidates for photoelectrochemical water splitting.

Figure 1.7. Energy diagram for hematite-based photoelectrochemical water splitting and Idealized LSV curve and current state for photoelectrochemical water oxidation of n-type hematite semiconductor.

Figure 1.8. Overview of the main categories of hematite-based photoelectrochemical water splitting.

Figure 1.9. (a) Schematic image for the fabrication of hematite on patented FTO (p-FTO) substrate. (b) Linear sweep voltammetry curves of Fe_2O_3 on FTO or p-FTO substrate. (c) Schematic image for the fabrication of 3D FTO substrate by PS assembly. (d). UV-Vis absorption of 3D-NFG, Fe_2O_3 and $\text{Fe}_2\text{O}_3/\text{GIO}$.

Figure 1.10. (a) Schematic image for underlayer mechanism for hematite photoanode and linear sweep voltammetry curves of Fe_2O_3 with various underlayers. (b) Schematic configuration for underlayer. (c) SPV measurements and band diagram.

Figure 1.11. (a) Schematic image for fabrication of TiO_2 overlayer coated hematite photoanode. (b) Linear sweep voltammetry curves of Fe_2O_3 w/wo TiO_2 overlayer. Chemical Society. (b) Schematic image for fabrication process utilizing Nb_2O_5 overlayer on hematite and SEM, TEM, HAADF, and EDX mapping images for hematite using Nb_2O_5 overlayer.

Figure 1.12. (a) Schematic image for improving the interface between $\text{NiFe}(\text{OH})_x$ and hematite by citrate and linear sweep voltammetry curves of Fe_2O_3 and $\text{NiFe}(\text{OH})_x$ coated Fe_2O_3 w/wo citrate treatment. (b) Schematic images of the kinetic process for pristine Fe_2O_3 , heterogenized molecular Ir catalyst coated Fe_2O_3 , IrO_2 co-catalyst coated Fe_2O_3 .

Figure 1.13. Electrolyte-dependent OER mechanism for red step of basic electrolyte and green step of acidic electrolytes. The black arrows indicates that the overall OER mechanism by four steps and blue steps are two adjacent oxo for M–O intermediates for oxidation process.

Figure 2.1. Schematic images for various approaches to fabricate hematite electrode and the comparison of productivity and fabrication cost of various technologies.

Figure 2.2. Schematic images for representative hydrothermal method for hematite electrode.

Figure 2.3. (a) Schematic image for preparation of hematite for Ti doping (Ti-H), porous hematite with Ti doping (Ti-PH), FeOOH coated porous hematite with Ti doping (FeOOH/Ti-PH), and Ti-FeOOH coated porous hematite with Ti doping (Ti-FeOOH/Ti-PH). Scanning electron microscopy (SEM) and transmission electron microscopy (TEM) images of Ti-PH (first column, (b, e and h)), FeOOH/Ti-PH (second column, (c, f and i)), and Ti-FeOOH/Ti-PH (third column, (d, g and j)). (b–d) SEM images of three types of photoanode. (e–g) TEM images of a nanorod of three types of photoanode, respectively. The inset images in (b–g) are the zoomed-in images of the rectangle region. (h–j) The zoomed-in images of the inner pore sites in three photoanodes.

Figure 2.4. (a) SEM image and (b) TEM image of Ti doped hematite. The insert image is the zoomed-in image of the dotted rectangle region. Cross-sectional SEM images of (c) Ti doped FeOOH and (d) Ti doped hematite.

Figure 2.5. Comparison of SEM images by different heat treatment conditions. The time of heat treatment increases from left to right whereas the temperature of heat treatment increases from top to bottom, as shown by the arrows. (a–c) Ti doped porous hematite prepared with various time conditions for 5, 10, and 20 min at fixed temperature (650 °C). (d–f) Ti doped porous hematite made with various time conditions for 5, 10, and 20 min at fixed temperature (750 °C). (g–i) Ti doped porous hematite arranged with various time conditions for 5, 10, and 20 min at fixed temperature (850 °C). Pore generations were observed in (f), (h), and (i), where the electrodes suffered harsh conditions to make enough pressure inside hematite by water vapor.

Figure 2.6. Comparison of SEM images of (a) FeOOH loaded Ti doped hematite and (b) FeOOH loaded Ti doped porous hematite. Two electrodes were made by same condition by using 1.5 mM FeCl₃. The comparison of TEM images of (c) FeOOH loaded Ti doped hematite and (d) FeOOH loaded Ti-PH. LSV curves under 1 SUN condition in the basic electrolyte (1 M NaOH) of (e) FeOOH loaded Ti doped hematite and (f) FeOOH loaded Ti doped porous hematite.

Figure 2.7. XPS spectra of O1s. (a) of Ti-FeOOH film on FTO glass, Ti-H without SiO_x overlayer, Ti-FeOOH/Ti-H, and TiFeOOH/SiO_x/Ti-H. (b) Deconvolution peaks of O 1s peaks to confirm the relative portion of O²⁻, OH⁻, and adsorbed water. UV-Vis spectra for light shielding effect. (c) Ti-FeOOH/Ti-H and (d) Ti-FeOOH/SiO_x/Ti-H. TEM images of (e) Ti-FeOOH/Ti-H and (f) Ti-FeOOH/SiO_x/Ti-H.

Figure 2.8. Various TEM images to confirm the selective deposition of FeOOH and Ti-FeOOH co-catalyst on outer and inner surface of Ti-PH.

Figure 2.9. Comparison of statistic data for the size distribution of FeOOH co-catalyst nanoparticles on

a) outer and b) inner surface of Ti-PH and the size distribution of Ti-FeOOH nanoparticles on c) outer and d) inner surface of Ti-PH.

Figure 2.10. Electrical conductivity measurements by (a) FeOOH and (b) Ti-FeOOH powders.

Figure 2.11. (a) Ti 2p peaks and (b) O 1s peaks of FeOOH/Ti-PH and Ti-FeOOH/Ti-PH.

Figure 2.12. Comparison of LSV curves of each photoanode in 1M NaOH under (a) light and (b) dark conditions. (c) Electrochemical impedance spectroscopy (EIS) curves at 1.23 V vs. RHE. (d) Stability test with chopped light conditions at 1.23 V vs. RHE. (e) IPCE spectra for each sample measured at 1.23 V vs. RHE. (f) Normalized UV-Vis absorption spectrum.

Figure 2.13. Faradaic efficiency of Ti-FeOOH/Ti-PH at 1.23 V vs RHE under AM 1.5 illumination in a 1 M NaOH electrolyte.

Figure 2.14. (a) LSV curves in 1M NaOH under the dark condition. For same concentration of FeOOH and Ti-FeOOH, film type electrode was made on FTO substrate. (b) Zeta potential measurement. (c) Scheme of the OER mechanism by FeOOH and Ti-FeOOH.

Figure 2.15. Long-term stability of Ti-FeOOH/Ti-PH.

Figure 2.16. (a) LSV curves with various co-catalyst and (b) long-term stability with representative co-catalyst loaded on Ti-PH. Schematic images to the light absorption by co-catalyst and light shielding effect of (c) Co-Pi or IrO₂ deposited Ti-PH and (d) Ti-FeOOH/Ti-PH.

Figure 3.1. (a) Schematic images for two strategies for consideration of Si doping with and without Ti dopant. Comparison of SEM and TEM images for (b) Si doped hematite by SiO_x layer and (c) Si and Ti co-doped hematite by SiO_x layer. (d) Linear sweep voltammetry (LSV) curves with and without Ti dopant. LSV measurement was conducted in basic electrolyte (1 M NaOH solution). The LSV curves measured in the dark condition are indicated by dotted lines. (e) Comparison of tau plots calculated from the UV-Vis spectra of four types of hematite. (f) Comparison of incident-photon-to-current efficiency (IPCE) spectra of Si doped hematite by SiO_x layer and Si and Ti co-doped hematite by SiO_x layer.

Figure 3.2. Scheme for photoanode fabrication of Fe₂O₃ and Ti doped Fe₂O₃. TEM images of (b-I) FeOOH, (b-II) Fe₂O₃, (c-I) Ti doped FeOOH and (c-II) Ti-Fe₂O₃.

Figure 3.3. Comparison of Fe₂O₃ annealed at 850 °C and 550 °C, and Si-Fe₂O₃ and Si and Ti doped Fe₂O₃ annealed at 850 °C. SEM images of (a) Fe₂O₃ annealed at 850 °C, (b) Fe₂O₃ annealed at 550 °C and (c) Si doped Fe₂O₃ (d) Si and Ti doped Fe₂O₃ annealed at 850 °C. The upper image is hematite grown on FTO and the lower image is the power hematite. (e) N₂ adsorption-desorption isotherms of four kinds of Fe₂O₃. The BET surface area of each Fe₂O₃ is 2 m²/g (Fe₂O₃, 850 °C), 5 m²/g (Fe₂O₃, 550 °C), 9 m²/g (Si doped Fe₂O₃, 850 °C) and 12 m²/g (Si and Ti co-doped Fe₂O₃, 850 °C). The pore distribution of (f) Fe₂O₃ (850 °C), (g) Fe₂O₃ (550 °C), (h) Si doped Fe₂O₃ (850 °C) and (g) Si and Ti co-doped Fe₂O₃ (850 °C).

Figure 3.4. Comparison of (a) UV-Vis spectra and (b) Achieved photocurrent density with band gap. (c) Comparison of the achieved photocurrent density with the theoretically achievable values based on band gap to utilize theoretical photocurrent density by Shockley and Queisser.

Figure 3.5. (a) Atomic arrangements for (a-I) Fe_2O_3 and (a-II) Si doped Fe_2O_3 without Ti dopant. (b) Atomic arrangements for (b-I) Ti doped Fe_2O_3 and (b-II) Si and Ti co-doped Fe_2O_3 . (c) Comparison of formation energy for effect of Ti dopant on Si doping with representative Sn doping into hematite. The black dotted line is the formation energy values at 1100k temperature and 1 atmosphere closest to the experimental condition. (d) Comparison of crystal-orbital overlap population (COOP) for the Fe atoms in (d-I) Si doped hematite and (d-II) Si and Ti co-doped hematite. Yellow arrows indicate charge repulsion between Fe atoms.

Figure 3.6. (a) Schematic images of the Sn distribution during hematite fabrication process w/wo the SiO_x layer. (b) The comparison of XPS spectra of Sn $3d$ and (c) Sn content.

Figure 3.7. The formation energy of Fe_2O_3 for Si doping in a $2 \times 2 \times 1$ supercell. The PEC activity of Si-doped Fe_2O_3 w/wo Ti-dopant by considering the interaction of the Sn dopant with the other two dopants (Si or Ti) by controlling the annealing temperature: (b) Si and Sn co-doped Fe_2O_3 and (c) Si, Ti, and Sn co-doped Fe_2O_3 .

Figure 3.8. (a) Si distribution diagram by three-dimensional TOF-SIMS of (SiO_x coated Ti-FeOOH film) and after high temperature annealing process (Si and Ti co-doped Fe_2O_3 film) and (b) comparison of Si distribution by depth profiles of TOF-SIMS. TEM images of (c-I) SiO_x coated FeOOH, (c-II) Si doped Fe_2O_3 , (d-I) SiO_x coated Ti-FeOOH, and (d-II) Si and Ti co-doped Fe_2O_3 . High resolution TEM images of (e) Si doped Fe_2O_3 and (f) Si and Ti co-doped Fe_2O_3 by removing SiO_x layer. (g) XRD patterns of Fe_2O_3 , Ti doped Fe_2O_3 , Si doped Fe_2O_3 , and Si and Ti co-doped Fe_2O_3 . The Inset images are compared results by normalizing. (h) Raman spectra of Fe_2O_3 , Ti doped Fe_2O_3 , Si doped Fe_2O_3 , and Si and Ti co-doped Fe_2O_3 . The Inset images are compared results by normalizing. Comparison of XPS spectra for (i) Ti 2p for Ti effect and (j) Si 2p for the Si doping.

Figure 3.9. The XPS depth profiles of Si and Ti co-doped Fe_2O_3 without the SiO_x layer for Si content.

Figure 3.10. (a) Zoomed-in XRD patterns of Fe_2O_3 , Ti doped Fe_2O_3 , Si doped Fe_2O_3 , and Si and Ti co-doped Fe_2O_3 and (b) Lattice parameter calculated from XRD patterns.

Figure 3.11. STEM-EDX elemental distribution of (a) Fe_2O_3 , (b) Ti doped Fe_2O_3 , (c) Si doped Fe_2O_3 and (d) Si and Ti co-doped Fe_2O_3 .

Figure 3.12. XPS spectra of Si 2p of (a) SiO_x coated Fe_2O_3 , (b) Si doped Fe_2O_3 , (c) SiO_x coated Ti- Fe_2O_3 and (d) Si and Ti doped Fe_2O_3 before and after etching the SiO_x layer.

Figure 3.13. (a) Density of surface states (DOSS) by PEIS measurements in different applied potential range. (b) Mott-Schottky plots for charge density of each sample. (c) Charge transfer efficiency by

calculating PEIS results. (d) Charge separation efficiency by hole scavenger system. Transient photocurrent behavior with (e) Si doped Fe_2O_3 and (f) Si and Ti co-doped Fe_2O_3 at $1.23 V_{\text{RHE}}$.

Figure 3.14. (a) The EIS circuit of hematite photoanodes under dark conditions. The comparison of Nyquist plots of (b) Fe_2O_3 , (c) Ti doped Fe_2O_3 , (d) Si doped Fe_2O_3 and (e) Si and Ti co-doped Fe_2O_3 .

Figure 3.15. (a) The PEIS circuit of hematite photoanodes under light illumination. The comparison of Nyquist plots of (b) Fe_2O_3 , (c) Ti doped Fe_2O_3 , (d) Si doped Fe_2O_3 and (e) Si and Ti co-doped Fe_2O_3 .

Figure 3.16. The PEIS circuit parameters by fitting PEIS data for Fe_2O_3 , Ti doped Fe_2O_3 , Si doped Fe_2O_3 and Si and Ti co-doped Fe_2O_3 in 1 M NaOH electrolyte under light condition. (a) R_{trapping} , (b) $R_{\text{ct,trap}}$ and (c) C_{trap} in different applied potential.

Figure 3.17. The comparison of the electrical conductivity for all samples.

Figure 3.18. (a) LSV curves in a 1 M NaOH electrolyte (solid lines) and a 1M NaOH with 0.1 M Na_2SO_3 (dashed lines) electrolyte under light conditions. (b) The comparison of the current densities at below $0.9V_{\text{RHE}}$

Figure 3.19. LSV curves of (a) Ti doped Fe_2O_3 and (b) Si and Ti co-doped Fe_2O_3 by injecting different Ti contents (Ti X = X μL of TiCl_3 in 100 mL of 150 mM FeCl_3). (c) Comparison of PEC efficiency by different Ti concentration at $1.23 V_{\text{RHE}}$. (d) LSV curves after loading NiFeO_x on Si:Ti- Fe_2O_3 . (e) Long-term stability test for NiFeO_x decorated Si and Ti co-doped Fe_2O_3 at $1.23 V_{\text{RHE}}$. (f) Faradaic efficiency of $\text{NiFeO}_x/\text{Si:Ti-Fe}_2\text{O}_3$ at $1.23 V_{\text{RHE}}$.

Figure 3.20. (a) A schematic illustration of a band diagram w/wo a NiFeO_x catalyst. (b) Comparison of open circuit potentials of Si and Ti co-doped Fe_2O_3 and NiFeO_x coated Si and Ti co-doped Fe_2O_3 . (c) Comparison of LSV curves for Si and Ti co-doped Fe_2O_3 and NiFeO_x coated Si:Ti- Fe_2O_3 in dark conditions.

Figure 3.21. LSV curves of (a) Fe_2O_3 , (b) Ti doped Fe_2O_3 , (c) Si doped Fe_2O_3 , (d) Si and Ti co-doped Fe_2O_3 and (e) NiFeO_x coated Si:Ti- Fe_2O_3 confirming the reproducibility of samples. (f) Statistical PEC performance data of samples at $1.23 V_{\text{RHE}}$.

Figure 3.22. LSV curves with an active area of (a) 0.50 cm^2 and (b) 1.00 cm^2 . (c) The comparison of FTO resistance before and after $850 \text{ }^\circ\text{C}$ annealing for 20 min. (d) Table for the current density of each sample at $1.23 V_{\text{RHE}}$ according to the active area.

Figure 4.1. (a) Schematic images for Ge doping strategy. (b) top-view and cross-sectional SEM and TEM images for (b) Fe_2O_3 , (c) Ge-H and (d) Ge-PH. (e) Scanning transmission electron microscopy (STEM) image of Ge-PH and the corresponding mapping element of (f) Fe, (g) O, (h) Ge and (i) Sn.

Figure 4.2. The top-view (a-1 and b-1) and cross-sectional (a-2 and b-2) SEM images and a TEM image (a-3 and b-3) of (a) FeOOH nanorod and (b) Ge-doped FeOOH nanorod.

Figure 4.3. (a) STEM image of the entire $\text{GeO}_2/\text{FeOOH}$ nanorod and the corresponding elemental mapping image of (b) Fe, (c) O, (d) Ge, (e) Sn and (f) C.

Figure 4.4. (a) LSV curves of Fe_2O_3 , nonporous Fe_2O_3 with Ge doping (Ge-H), and porous Fe_2O_3 with Ge doping (Ge-PH) in basic electrolyte (1 M NaOH (pH = 13.6)) under 1 SUN illumination. (b) XRD patterns of Fe_2O_3 , nonporous Fe_2O_3 with Ge doping (Ge-H), and porous Fe_2O_3 with Ge doping (Ge-PH) and (c) Raman spectra of Fe_2O_3 , nonporous Fe_2O_3 with Ge doping (Ge-H), and porous Fe_2O_3 with Ge doping (Ge-PH). XPS signals for (d) Ge 3d of Fe_2O_3 , nonporous Fe_2O_3 with Ge doping (Ge-H), and porous Fe_2O_3 with Ge doping (Ge-PH), and (e) Sn 3d of Fe_2O_3 , nonporous Fe_2O_3 with Ge doping (Ge-H), and porous Fe_2O_3 with Ge doping (Ge-PH). (f) Fourier transform of the EXAFS data at the Fe k-edge of the hematite nanostructures in Fe_2O_3 , nonporous Fe_2O_3 with Ge doping (Ge-H), and porous Fe_2O_3 with Ge doping (Ge-PH). The depth profiles by XPS measurements for (g) Sn and (h) Ge contents. (i) Calculated Sn:Ge doping ratio.

Figure 4.5. SEM and TEM images of porous hematites with (a) Sn, (b) Ti, and (c) Si doping. (d) PEC efficiency for various doped porous hematites and (e) N_2 adsorption-desorption isotherms of each sample. The BET surface area of each sample is around $10 \text{ m}^2/\text{g}$. (f) The ECSA values of each photoanode. (g) XRD patterns of each sample and (h) the zoom-in image of XRD patterns for (110) and (300) plane.

Figure 4.6. XPS spectra of Ge 3d for (a) GeO_2 , (b) Ge-H and (c) Ge-PH.

Figure 4.7. The photoelectrochemical performance of Ge-H according to the amount of different Ge precursors in 100 ml of 150 mM FeCl_3 .

Figure 4.8. XANES spectra of Fe_2O_3 , Ge-H and Ge-PH.

Figure 4.9. Calculated (Sn+Ge)/Fe ratio by XPS depth profiles

Figure 4.10. SEM images of (a) Fe_2O_3 , (b) Sn_{100} ($\text{Ge}_0:\text{Sn}_{100}$ -hematite), (c) $\text{Ge}_{25}\text{Sn}_{75}$ ($\text{Ge}_{25}:\text{Sn}_{75}$ -hematite), (d) $\text{Ge}_{50}\text{Sn}_{50}$ ($\text{Ge}_{50}:\text{Sn}_{50}$ -hematite), (e) $\text{Ge}_{75}\text{Sn}_{25}$ ($\text{Ge}_{75}:\text{Sn}_{25}$ -hematite), (f) Ge_{100} ($\text{Ge}_0:\text{Sn}_{100}$ -hematite). (g) N_2 adsorption-desorption isotherms of each sample. The BET surface area of each sample is around $2 \text{ m}^2/\text{g}$. (h) The pore size distribution in Fe_2O_3 , Ge-H, and Ge-PH. (i) J-V curves of Sn-doped, Ge-doped, and Ge:Sn co-doped hematite prepared at low temperature ($550 \text{ }^\circ\text{C}$).

Figure 4.11. (a) Calculated formation energies of various dopants (Sn, Ge, and co-doped Ge and Sn) into hematite. The dotted line is the energy standard that matches the experimental conditions. (b) atomic structures of Fe_2O_3 , Ge doped Fe_2O_3 , and Ge and Sn co-doped Fe_2O_3 . by DFT calculations. (c) Atomic arrangements of ideal Fe_2O_3 , Ge doped Fe_2O_3 Sn doped Fe_2O_3 and Ge and Sn co-doped Fe_2O_3 . (d) Fe 2p signals by XPS measurement. (e) The process of Sn doping from FTO and the mechanism by which Ge and Sn exist together.

Figure 4.12. (a) Mott-Schottky measurements of Fe_2O_3 , Ge doped Fe_2O_3 and Ge and Sn co-doped Fe_2O_3 . and (b) Nyquist plot. inset image is the circuit model. (c) Free energy diagrams of the intermediates on ideal Fe_2O_3 and ideal Ge doped Fe_2O_3 . Hematite (0001) surface was used for accurate comparison with the existing literature. Brown, gray, red, and white are Fe, Ge, O, and H atoms, respectively. (d) PEC efficiency of Fe_2O_3 , Ge-H, and Ge-PH with hole scavenger, .5 M Na_2SO_3 , (dashed lines) and without hole scavenger (solid lines) in basic electrolyte (1 M NaOH). (e) Calculated charge separation efficiencies by LSV curve w/wo hole scavenger.

Figure 4.13. (a) Schematic images of the working principle of a tandem device composed of hematite photoanode and PSC. (b) LSV curves of Ge-PH w/wo NiFeO_x . (c) LSV curves of PSC behind photoanode and our final photoanode ($\text{NiFeO}_x@\text{Ge-PH}$). (d) Long-term stability test of our final photoanode ($\text{NiFeO}_x@\text{Ge-PH}$) at $1.23V_{\text{RHE}}$ and tandem device for solar water splitting. (e) Gases measurements for calculating Faradaic efficiency of the $\text{NiFeO}_x@\text{Ge-PH}$.

Figure 4.14. LSV curves of PSC under 1 SUN illumination.

Figure 4.15. (a) UV-Vis and (b) IPCE spectra of Fe_2O_3 , Ge-H and Ge-PH.

List of Tables

Table 1.1 Comparison of advantages and disadvantages of various photocatalysts used in the PEC system.

Table 1.2. Electrolyte-dependent HER mechanism in basic and acidic electrolytes.

Table 2.1. The values by fitted resistance calculated from the EIS results.

Table 3.1. Comparison of the PEC performance and Si content.

Table 4.1. Calculated results from Mott-Schottky plots for the flat band potential (E_{FB}), charge carrier concentration (N_D), and space charge width (W_{sc}).

Table 4.2. Recent reports on hematite-based tandem system.

Chapter 1. Introduction: hydrogen energy

1.1 Hydrogen: grey, blue and green hydrogen

Achieving the global energy goal of zero emissions requires fundamental changes in power systems as well as power generation and consumption. Hydrogen has tremendous potential as the next generation energy.^{1,2} Since hydrogen is the energy carrier, it is possible to store and transfer the energy by chemical reactions rather than combustion. The byproduct of hydrogen energy is only water and heat and hydrogen has a high specific energy compared with other energy sources as shown in Figure 1.1a. However, hydrogen has a low energy density indicating that it requires a progressive storage system to make it practical for use in electric devices as shown in Figure 1.1b. In order for hydrogen energy to be competitive with the other energy sources currently used, therefore, the storage and delivery system for hydrogen should be well developed. Along with hydrogen storage and delivery, the means of hydrogen production are also one of the three tasks of hydrogen energy. Paradoxically, most of the hydrogen for an ideal eco-friendly system is produced by refining fossil fuels. This means that a lot of environmental pollutions must be caused to make hydrogen. For this part, there are a lot of controversies about whether hydrogen energy is suitable as the next-generation energy. Therefore, to realize a hydrogen society, many technologies should be developed to a certain level where all three of hydrogen production, storage, and transport can replace the current energy system. Depending on the hydrogen production technology, hydrogen can be divided into three types: grey hydrogen,³ blue hydrogen,⁴ and green hydrogen^{5,6} as shown in Figure 1.2. First, grey hydrogen refers to hydrogen that is extracted from fossil fuels, producing it the least renewable form of hydrogen. Most of the hydrogen currently being produced is grey hydrogen. It is relatively inexpensive and commonly used in the industry to make fertilizer and for refining oil. For grey hydrogen production, methane, the primary element in natural gas, is mixed with steam at a high temperature to yield hydrogen and carbon dioxide through a catalytic chemical reaction. Since this part is not eco-friendly, it is fatal to realizing a hydrogen society. Blue hydrogen is a more improved production method of grey hydrogen. The CO₂ gases generated during hydrogen production is captured and stored using storage facilities so that it is not emitted to the outside. This system is known as carbon capture and storage (CSS). However, the storage also is costly and has logistical challenges. Blue hydrogen is the most realistic hydrogen production method available at the current technological level, but it is not suitable for the ideal hydrogen energy cycle. Finally, there is green hydrogen, which is the most ideal and ultimate goal. Green hydrogen produces hydrogen by decomposing water. The water electrolysis produces oxygen and hydrogen only and does not produce any byproducts. As mentioned above, since hydrogen energy generates only water and heat when used,

the green hydrogen can form the most ideal energy circulation system in which only the water cycle process occurs. Because hydrogen can be obtained by simply electrolyzing water, there is no need for complex equipment such as grey hydrogen or blue hydrogen. Therefore, another advantage of green hydrogen is that a grid-off system is possible. In other words, it is possible to alleviate the problems of hydrogen storage and transportation by individuals directly producing and using hydrogen. Since a lot of electrical energy is consumed to decompose water, the cost of hydrogen production is very expensive compared to grey hydrogen or blue hydrogen. In addition, since the catalysts used for water electrolysis are made of expensive precious metals such as platinum or iridium, the material cost is also high as shown in Figure 1.3a. Water decomposes when the energy of 1.23 V is applied, which is an energy equivalent to 237 kJ mol^{-1} .⁷ However, it is limited to cases where ideal water decomposition is possible. In other words, there is no energy loss occurring in the system. Therefore, considering the energy loss in the actual system, it requires more energy than 1.23 V as shown in Figure 1.3b. The reason for the energy loss is the overpotential that occurs in the OER and HER reaction, and the resistances including the total system and materials. Therefore, the catalysts made of inexpensive materials are being developed to lower the production cost of green hydrogen. In addition, the development of systems that can handle the energy use required for water electrolysis more efficiently is in progress. In terms of water electrolysis system, researchers have considered the systems that use renewable energy for water electrolysis as one of the most promising as shown in Figure 1.3c. Renewable energies such as hydro,⁸ wind,⁹ geothermal¹⁰ and solar energy^{11,12} have been proposed as candidates for water splitting. Among various renewable energies, solar energy is one of the most promising eco-friendly energy sources. Figure 1.4 shows various sources on the earth. If we could use only 1% of the solar energy without any loss, we would be able to use the same amount of energy as all the energy on Earth combined. The amount of solar energy delivered to the Earth is about 173,000 TW, which is about 9600 times higher than the total global energy consumption (17.91 TW).⁷ Therefore, humanity's efforts to utilize solar energy will continue as long as the sun does not disappear from space. However, converting and using solar energy delivered to the earth is a task that needs to be solved in the future as only a very low level of energy conversion is possible with current technology. There are various solar-driven water splitting systems. Solar-driven water splitting systems utilize semiconductors, different from general water splitting catalysts. In this thesis, we will focus on the principle of solar driven water splitting system and the challenges to be solved.

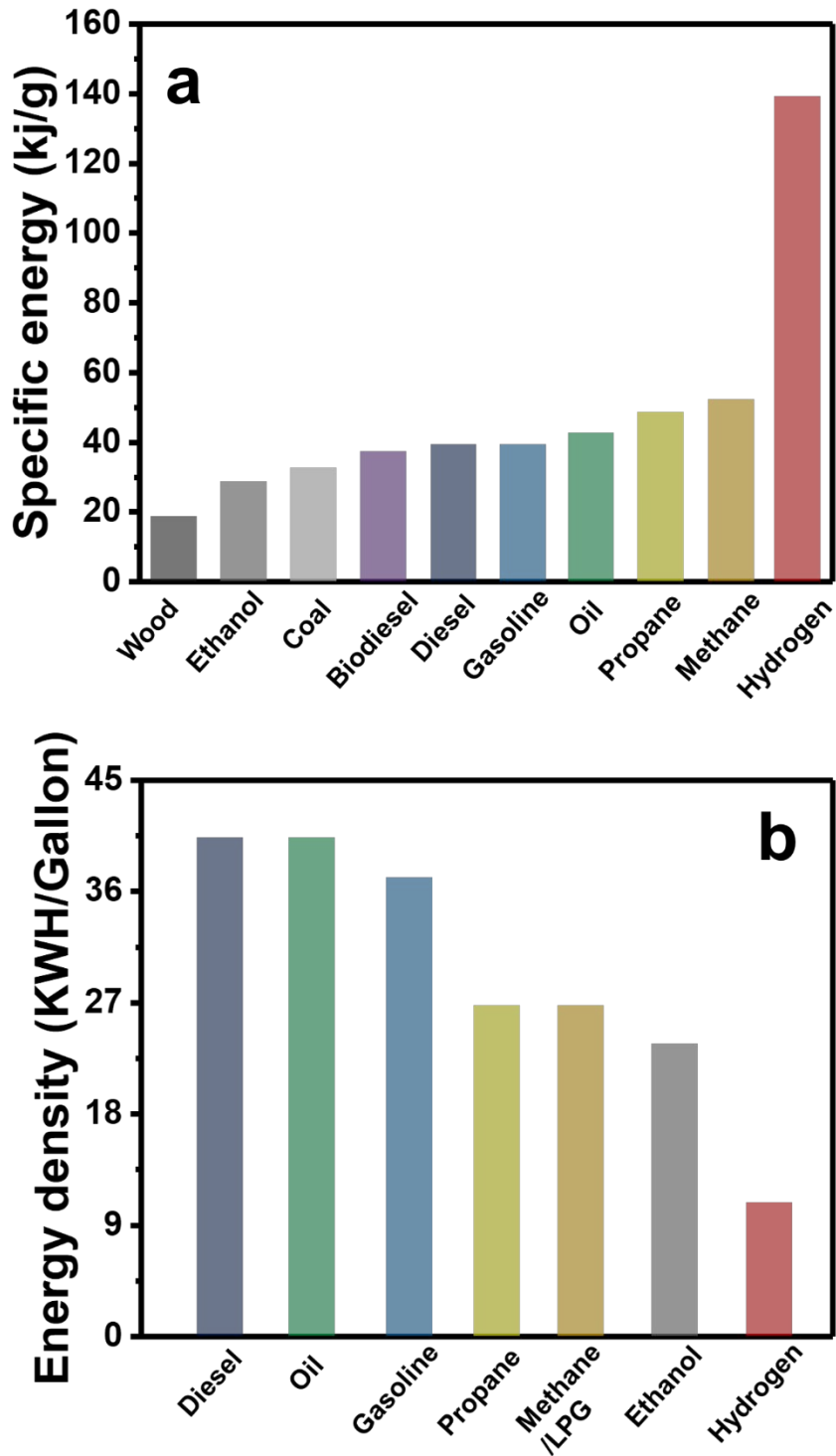


Figure 1.1. Comparison of (a) specific energy and (b) energy density for various energy sources. DOE, Green Econometrics research.

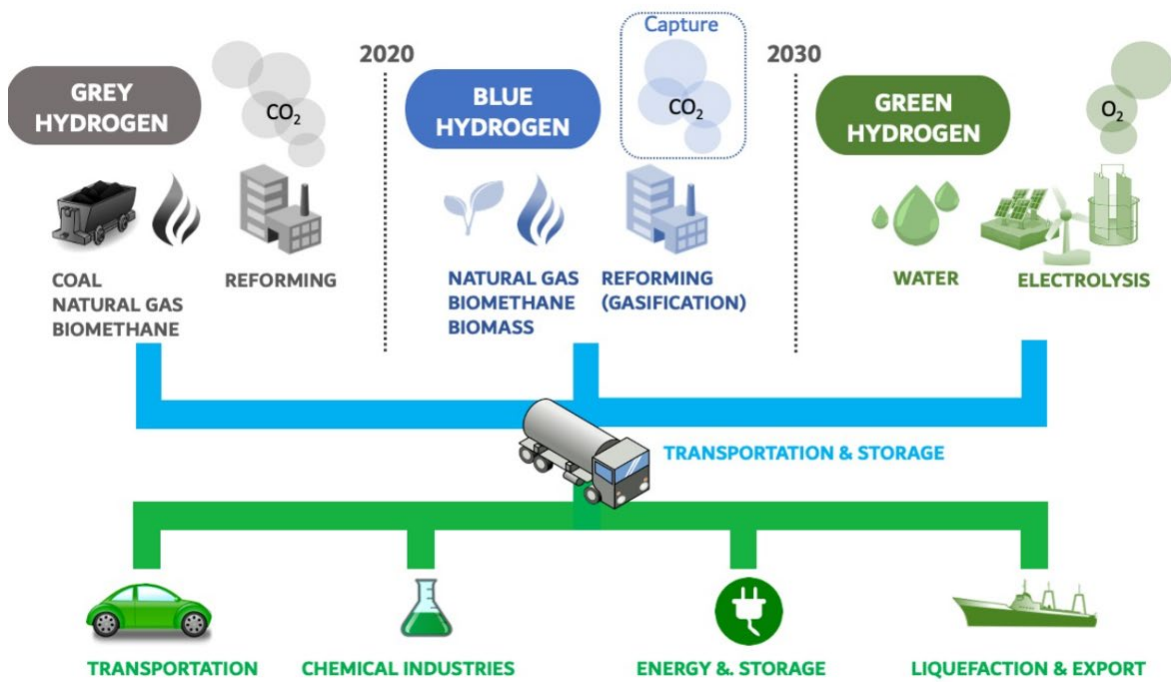
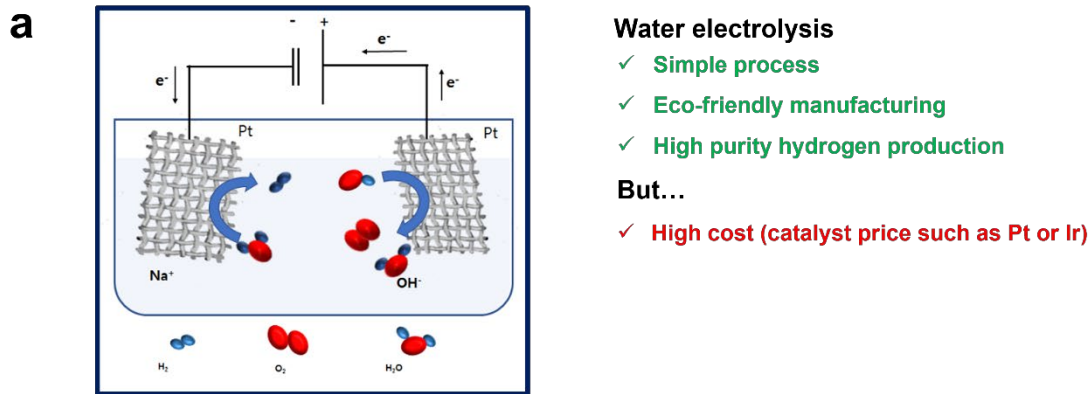


Figure 1.2. The schematic image for grey, blue, and green hydrogen production systems. DOE, Chem4us.



The required energy for actual water electrolysis is $>1.23\text{V}$ by η_{loss}

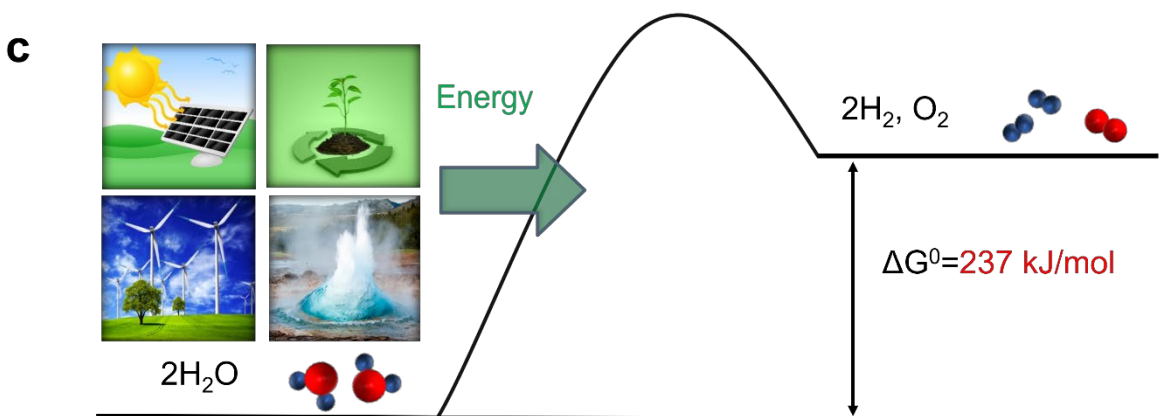
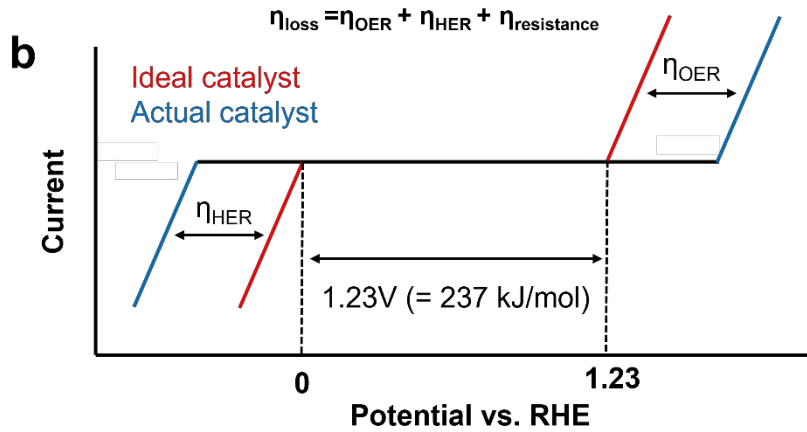


Figure 1.3. Schematic image of water electrolysis with advantages and disadvantages. (b) Schematic image of needed energy for OER and HER reaction of theoretical and actual catalysts. (c) Energy needed for water splitting and alternative energy sources.

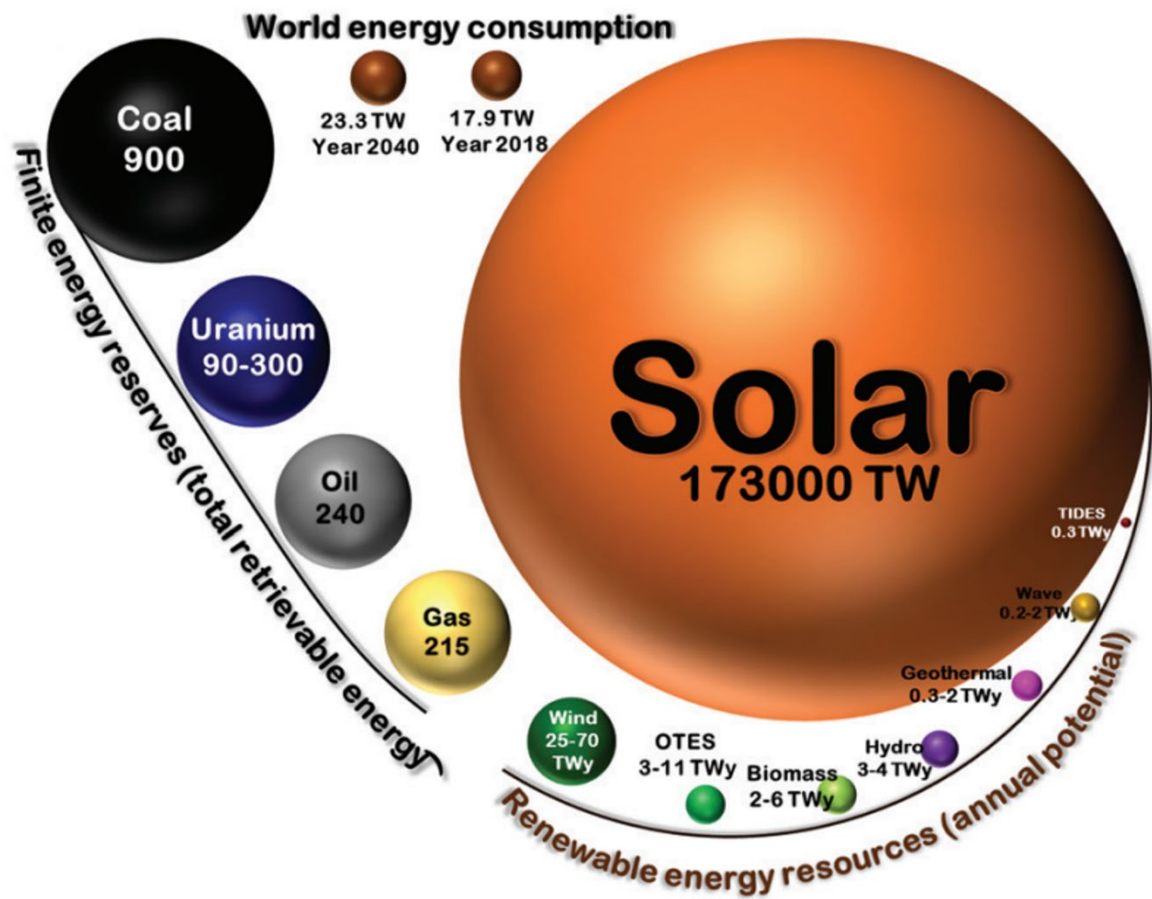


Figure 1.4. (a) Various energy resources existing on Earth. Reproduced from ref. 5 with permission from the IEA/SHC Solar Update, copyright 2009.

1.2 Understanding the photoelectrochemical water splitting

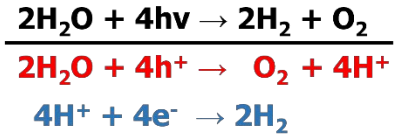
The photoelectrochemical water splitting system is one of the technologies that enables the formation of the most ideal hydrogen energy circulation system. This system can offset the overpotential for water splitting by receiving the energy required for water splitting from solar energy.^{13,14} In other words, the water splitting through oxygen evolution reaction and hydrogen evolution reaction requires an external applied voltage of 1.23 V or higher, but this system can split water molecules at lower external voltage than 1.23 V. To convert water molecules into O₂ and H₂ gases, a Gibbs energy of 237 KJ mol⁻¹ at 298 K and 1 bar is required since the water electrolysis is a thermodynamically unfavorable reaction. Therefore, The photoelectrochemical water splitting systems are preferred over the general electrochemical water splitting systems for these reasons.^{15,16} The photoelectrochemical water splitting is to collect solar energy and use it for green hydrogen production. When the semiconductor is irradiated with sunlight, electron-hole pairs are created by the band gap of semiconductor. As the holes and electrons move to the surface of the semiconductor, the holes participate in the oxidation reaction of water and the electrons participate in the reduction reaction of water to make oxygen and hydrogen. In this process, there are cases where co-catalysts are additionally used to increase the respective reaction activity of OER and HER.¹⁷⁻¹⁹ A simple schematic image of the reaction mechanism of photoelectrochemical water splitting is shown in Figure 1.5 and the following conditions are required to increase hydrogen production efficiency. First, it is necessary to select a semiconductor material that can efficiently utilize solar spectrum. As shown in Figure 1.6, there are various semiconductors that can be used in the photoelectrochemical water splitting, but there is no semiconductor material that can be used ideally so far. The semiconductors to be used for photoelectrochemical water splitting should have outstanding stability in an aqueous environment since they must not only absorb the sunlight but also operate in an electrolyte. Next, we need to consider the charge transport, how quickly the generated holes and electrons can reach the surface of the semiconductor without the recombination. Finally, it is necessary to consider how quickly the holes and electrons reaching the surface of semiconductor can be used for water oxidation and reduction reactions. According to these mechanisms, the degree of photoelectrochemical water splitting reaction of semiconductor is determined, and solar-to-hydrogen (STH) conversion efficiency can be calculated according to the degree of hydrogen production. Various semiconductors are being tried for PEC water splitting, and the representative materials currently used are TiO₂, ZnO, WO₃, BiVO₄ and Fe₂O₃ as summarized in Table 1.1. Each of these semiconductors has advantages and disadvantages, and many efforts have been made to solve the disadvantages of each material. In the case of WO₃, it can be maintained in a stable state under acidic conditions, and its hole diffusion length is also suitable for use as a PEC material. However, WO₃ has a large band gap, it cannot

utilize wide spectrum light, but also the corrosion occurs due to peroxy-species generated during PEC reaction. TiO_2 and ZnO also have a bandgap of 3.0 eV or more, resulting in the light cannot be fully utilized. Instead, ZnO and TiO_2 can easily form junctions with other photocatalysts by taking advantage of their large bandgap, and most research has focused on solving the bandgap problem through bandgap junctions. In the case of BiVO_4 , it has a suitable band gap (2.4-2.5 eV) compared to the above-mentioned semiconductors and forms an appropriate band energy for water splitting. BiVO_4 has a theoretical STH of about 9% and is the closest material to commercialization. Due to many efforts to improve BiVO_4 efficiency, the achievements of reaching about 90% of the theoretical efficiency are being realized. However, since the commercialization of PEC system needs to reach an efficiency of at least 10% STH, an innovative system or bandgap engineering that goes beyond the theoretical efficiency of BiVO_4 is required. From a theoretical efficiency point of view, hematite is the most promising material. Hematite has a band gap of 1.9-2.2, so it can fully utilize the broad spectrum of sunlight and the theoretical efficiency is up to around 15%. In addition, it has outstanding stability in basic electrolytes with excellent oxygen evolution reaction. Therefore, the development of a PEC system using hematite is highly active. However, hematite is currently showing about 1-2% STH performance due to characteristics such as poor electrical property and short length for hole travel, which are applied as fatal disadvantages in the PEC system. Therefore, solving the low electrical conductivity and short hole diffusion length of hematite is the most challenging task in the hematite-based PEC system. In this thesis, we cover photoelectrochemical water splitting using iron oxide, called hematite among n-type semiconductors used for solar-driven water oxidation.



Clean & Renewable

Target reaction



Solar-To-Hydrogen (STH) conversion efficiency

1. Light collection
- +
 2. Charge separation
 - +
 3. Charge transport
 - +
 4. Reaction kinetics

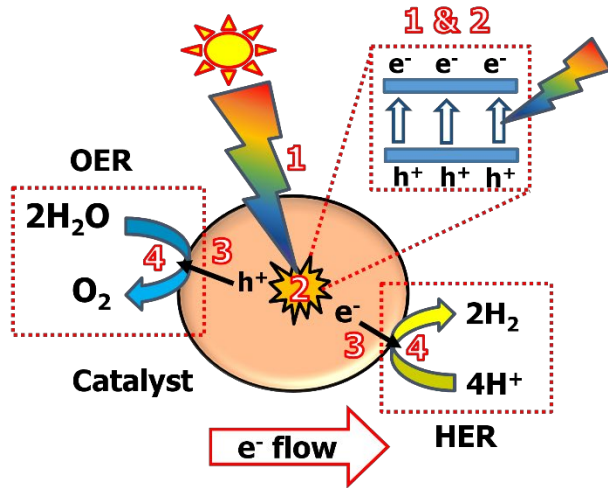


Figure 1.5. Photoelectrochemical water splitting system for green hydrogen production using solar energy and water and the necessary factors to improve the system efficiency.

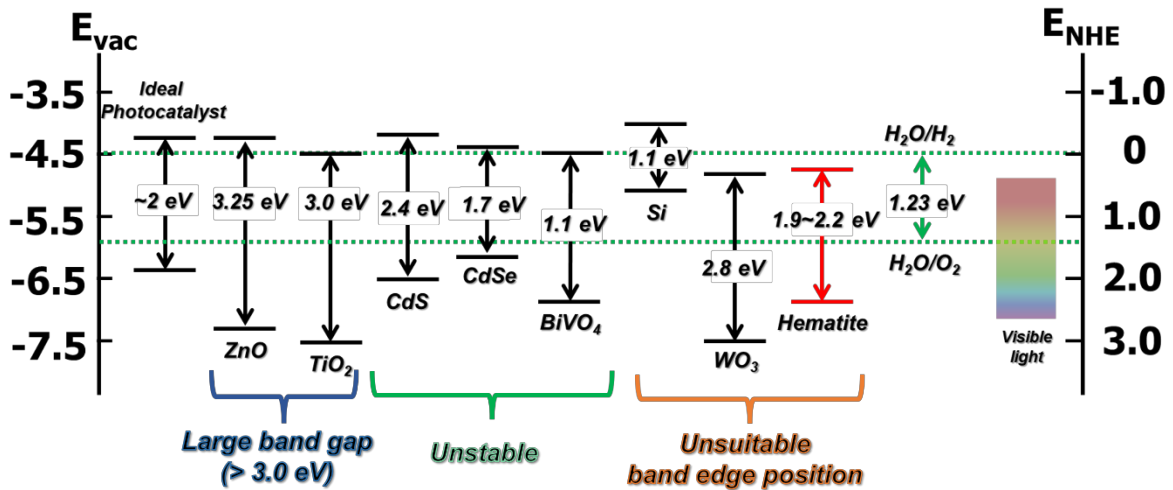


Figure 1.6. various semiconductor candidates for photoelectrochemical water splitting.

Photoanodes	Advantages	Disadvantages	Theoretical STH efficiency
WO₃	Stable in acid conditions (pH < 4) and proper hole-diffusion length (~ 150 nm).	Photo-corrosion by peroxy-species, Large band gap of 2.4–2.8 eV, slow water oxidation kinetics and fast electron-hole recombination.	~8%
ZnO	Outstanding electron lifetime exceeding 10 s with High electron mobility.	Large bandgap of 3.2 eV and Poor chemical stability in electrolytes.	~2%
TiO₂	Stable against chemical corrosion, suitable valence band edge and good electrical conductivity	Large bandgap of 3.0–3.2 eV and low charge separation efficiency	~2%
BiVO₄	Proper bandgap of 2.4–2.5 eV and the energy level of conduction band edge (0.1–0.2 V vs. NHE) for water splitting	Unstable against alkaline electrolyte and low theoretical STH efficiency.	~9%
Fe₂O₃	High chemical stability in alkaline electrolyte and good bandgap (2.0–2.2 eV) with high theoretical STH efficiency	Short hole diffusion length (2–4 nm), Poor electron mobility (~10 ⁻¹ cm ² V ⁻¹ s ⁻¹ at 20 °C) and slow OER kinetics.	~15%

Table 1.1 Comparison of advantages and disadvantages of various photocatalysts used in the PEC system.

1.3 Hematite (α -Fe₂O₃): promising n-type semiconductor for PEC water oxidation

Hematite is one of the oxides of iron and iron is the fourth most common element in the earth's crust (6.3 % by weight).²⁰ Iron oxide is ubiquitous since iron is readily oxidized in air to the ferrous (+2) and ferric (+3) states.⁵ Hematite is the most thermodynamically stable form of iron oxide in ambient conditions, and it is also the most common form of crystalline iron oxide. Hematite has properties suitable for use in PEC system. First, hematite has an average bandgap of 1.9-2.2 eV, indicating that the light absorption range for solar energy is very wide. From an optical point of view, the theoretical STH conversion efficiency of hematite is possible up to around 15%.²¹ This means that it has great potential compared to other metal oxides. For example, other metal oxides such as TiO₂,^{22,23} ZnO²⁴ and WO₃²⁵ have the bandgap of around 3.0 eV, indicating that most of them can only absorb the solar energy in the UV range. In addition, Hematite is very stable under basic condition. Usually in electronic devices, the oxide formation should be suppressed, but hematite is an already oxidized material. Therefore, the stability of the hematite electrode is guaranteed since it is stable in basic condition. This is a great advantage as a material for use in PEC electrode since it must form a direct reaction in the electrolyte due to the characteristics of the PEC system. Taking these advantages, hematite has been mainly used for photoanode for water oxidation reaction in the whole system of PEC water splitting. The water oxidation reaction system using hematite is as shown in Figure 1.7. When the photon energy is absorbed by hematite, hole and electron pairs are generated in the hematite. The hole and electron move to the reaction surface and four holes and electrons can produce one oxygen molecule and two hydrogen molecules. Hematite is an n-type semiconductor and mainly studies the water oxidation reaction in half cell device. In conclusion, the most important part is how efficiently hematite can oxidize water. As mentioned above, hematite is clearly one of the most attractive materials for use in the photoanode part among various metal oxides. However, although many studies have been conducted so far, the actual STH conversion efficiency is less than half of the theoretical efficiency. As many studies have been conducted, the shortcomings of hematite have been discovered: (i) a flat band potential, too low in energy for water reduction²⁶ as shown in Figure 1.6, (ii) low electrical conductivity,²⁷ (iii) a very short hole-diffusion-length (> 5nm)²⁸ and (iv) a relatively low absorption coefficient, requiring 400-500 nm thick film for complete light absorption.²⁹ Due to these shortcomings, the actual efficiency of hematite is currently stuck at 2-3 % STH conversion efficiency. To overcome these limitations, many challenges are still being made, and the research field of hematite photoanode can be divided as shown in Figure 1.8. First of all, in the case of substrate, transparent conductive (TCO) substrates have been mainly used for hematite photoanode.

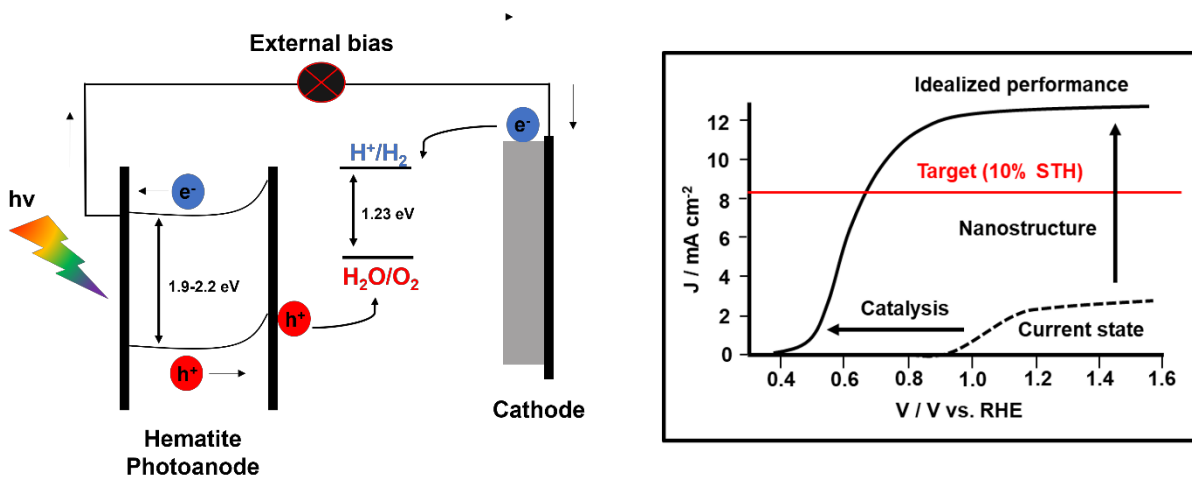


Figure 1.7. Energy diagram for hematite-based photoelectrochemical water splitting and Idealized LSV curve and current state for photoelectrochemical water oxidation of n-type hematite semiconductor.

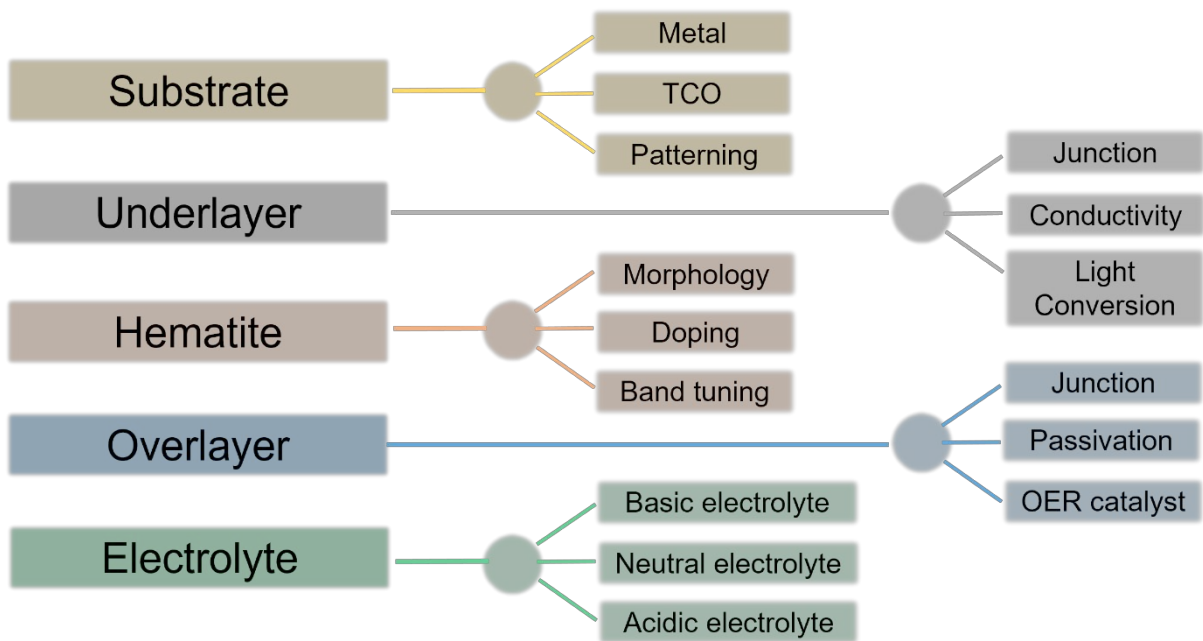
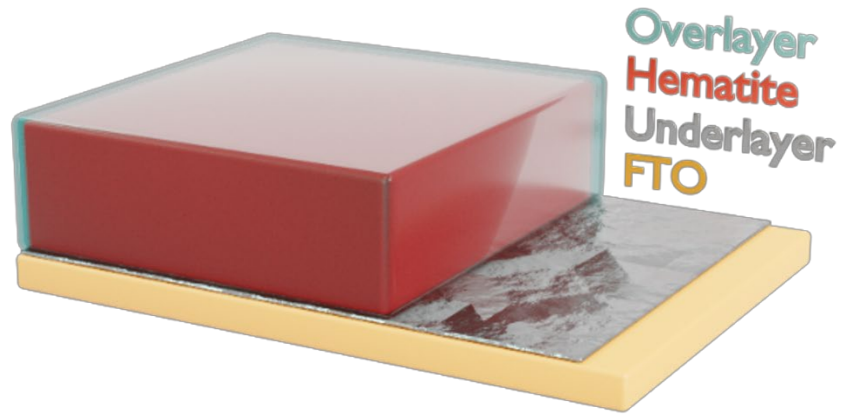


Figure 1.8. Overview of the main categories of hematite-based photoelectrochemical water splitting.

Sometimes metal substrates such as iron^{30,31} or titanium³² were used, but this is limited to half-cell testing since the ultimate purpose of this technology is to make a spontaneous hydrogen production system without externally applied voltage in a full-cell device.³³ Therefore, it is mainly carried out using the TCO substrate, and a full-cell test is sometimes performed using a tandem system along with appropriate cathode. Among various TCO substrates, Fluorine-doped tin oxide (FTO) coated glass have been mainly used since the activation is required to boost the PEC performance of hematite photoanode with high temperature (above 700 °C).^{21,29} This will be discussed in detail in the section on hematite synthesis part. Since the substrate usually has a flat two-dimensional shape, many attempts have been made to manufacture and use the substrate in three-dimensional form to obtain the surface area increase and light trapping effect. This strategy can overcome the disadvantage of hematite's low absorption coefficient as shown in Figure 1.9.^{29,34} Substrate research is still needed since the current FTO substrate is difficult to withstand high-temperature heat treatment (above 700 °C), which is an essential manufacturing process of hematite. If the electrode is damaged by high temperature, the resistance increases, and the energy loss becomes severe. At present, laboratory-scale electrodes are being manufactured, but as the efficiency will decrease rapidly when the area is enlarged in the future, it is essential to study a substrate that can withstand high temperatures.³⁵

The studies using underlayers^{36,37} and overlayers³⁸ have also been actively conducted to maximize the PEC performance. In the case of the underlayer, it has been used as the electron transport layer (ETL) with junction, improving the conductivity of the substrate and using up-conversion or down-conversion to maximize the wavelength at which hematite is most efficient. For underlayer, the oxides such as TiO₂,³⁹ SiO_x,⁴⁰ and Nb₂O₅³⁷ have been widely used, and they are known to have the effect of improving efficiency by preventing back electron injection as shown in Figure 1.10. In the case of Fe₂O₃ using an underlayer, the overall PEC efficiency is low. Because the underlayer must be coated before high-temperature process, which is one of the manufacturing processes of hematite resulting in the damage of the underlayer or low-temperature heat treatment is used to prevent material damage. Therefore, the utilization of the underlayer is limitedly used in the hematite electrode system.

In the case of the overlayer, it has been applied more widely than the underlayer. The use of overlayer can be divided into three main categories: (i) hole transport layer (HTL),^{41,42} (ii) passivation layer^{43,44} and (iii) OER co-catalyst.⁴⁵⁻⁴⁷ When used as an HTL, it has been mainly used to solve the short hole diffusion length, the biggest problem of hematite, by making a junction with hematite. TiO₂ has been the most used material because it can make the junction with hematite as well as passivation to compensate for the surface defects of hematite as shown in Figure 1.11. Surface defects should be suppressed as much as possible to cause recombination of electron holes, and this can be supplemented through a passivation layer. The co-catalyst layer can boost the PEC performance by improving the

OER kinetic while compensating for surface defects as passivation layer. Typical OER co-catalyst used in hematite are Co-Pi, NiFeO_x, and FeOOH. For these OER co-catalyst, the main challenges were to study the interface between hematite and the OER co-catalyst or to minimize the light shielding effect by the OER co-catalyst as shown in Figure 1.12. Apart from electrode development, PEC systems that can be operated in various electrolytes have also been studied. Basically, OER shows the best efficiency with basic electrolyte since it has sufficient OH⁻. In the case of neutral electrolytes, the PEC system has been tried because the safety is superior to that of basic electrolytes, and acid electrolytes have been challenged to increase the efficiency of full cell because the HER is excellent in acidic conditions by sufficient H⁺. Therefore, OER and HER mechanisms are slightly different depending on which electrolyte is used, and studies are being conducted to find materials suitable for each mechanism⁴⁸ as shown in Figure 1.13 and Table 1.2. Finally, there are studies that improve the performance of hematite itself, which will be mainly covered in this thesis.

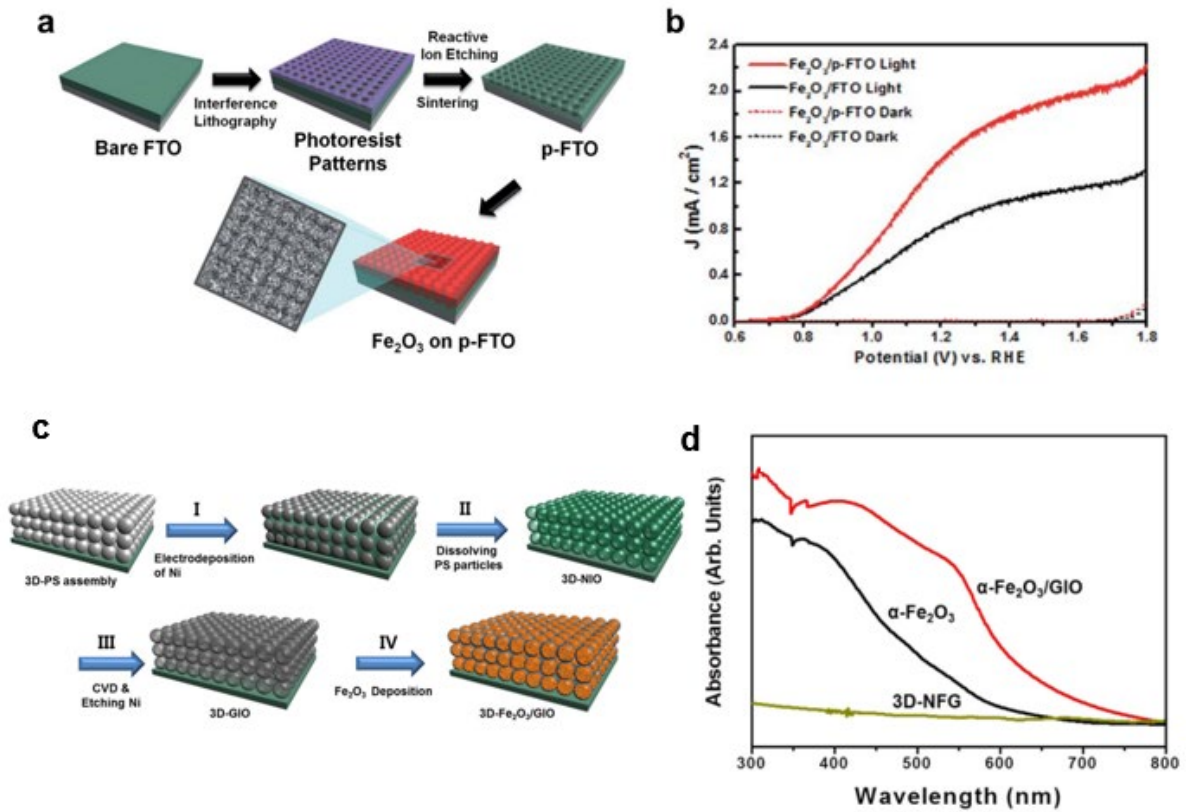


Figure 1.9. (a) Schematic image for the fabrication of hematite on patented FTO (p-FTO) substrate. (b) Linear sweep voltammetry curves of Fe_2O_3 on FTO or p-FTO substrate. Copyright © 2015, Royal Society of Chemistry. (c) Schematic image for the fabrication of 3D FTO substrate by PS assembly. (d). UV-Vis absorption of 3D-NFG, Fe_2O_3 and $\text{Fe}_2\text{O}_3/\text{GIO}$. Copyright © 2014, American Chemical Society.

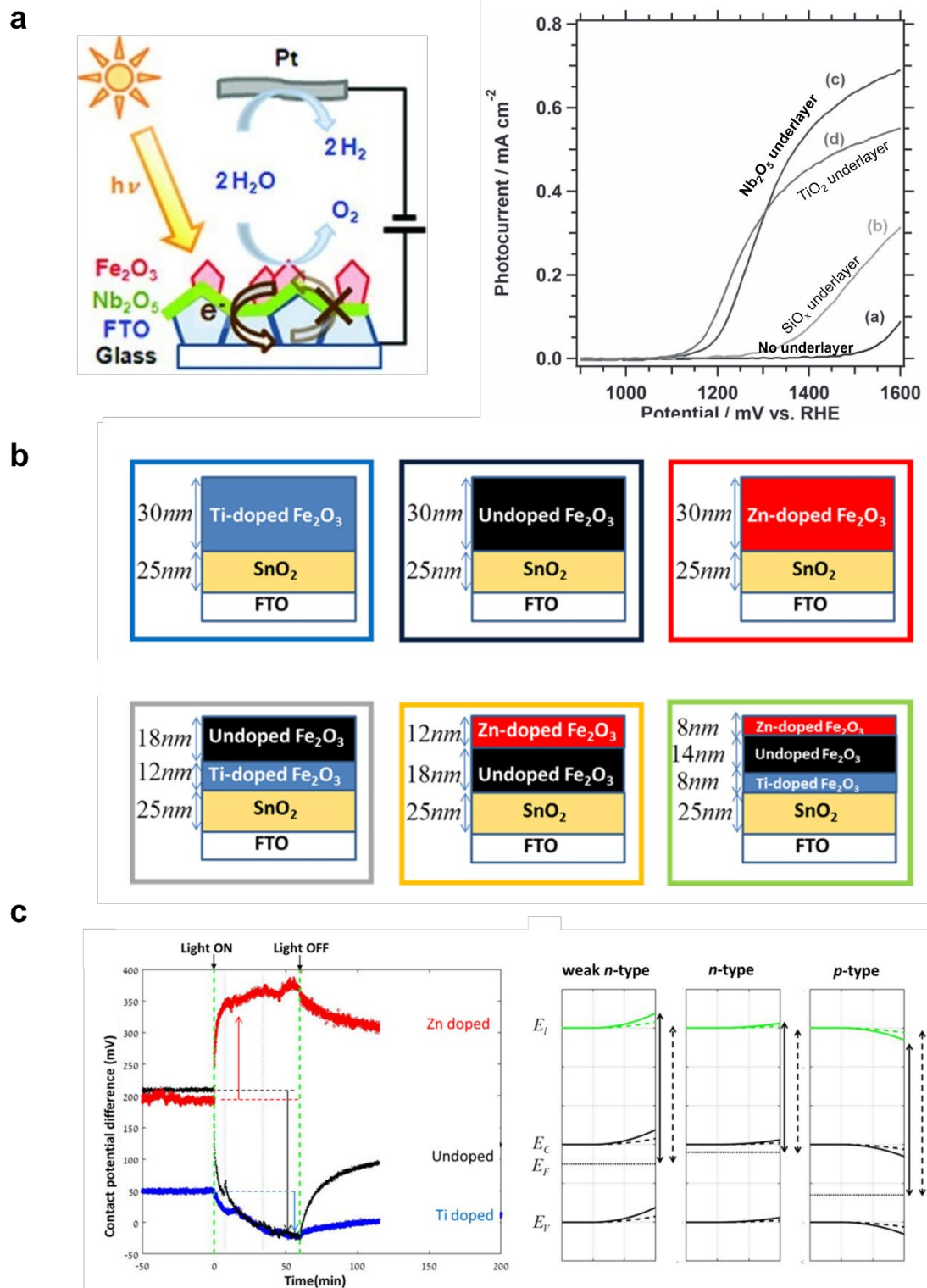


Figure 1.10. (a) Schematic image for underlayer mechanism for hematite photoanode and linear sweep voltammetry curves of Fe_2O_3 with various underlayers. Copyright © 2012 WILEY-VCH Verlag GmbH & Co. KGaA, Weinheim. (b) Schematic configuration for underlayer. (c) SPV measurements and band diagram. Copyright © 2016, American Chemical Society.

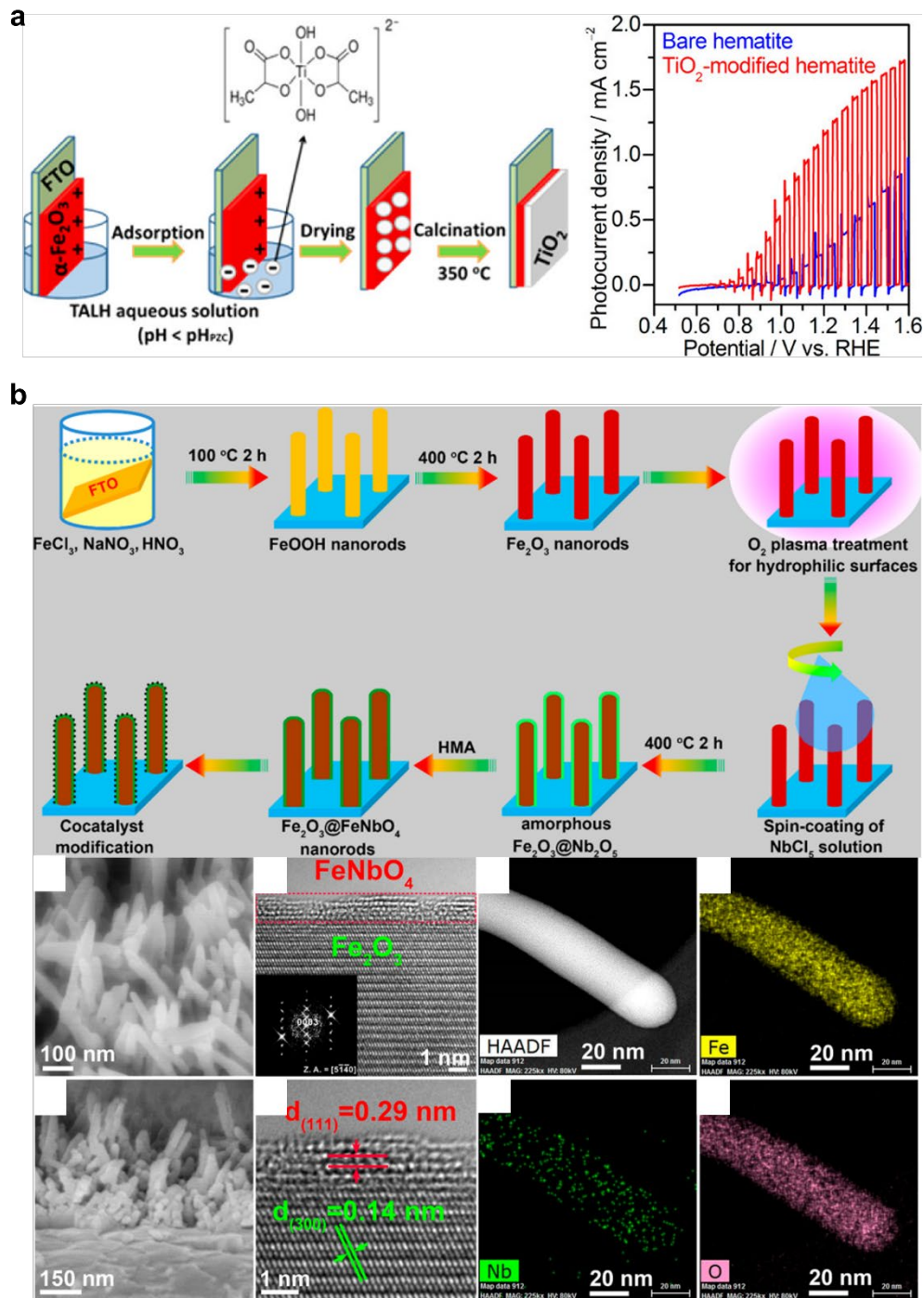


Figure 1.11. (a) Schematic image for fabrication of TiO₂ overlayer coated hematite photoanode. (b) Linear sweep voltammetry curves of Fe₂O₃ w/wo TiO₂ overlayer. Copyright © 2015, American Chemical Society. (b) Schematic image for fabrication process utilizing Nb₂O₅ overlayer on hematite and SEM, TEM, HAADF, and EDX mapping images for hematite using Nb₂O₅ overlayer. Copyright © 2018, American Chemical Society.

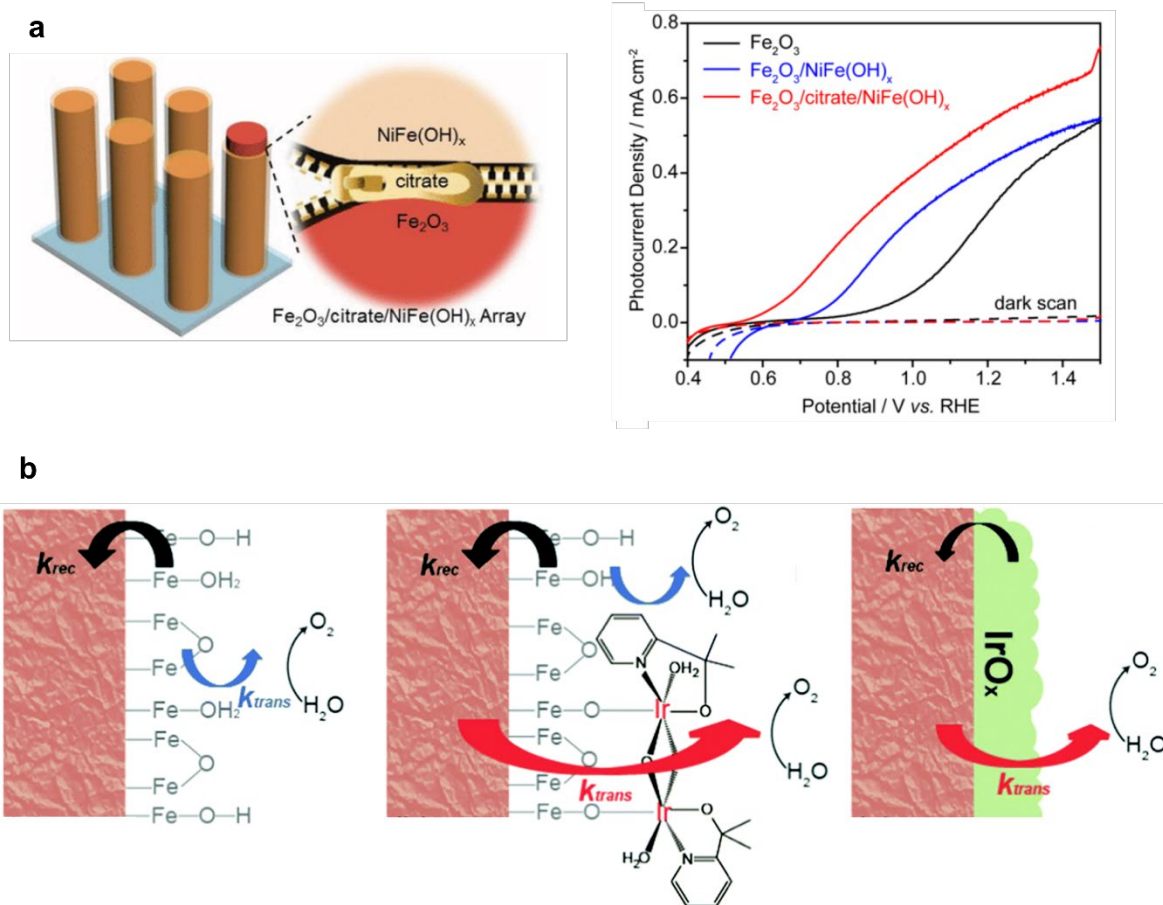


Figure 1.12. (a) Schematic image for improving the interface between NiFe(OH)_x and hematite by citrate and linear sweep voltammetry curves of Fe_2O_3 and NiFe(OH)_x coated Fe_2O_3 w/o citrate treatment. Copyright © 2019, American Chemical Society. (b) Schematic images of the kinetic process for pristine Fe_2O_3 , heterogenized molecular Ir catalyst coated Fe_2O_3 , IrO_2 co-catalyst coated Fe_2O_3 . Copyright © 2015, Royal Society of Chemistry.

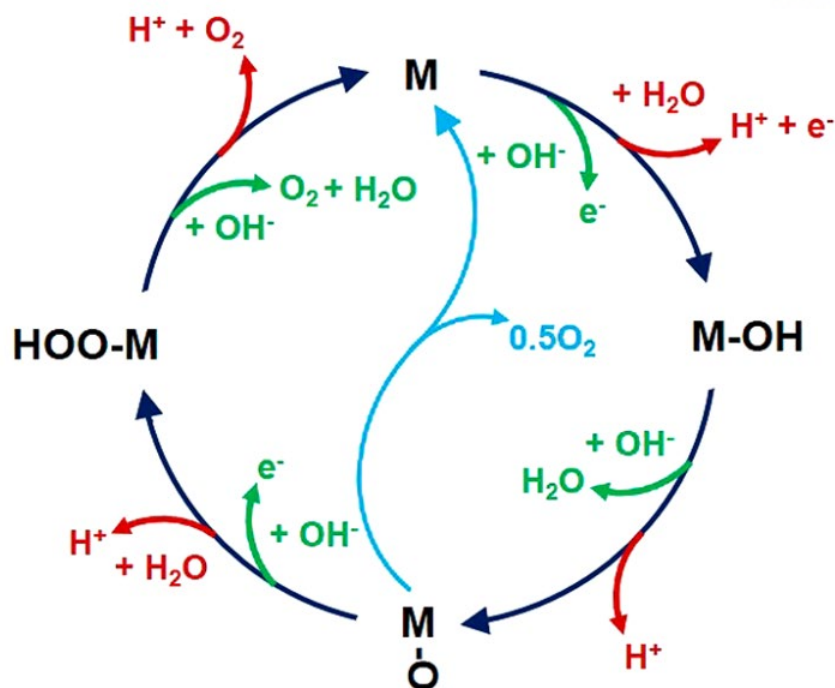


Figure 1.13. Electrolyte-dependent OER mechanism for red step of basic electrolyte and green step of acidic electrolytes. The black arrows indicates that the overall OER mechanism by four steps and blue steps are two adjacent oxo for M–O intermediates for oxidation process. Copyright © 2018, American Chemical Society.

	acid	alkaline	Tafel slope
overall	$* + 2\text{H}^+ + 2\text{e}^- \rightarrow \text{H}_2$	$* + 2\text{H}_2\text{O} + 2\text{e}^- \rightarrow \text{H}_2 + 2\text{OH}^-$	–
Volmer	$* + \text{H}^+ + \text{e}^- \rightarrow \text{H}^*$	$* + \text{H}_2\text{O} + \text{e}^- \rightarrow \text{H}^* + \text{OH}^-$	$b = \frac{2.3RT}{\alpha F} \approx 120 \text{ mV dec}^{-1}$
Heyrovsky	$* + \text{H}^+ + \text{e}^- + \text{H}^* \rightarrow \text{H}_2 + *$	$* + \text{H}_2\text{O} + \text{e}^- + \text{H}^* \rightarrow \text{H}_2 + \text{OH}^- + *$	$b = \frac{2.3RT}{(1 + \alpha)F} \approx 40 \text{ mV dec}^{-1}$
Tafel	$2\text{H}^* \rightarrow \text{H}_2 + 2*$	$2\text{H}^* \rightarrow \text{H}_2 + 2*$	$b = \frac{2.3RT}{2F} \approx 30 \text{ mV dec}^{-1}$

Table 1.2. Electrolyte-dependent HER mechanism in basic and acidic electrolytes. Copyright © 2018, American Chemical Society.

1.4 References

- (1) Van Hoecke, L.; Laffineur, L.; Campe, R.; Perreault, P.; Verbruggen, S. W.; Lenaerts, S. Challenges in the Use of Hydrogen for Maritime Applications. *Energy Environ. Sci.* **2021**, *14* (2), 815–843. <https://doi.org/10.1039/D0EE01545H>.
- (2) Wang, C.; Astruc, D. Recent Developments of Nanocatalyzed Liquid-Phase Hydrogen Generation. *Chem. Soc. Rev.* **2021**, *50* (5), 3437–3484. <https://doi.org/10.1039/D0CS00515K>.
- (3) Vennelakanti, V.; Qi, H. W.; Mehmood, R.; Kulik, H. J. When Are Two Hydrogen Bonds Better than One? Accurate First-Principles Models Explain the Balance of Hydrogen Bond Donors and Acceptors Found in Proteins. *Chem. Sci.* **2021**, *12* (3), 1147–1162. <https://doi.org/10.1039/D0SC05084A>.
- (4) Bauer, C.; Treyer, K.; Antonini, C.; Bergerson, J.; Gazzani, M.; Gencer, E.; Gibbins, J.; Mazzotti, M.; McCoy, S. T.; McKenna, R.; Pietzcker, R.; Ravikumar, A. P.; Romano, M. C.; Ueckerdt, F.; Vente, J.; van der Spek, M. On the Climate Impacts of Blue Hydrogen Production. *Sustain. Energy Fuels* **2022**, *6* (1), 66–75. <https://doi.org/10.1039/D1SE01508G>.
- (5) Sharma, P.; Jang, J.-W.; Lee, J. S. Key Strategies to Advance the Photoelectrochemical Water Splitting Performance of α -Fe₂O₃ Photoanode. *ChemCatChem* **2019**, *11* (1), 157–179. <https://doi.org/https://doi.org/10.1002/cctc.201801187>.
- (6) Jorschick, H.; Preuster, P.; Bösmann, A.; Wasserscheid, P. Hydrogenation of Aromatic and Heteroaromatic Compounds – a Key Process for Future Logistics of Green Hydrogen Using Liquid Organic Hydrogen Carrier Systems. *Sustain. Energy Fuels* **2021**, *5* (5), 1311–1346. <https://doi.org/10.1039/D0SE01369B>.
- (7) Kim, J. H.; Hansora, D.; Sharma, P.; Jang, J.-W.; Lee, J. S. Toward Practical Solar Hydrogen Production – an Artificial Photosynthetic Leaf-to-Farm Challenge. *Chem. Soc. Rev.* **2019**, *48* (7), 1908–1971. <https://doi.org/10.1039/C8CS00699G>.
- (8) Mehrjerdi, H.; Hemmati, R.; Shafie-khah, M.; Catalão, J. P. S. Zero Energy Building by Multicarrier Energy Systems Including Hydro, Wind, Solar, and Hydrogen. *IEEE Trans. Ind. Informatics* **2021**, *17* (8), 5474–5484. <https://doi.org/10.1109/TII.2020.3034346>.
- (9) Zhou, T.; Francois, B.; Lebbal, M. el H.; Lecoecuche, S. Real-Time Emulation of a Hydrogen-Production Process for Assessment of an Active Wind-Energy Conversion System. *IEEE Trans. Ind. Electron.* **2009**, *56* (3), 737–746. <https://doi.org/10.1109/TIE.2008.2007048>.
- (10) Ghazvini, M.; Sadeghzadeh, M.; Ahmadi, M. H.; Moosavi, S.; Pourfayaz, F. Geothermal Energy Use in Hydrogen Production: A Review. *Int. J. Energy Res.* **2019**, *43* (14), 7823–7851. <https://doi.org/https://doi.org/10.1002/er.4778>.

- (11) A., F. E.; L., M. R. Hydrogen- and Oxygen from Water. *Science* (80-.). **1977**, *197* (4308), 1050–1056. <https://doi.org/10.1126/science.197.4308.1050>.
- (12) Moss, B.; Babacan, O.; Kafizas, A.; Hankin, A. A Review of Inorganic Photoelectrode Developments and Reactor Scale-Up Challenges for Solar Hydrogen Production. *Adv. Energy Mater.* **2021**, *11* (13), 2003286. <https://doi.org/https://doi.org/10.1002/aenm.202003286>.
- (13) Jin, L.; Zhao, H.; Wang, Z. M.; Rosei, F. Quantum Dots-Based Photoelectrochemical Hydrogen Evolution from Water Splitting. *Adv. Energy Mater.* **2021**, *11* (12), 2003233. <https://doi.org/https://doi.org/10.1002/aenm.202003233>.
- (14) Siavash Moakhar, R.; Hosseini-Hosseiniabad, S. M.; Masudy-Panah, S.; Seza, A.; Jalali, M.; Fallah-Arani, H.; Dabir, F.; Gholipour, S.; Abdi, Y.; Bagheri-Hariri, M.; Riahi-Noori, N.; Lim, Y.-F.; Hagfeldt, A.; Saliba, M. Photoelectrochemical Water-Splitting Using CuO-Based Electrodes for Hydrogen Production: A Review. *Adv. Mater.* **2021**, *33* (33), 2007285. <https://doi.org/https://doi.org/10.1002/adma.202007285>.
- (15) Wang, D.; Chen, R.; Zhu, X.; Ye, D.; Yang, Y.; Yu, Y.; Li, J.; Liu, Y.; Zhao, H.; Liao, Q. Synergetic Photo-Thermo Catalytic Hydrogen Production by Carbon Materials. *J. Phys. Chem. Lett.* **2022**, *13* (6), 1602–1608. <https://doi.org/10.1021/acs.jpcclett.1c03988>.
- (16) Li, Q.; Li, Y.; Chen, J.; Wang, F.; Zhou, X.; Xuan, T.; Wang, C.; Yang, D.; Zhang, L. Synergistically Photo-Thermo-Catalytic Effect of Metal-Oxide Semiconductors with D10 Electronic Configuration for Hydrogen Generation in NaBH₄ Hydrolyzation. *Catal. Letters* **2021**. <https://doi.org/10.1007/s10562-021-03825-z>.
- (17) Zhang, J.; Huang, Y.; Lu, X.; Yang, J.; Tong, Y. Enhanced BiVO₄ Photoanode Photoelectrochemical Performance via Borate Treatment and a NiFeOx Cocatalyst. *ACS Sustain. Chem. Eng.* **2021**, *9* (24), 8306–8314. <https://doi.org/10.1021/acssuschemeng.1c03055>.
- (18) Chai, H.; Wang, P.; Wang, T.; Gao, L.; Li, F.; Jin, J. Surface Reconstruction of Cobalt Species on Amorphous Cobalt Silicate-Coated Fluorine-Doped Hematite for Efficient Photoelectrochemical Water Oxidation. *ACS Appl. Mater. Interfaces* **2021**, *13* (40), 47572–47580. <https://doi.org/10.1021/acsami.1c12597>.
- (19) Borrelli, M.; Querebillo, C. J.; Pastoetter, D. L.; Wang, T.; Milani, A.; Casari, C.; Khoa Ly, H.; He, F.; Hou, Y.; Neumann, C.; Turchanin, A.; Sun, H.; Weidinger, I. M.; Feng, X. Thiophene-Based Conjugated Acetylenic Polymers with Dual Active Sites for Efficient Co-Catalyst-Free Photoelectrochemical Water Reduction in Alkaline Medium. *Angew. Chemie Int. Ed.* **2021**, *60* (34), 18876–18881. <https://doi.org/https://doi.org/10.1002/anie.202104469>.
- (20) Tamirat, A. G.; Rick, J.; Dubale, A. A.; Su, W.-N.; Hwang, B.-J. Using Hematite for

- Photoelectrochemical Water Splitting: A Review of Current Progress and Challenges.
Nanoscale Horizons **2016**, *1* (4), 243–267. <https://doi.org/10.1039/C5NH00098J>.
- (21) Ahn, H.-J.; Yoon, K.-Y.; Kwak, M.-J.; Park, J.; Jang, J.-H. Boron Doping of Metal-Doped Hematite for Reduced Surface Recombination in Water Splitting. *ACS Catal.* **2018**, *8* (12), 11932–11939. <https://doi.org/10.1021/acscatal.8b03184>.
- (22) M., K. S. U.; Mofareh, A.-S.; B., I. W. Efficient Photochemical Water Splitting by a Chemically Modified N-TiO₂. *Science* (80-.). **2002**, *297* (5590), 2243–2245. <https://doi.org/10.1126/science.1075035>.
- (23) Ge, M.; Li, Q.; Cao, C.; Huang, J.; Li, S.; Zhang, S.; Chen, Z.; Zhang, K.; Al-Deyab, S. S.; Lai, Y. One-Dimensional TiO₂ Nanotube Photocatalysts for Solar Water Splitting. *Adv. Sci.* **2017**, *4* (1), 1600152. <https://doi.org/https://doi.org/10.1002/advs.201600152>.
- (24) Yang, X.; Wolcott, A.; Wang, G.; Sobo, A.; Fitzmorris, R. C.; Qian, F.; Zhang, J. Z.; Li, Y. Nitrogen-Doped ZnO Nanowire Arrays for Photoelectrochemical Water Splitting. *Nano Lett.* **2009**, *9* (6), 2331–2336. <https://doi.org/10.1021/nl900772q>.
- (25) Zhou, D.; He, M.; Ding, Y.; Yu, J.; Fan, K.; Sun, L. WO₃ Nanosheet-Supported IrW Alloy for High-Performance Acidic Overall Water Splitting with Low Ir Loading. *ACS Appl. Energy Mater.* **2022**, *5* (1), 970–980. <https://doi.org/10.1021/acsaem.1c03358>.
- (26) Yoon, K.-Y.; Park, J.; Lee, H.; Seo, J. H.; Kwak, M.-J.; Lee, J. H.; Jang, J.-H. Unveiling the Role of the Ti Dopant and Viable Si Doping of Hematite for Practically Efficient Solar Water Splitting. *ACS Catal.* **2022**, *12* (9), 5112–5122. <https://doi.org/10.1021/acscatal.1c05106>.
- (27) Kim, J. Y.; Magesh, G.; Youn, D. H.; Jang, J.-W.; Kubota, J.; Domen, K.; Lee, J. S. Single-Crystalline, Wormlike Hematite Photoanodes for Efficient Solar Water Splitting. *Sci. Rep.* **2013**, *3* (1), 2681. <https://doi.org/10.1038/srep02681>.
- (28) Pendlebury, S. R.; Cowan, A. J.; Barroso, M.; Sivula, K.; Ye, J.; Grätzel, M.; Klug, D. R.; Tang, J.; Durrant, J. R. Correlating Long-Lived Photogenerated Hole Populations with Photocurrent Densities in Hematite Water Oxidation Photoanodes. *Energy Environ. Sci.* **2012**, *5* (4), 6304–6312. <https://doi.org/10.1039/C1EE02567H>.
- (29) Yoon, K.-Y.; Lee, J.-S.; Kim, K.; Bak, C. H.; Kim, S.-I.; Kim, J.-B.; Jang, J.-H. Hematite-Based Photoelectrochemical Water Splitting Supported by Inverse Opal Structures of Graphene. *ACS Appl. Mater. Interfaces* **2014**, *6* (24), 22634–22639. <https://doi.org/10.1021/am506721a>.
- (30) Lee, C.-Y.; Wang, L.; Kado, Y.; Killian, M. S.; Schmuki, P. Anodic Nanotubular/Porous Hematite Photoanode for Solar Water Splitting: Substantial Effect of Iron Substrate Purity. *ChemSusChem* **2014**, *7* (3), 934–940. <https://doi.org/https://doi.org/10.1002/cssc.201300603>.

- (31) Mushove, T.; Breault, T. M.; Thompson, L. T. Synthesis and Characterization of Hematite Nanotube Arrays for Photocatalysis. *Ind. Eng. Chem. Res.* **2015**, *54* (16), 4285–4292. <https://doi.org/10.1021/ie504585q>.
- (32) Song, Y.; Qin, S.; Zhang, Y.; Gao, W.; Liu, J. Large-Scale Porous Hematite Nanorod Arrays: Direct Growth on Titanium Foil and Reversible Lithium Storage. *J. Phys. Chem. C* **2010**, *114* (49), 21158–21164. <https://doi.org/10.1021/jp1091009>.
- (33) Morales-Guio, C. G.; Mayer, M. T.; Yella, A.; Tilley, S. D.; Grätzel, M.; Hu, X. An Optically Transparent Iron Nickel Oxide Catalyst for Solar Water Splitting. *J. Am. Chem. Soc.* **2015**, *137* (31), 9927–9936. <https://doi.org/10.1021/jacs.5b05544>.
- (34) Kim, K.; Kim, I.-H.; Yoon, K.-Y.; Lee, J.; Jang, J.-H. α -Fe₂O₃ on Patterned Fluorine Doped Tin Oxide for Efficient Photoelectrochemical Water Splitting. *J. Mater. Chem. A* **2015**, *3* (15), 7706–7709. <https://doi.org/10.1039/C5TA00027K>.
- (35) Qayum, A.; Guo, M.; Wei, J.; Dong, S.; Jiao, X.; Chen, D.; Wang, T. An in Situ Combustion Method for Scale-up Fabrication of BiVO₄ Photoanodes with Enhanced Long-Term Photostability for Unassisted Solar Water Splitting. *J. Mater. Chem. A* **2020**, *8* (21), 10989–10997. <https://doi.org/10.1039/D0TA03557B>.
- (36) Hisatomi, T.; Dotan, H.; Stefik, M.; Sivula, K.; Rothschild, A.; Grätzel, M.; Mathews, N. Enhancement in the Performance of Ultrathin Hematite Photoanode for Water Splitting by an Oxide Underlayer. *Adv. Mater.* **2012**, *24* (20), 2699–2702. <https://doi.org/https://doi.org/10.1002/adma.201104868>.
- (37) Steier, L.; Herraiz-Cardona, I.; Gimenez, S.; Fabregat-Santiago, F.; Bisquert, J.; Tilley, S. D.; Grätzel, M. Understanding the Role of Underlayers and Overlayers in Thin Film Hematite Photoanodes. *Adv. Funct. Mater.* **2014**, *24* (48), 7681–7688. <https://doi.org/https://doi.org/10.1002/adfm.201402742>.
- (38) Ahmed, M. G.; Kretschmer, I. E.; Kandiel, T. A.; Ahmed, A. Y.; Rashwan, F. A.; Bahnemann, D. W. A Facile Surface Passivation of Hematite Photoanodes with TiO₂ Overlayers for Efficient Solar Water Splitting. *ACS Appl. Mater. Interfaces* **2015**, *7* (43), 24053–24062. <https://doi.org/10.1021/acsami.5b07065>.
- (39) Park, J. W.; Mahadik, M. A.; Ma, H.; An, G. W.; Lee, H. H.; Choi, S. H.; Chae, W.-S.; Chung, H.-S.; Jang, J. S. Improved Interfacial Charge Transfer Dynamics and Onset Shift in Nanostructured Hematite Photoanodes via Efficient Ti⁴⁺/Sn⁴⁺ Heterogeneous Self-Doping Through Controlled TiO₂ Underlayers. *ACS Sustain. Chem. Eng.* **2019**, *7* (7), 6947–6958. <https://doi.org/10.1021/acssuschemeng.8b06544>.
- (40) Kang, M. J.; Kang, Y. S. Ultrathin Insulating Under-Layer with a Hematite Thin Film for

- Enhanced Photoelectrochemical (PEC) Water Splitting Activity. *J. Mater. Chem. A* **2015**, *3* (30), 15723–15728. <https://doi.org/10.1039/C5TA03468J>.
- (41) Hu, W.; Liu, T.; Yin, X.; Liu, H.; Zhao, X.; Luo, S.; Guo, Y.; Yao, Z.; Wang, J.; Wang, N.; Lin, H.; Guo, Z. Hematite Electron-Transporting Layers for Environmentally Stable Planar Perovskite Solar Cells with Enhanced Energy Conversion and Lower Hysteresis. *J. Mater. Chem. A* **2017**, *5* (4), 1434–1441. <https://doi.org/10.1039/C6TA09174A>.
- (42) Li, H.; Yin, M.; Li, X.; Mo, R. Enhanced Photoelectrochemical Water Oxidation Performance in Bilayer TiO₂/α-Fe₂O₃ Nanorod Arrays Photoanode with Cu : NiO_x as Hole Transport Layer and Co–Pi as Cocatalyst. *ChemSusChem* **2021**, *14* (11), 2331–2340. <https://doi.org/https://doi.org/10.1002/cssc.202100363>.
- (43) Ahn, H.-J.; Yoon, K.-Y.; Kwak, M.-J.; Jang, J.-H. A Titanium-Doped SiO_x Passivation Layer for Greatly Enhanced Performance of a Hematite-Based Photoelectrochemical System. *Angew. Chemie Int. Ed.* **2016**, *55* (34), 9922–9926. <https://doi.org/10.1002/anie.201603666>.
- (44) Zhang, H.; Kim, Y. K.; Jeong, H. Y.; Lee, J. S. A Few Atomic FeNbO₄ Overlayers on Hematite Nanorods: Microwave-Induced High Temperature Phase for Efficient Photoelectrochemical Water Splitting. *ACS Catal.* **2019**, *9* (2), 1289–1297. <https://doi.org/10.1021/acscatal.8b04034>.
- (45) Yi, Y.; Wu, Q.; Wang, W.; Cui, C. In Situ Depositing an Ultrathin CoO_xH_y Layer on Hematite in Alkaline Media for Photoelectrochemical Water Oxidation. *Appl. Catal. B Environ.* **2020**, *263*, 118334. <https://doi.org/https://doi.org/10.1016/j.apcatb.2019.118334>.
- (46) Jeon, T. H.; Bokare, A. D.; Han, D. S.; Abdel-Wahab, A.; Park, H.; Choi, W. Dual Modification of Hematite Photoanode by Sn-Doping and Nb₂O₅ Layer for Water Oxidation. *Appl. Catal. B Environ.* **2017**, *201*, 591–599. <https://doi.org/https://doi.org/10.1016/j.apcatb.2016.08.059>.
- (47) Li, W.; He, D.; Sheehan, S. W.; He, Y.; Thorne, J. E.; Yao, X.; Brudvig, G. W.; Wang, D. Comparison of Heterogenized Molecular and Heterogeneous Oxide Catalysts for Photoelectrochemical Water Oxidation. *Energy Environ. Sci.* **2016**, *9* (5), 1794–1802. <https://doi.org/10.1039/C5EE03871E>.
- (48) Jin, H.; Guo, C.; Liu, X.; Liu, J.; Vasileff, A.; Jiao, Y.; Zheng, Y.; Qiao, S.-Z. Emerging Two-Dimensional Nanomaterials for Electrocatalysis. *Chem. Rev.* **2018**, *118* (13), 6337–6408. <https://doi.org/10.1021/acs.chemrev.7b00689>.

Chapter 2. Porous hematite synthesis with Ti doped FeOOH OER co-catalyst for efficient photoelectrochemical water splitting system

*Chaper2 is reproduced in part with permission of “Yoon, K.-Y.; Ahn, H.-J.; Kwak, M.-J.; Kim S.-I.; Park, J. and Jang, J.-H.”²⁶ Copyright © 2016, Royal Society of Chemistry.

2.1. Introduction

Various studies have been conducted to manufacture more efficient electrodes by directly solving the fundamental shortcomings of hematite.¹⁻³ Many researchers have attempted to overcome the short hole diffusion length of hematite using nanostructure and have also improve electrical conductivity by doping.^{4,5} Various methods of manufacturing hematite have been developed,⁶⁻⁸ and many challenges have been made with the goal of 10% STH conversion efficiency. Among the various manufacturing methods, price competitiveness, which is one of the biggest advantages of hematite, is sometimes reduced.^{9,10} If the cost of hematite electrodes increases rapidly during the manufacturing process, it is not much different from using precious metal-based photoelectrodes for high-efficiency hydrogen production. Therefore, in order to maximize the advantages of hematite, it is necessary to find the optimal synthesis method in consideration of the electrode manufacturing method and its cost. Figure 2.1 shows the electrode cost and productivity according to various manufacturing methods.¹¹ Among many manufacturing technologies, we have been trying to make hematite electrodes by hydrothermal method since it does not require expensive processes and can have high productivity.¹²⁻¹⁵ In this manufacturing technology, when FTO is immersed in FeCl₃ solution and maintained at a specific temperature for a certain time, FeOOH nanorods are grown on FTO substrate. When the FeOOH nanorods grown on FTO are heat treated at a temperature of 500 °C or higher, FeOOH is changed to Fe₂O₃. At this time, most of the heat treatment at 700 °C or higher has been used. Because the FTO is slightly deformed at a temperature of 700 °C or higher, thereby eliminating the physical boundary for interface between active material and the FTO substrate and at the same time doping the hematite with Sn. High-temperature heat treatment can reduce grain boundaries and obtain doping effect, but hematite also becomes bulkier as it melts at high temperature, which is disadvantageous in terms of the transport of holes and electrons as shown in Figure 2.2.¹⁶ Therefore, it is one of the important challenges to improve the crystallinity of hematite without grain boundaries while preventing hematite coarsening. Herein, we propose a method for manufacturing hematite electrode with an efficient porous structure in the PEC system while preventing hematite coarsening by using SiO_x overlayer as a hard template. In addition, we also present efficient OER co-catalyst design by using developed Ti doped ferric

oxyhydroxide (Ti-FeOOH) co-catalyst on the inner surface (inside pores) of porous hematite with Ti doping (Ti-PH). Our Ti-FeOOH decorated Ti-PH photoanode showed PEC efficiency of above 4 mA cm⁻² at 1.23 V vs. RHE for 36 hours.

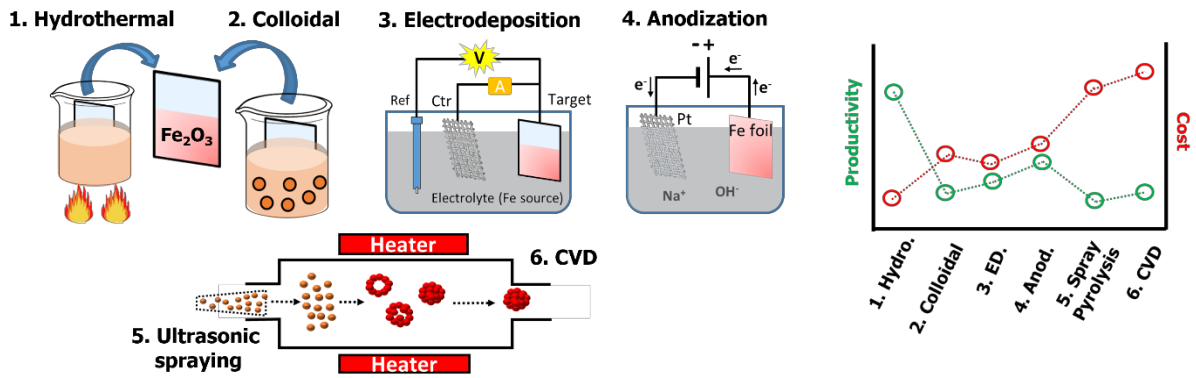


Figure 2.1. Schematic images for various approaches to fabricate hematite electrode and the comparison of productivity and fabrication cost of various technologies.

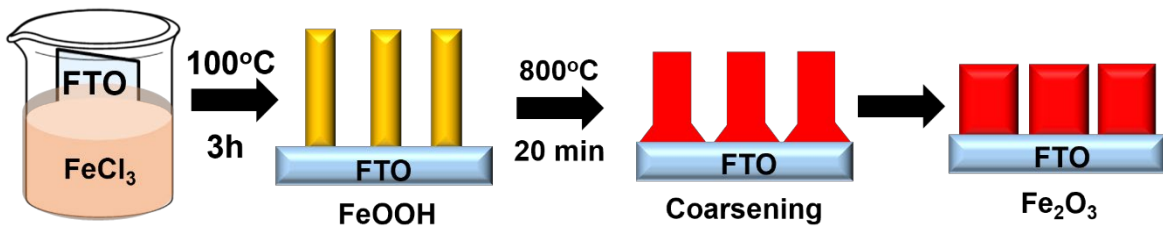


Figure 2.2. Schematic images for representative hydrothermal method for hematite electrode.

2.2. Experimental section

2.2.1 Fabrication of Ti-H photoanode.

For Ti doping into hematite (Ti-H), 7 μl of titanium trichloride (TiCl_3) was injected in 100ml of 150 mM ferric chloride hexahydrate ($\text{FeCl}_3 \cdot 6\text{H}_2\text{O}$). Fluorine-doped tin oxide (FTO) glass was immersed in a vial with a pre-prepared solution. The vial was reacted in an oven at 100 $^\circ\text{C}$ for 3 hours. After the reaction, it can be confirmed that Ti-doped FeOOH nanorods were grown on FTO glass. FTO glass was colored bright yellow by Ti- FeOOH . The FTO substrate on which Ti- FeOOH was grown was annealed at 850 $^\circ\text{C}$ for 20 min in a furnace. As Ti- FeOOH changed to Ti- Fe_2O_3 , the color of electrode became red.

2.2.2 Fabrication of Ti-PH photoanode.

The SiO_x precursor was made by mixing D.I. water:3-(aminopropyl) trimethoxysilane (APTMS)=100:1(v:v). Ti- FeOOH electrode was absorbed in the SiO_x solution for 30 min. After washing SiO_x coated Ti- FeOOH by D.I. water and drying by N_2 gas, SiO_x coated Ti- FeOOH nanorods were annealed at 850 $^\circ\text{C}$ for 20 min to create Ti doped porous hematite Ti-PH.

2.2.3 Fabrication of FeOOH decorated Ti-PH or Ti- FeOOH decorated Ti-PH photoanode.

For the loading of FeOOH co-catalyst on Ti-PH, 1.5 mM of FeCl_3 solution was made and, Ti-PH electrode was dipped in as-prepared solution. The sample was heated to 70 $^\circ\text{C}$ for 30 min. For the loading of Ti- FeOOH co-catalyst, all processes were the same by adding only 7ul of TiCl_3 to the FeCl_3 solution used for the FeOOH co-catalyst.

2.2.4 PEC measurement.

PEC measurements were carried out as half-cell measurements. The half-cell test was based on a three-electrode system made of an Ag/AgCl electrode by KCl saturated solution and a platinum mesh as reference and counter parts, respectively. The exposed area for measuring PEC efficiency was fixed at 0.44 cm^2 by O-ring. The electrolyte was applied as 1M NaOH (pH=13.6) in all PEC measurements. The scan rate is the same for all of them at 20 mVs^{-1} . EIS results were fitted using Z-view software for accurate analysis. IPCE measurement was conducted out by Xe lamp with monochromatic light.

2.3. Results and discussion

Figure 2.3a shows the schematic image for fabricating the porous hematite with Ti doping (Ti-PH) photoanodes represented in this research. Hematite nanorod with Ti doping (Ti-H) by annealed at 850 °C for 20 min is referred as Ti-H. For SiO_x overlayer coating, Ti-FeOOH nanorod is immersed in 3-aminopropyl-trimethoxysilane (APTMS) and annealed at 850 °C for 20 min and then, Ti-FeOOH turned into porous Ti doped hematite with surface SiO_x layer coating and is denoted as Ti-PH. FeOOH decoration is carried out by reacting with 1.5mM FeCl₃ at 70 °C for 30 min. FeOOH coated Ti-PH is referred as FeOOH/Ti-PH. For Ti doping into FeOOH (Ti-FeOOH), an appropriate amount of TiCl₃ is added to the FeCl₃ solution and prepared under the same conditions as FeOOH nanorods. Ti-FeOOH coated Ti-PH is denoted as Ti-FeOOH/Ti-PH. First, we observed scanning electron microscopy (SEM) and transmission electron microscopy (TEM) images to observe the structure of each fabricated electrode as shown in Figure 2.3b-j. The first column in Figures 2.3b, e, and h showed that a distinct porous hematite structure formed by SiO_x overlayer. The thickness of the SiO_x overlayer on hematite surface was found to be 2-5 nm on average. The average size of the pores was 15-30 nm, and the pores could make hematite thinner than typical hematite (Ti-H, ~80 nm) as shown in Figure 2.4. The mechanism by which the pore occurs is as follows: (i) The SiO_x overlayer acted as a hard template, preventing hematite from melting during heat treatment at high temperature. (ii) In the high-temperature heat treatment process, FeOOH is converted to Fe₂O₃, and many water molecules were formed at this time. These water molecules are trapped by SiO_x and pores are formed by the vapors of mass water molecules, making porous structure as shown in Figure 2.5. By forming a porous structure of hematite, it was able to have various advantages for use in the PEC system. First, the surface area is increased. That is, as the number of OER sites increased, it was advantageous for the PEC system. Second, the travel distance of the hole is shortened, indicating that Ti-PH can overcome the problem about the short length of hole diffusion. Third, the co-catalyst can be selectively loaded by using different physical properties of the outer (SiO_x) and inner (Fe₂O₃) surfaces. Except for co-catalysts that have arbitrary photoactivity, co-catalysts can cause light blocking. Therefore, a co-catalyst with high transmittance or a thin coating of the co-catalyst is being developed.^{17,18} From this point of view, Ti-PH can solve the light shielding effect by utilizing the different surface properties of the outside and inside. The second column (Figures 2.3c, f, and i) is images of FeOOH loaded Ti-PH. FeOOH can be easily grown on the hematite surface because the (221) planes of FeOOH match well with the (110) planes of hematite. Therefore, in FeOOH/Ti-PH, FeOOH was rapidly grown to the extent that Ti-PH pores disappeared as shown in Figure 2.6.

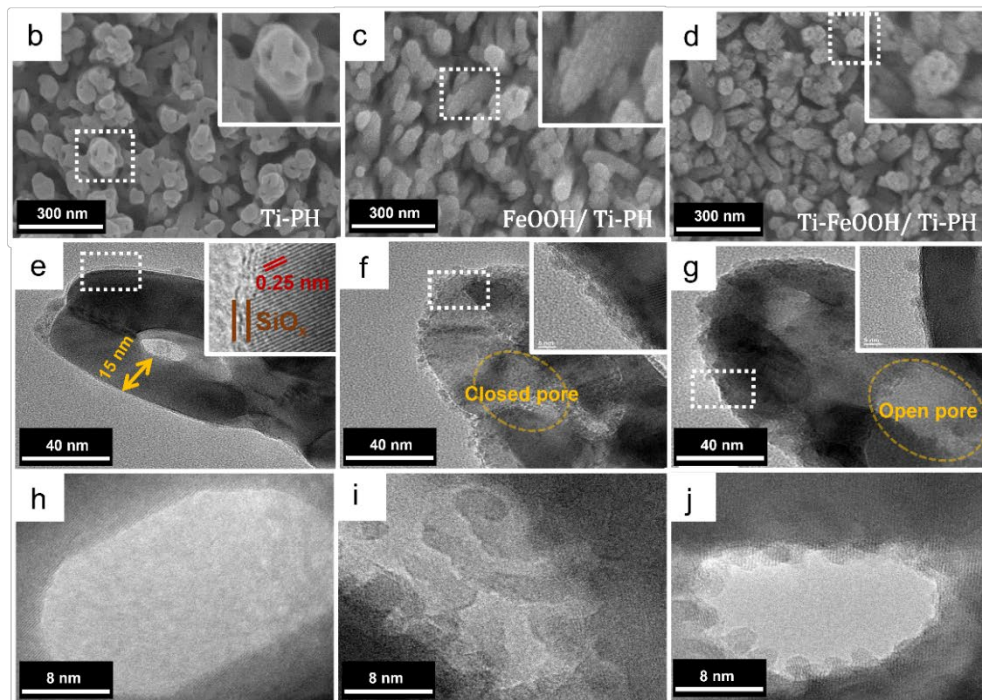
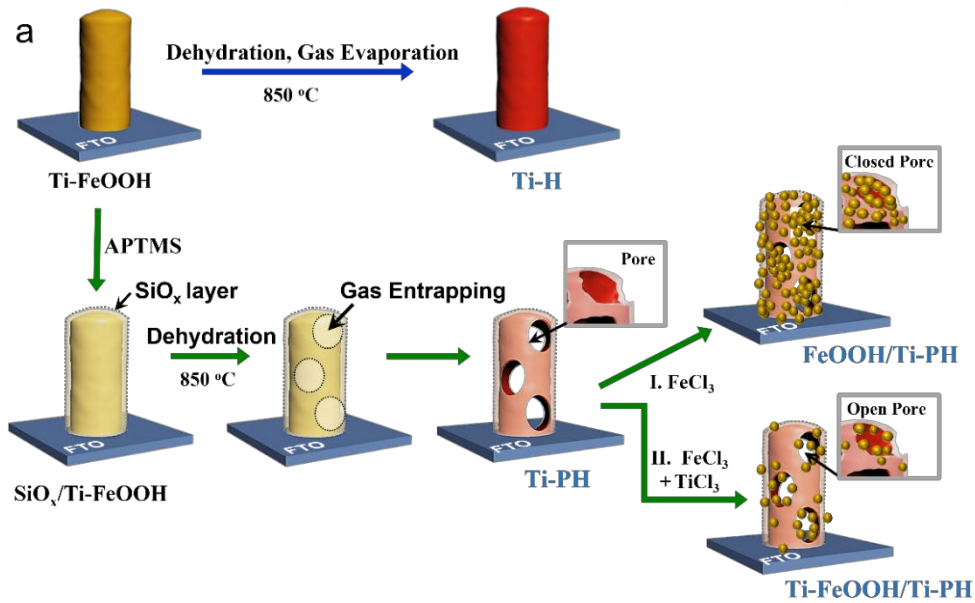


Figure 2.3. (a) Schematic image for preparation of hematite for Ti doping (Ti-H), porous hematite with Ti doping (Ti-PH), FeOOH coated porous hematite with Ti doping (FeOOH/Ti-PH), and Ti-FeOOH coated porous hematite with Ti doping (Ti-FeOOH/Ti-PH). Scanning electron microscopy (SEM) and transmission electron microscopy (TEM) images of Ti-PH (first column, (b, e and h)), FeOOH/Ti-PH (second column, (c, f and i)), and Ti-FeOOH/Ti-PH (third column, (d, g and j)). (b–d) SEM images of three types of photoanode. (e–g) TEM images of a nanorod of three types of photoanode, respectively. The inset images in (b–g) are the zoomed-in images of the rectangle region. (h–j) The zoomed-in images of the inner pore sites in three photoanodes.

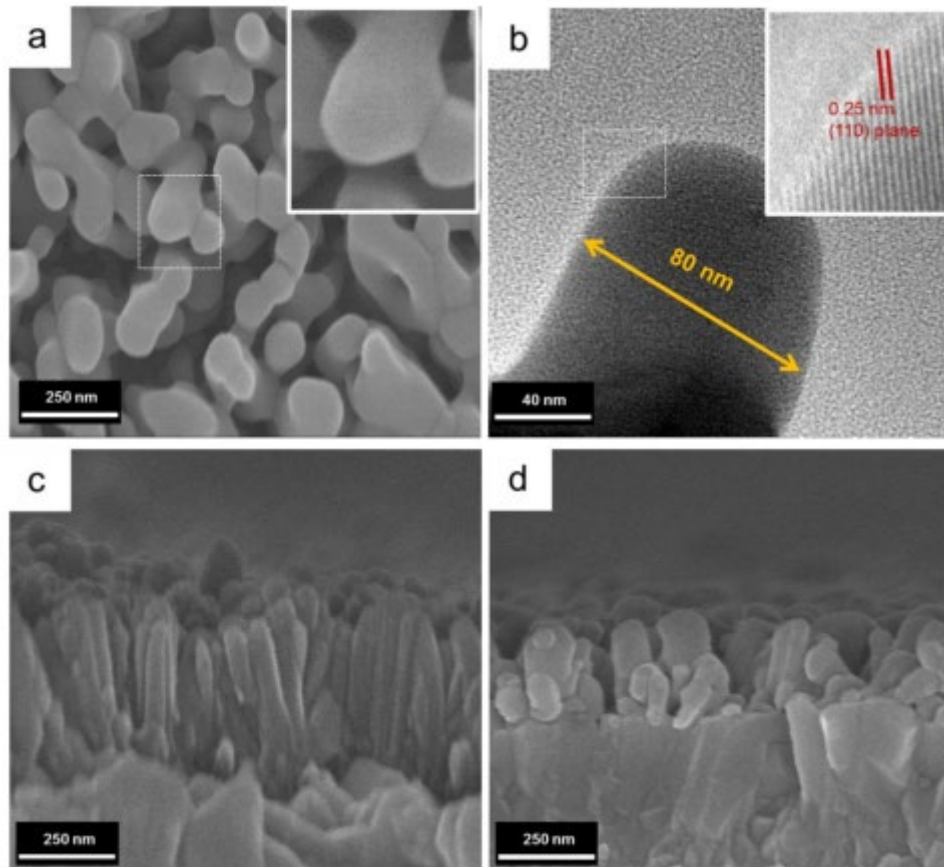


Figure 2.4. (a) SEM image and (b) TEM image of Ti doped hematite. The insert image is the zoomed-in image of the dotted rectangle region. Cross-sectional SEM images of (c) Ti doped FeOOH and (d) Ti doped hematite.

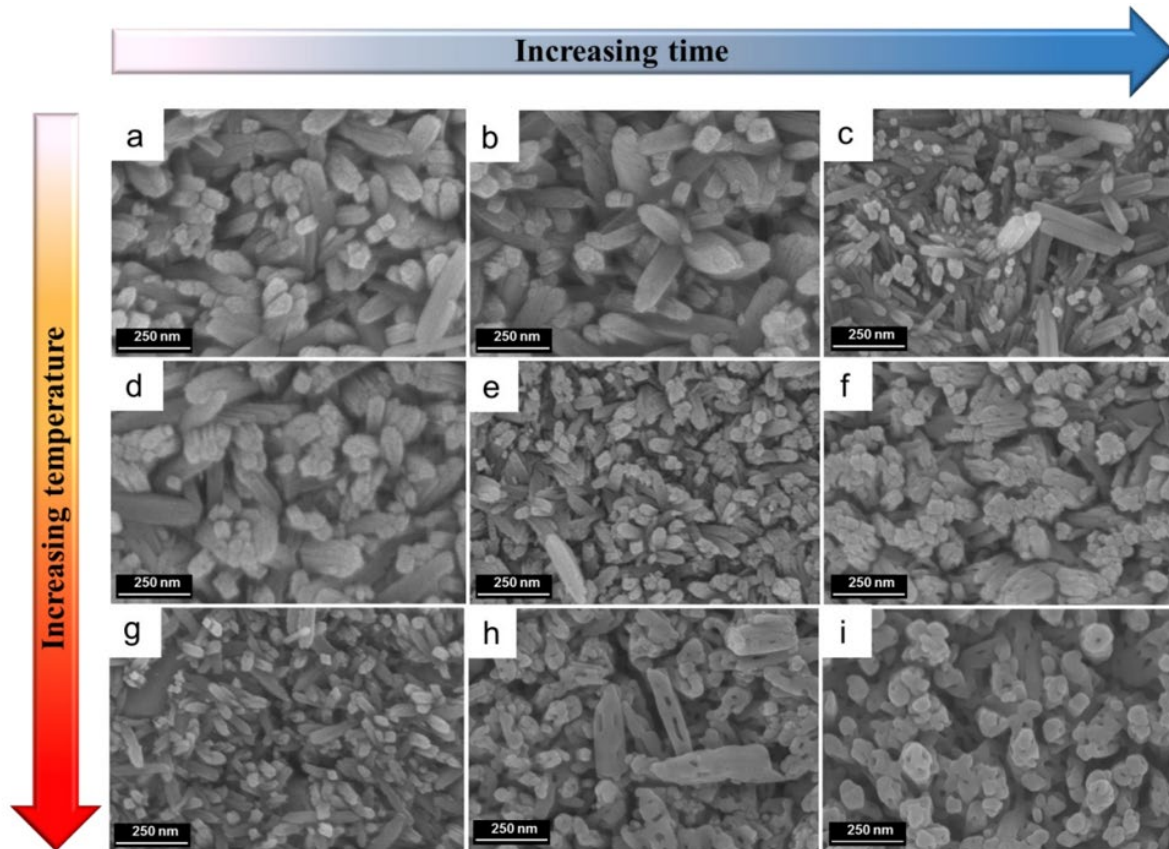


Figure 2.5. Comparison of SEM images by different heat treatment conditions. The time of heat treatment increases from left to right whereas the temperature of heat treatment increases from top to bottom, as shown by the arrows. (a-c) Ti doped porous hematite prepared with various time conditions for 5, 10, and 20 min at fixed temperature (650 °C). (d-f) Ti doped porous hematite made with various time conditions for 5, 10, and 20 min at fixed temperature (750 °C). (g-i) Ti doped porous hematite arranged with various time conditions for 5, 10, and 20 min at fixed temperature (850 °C). Pore generations were observed in (f), (h), and (i), where the electrodes suffered harsh conditions to make enough pressure inside hematite by water vapor.

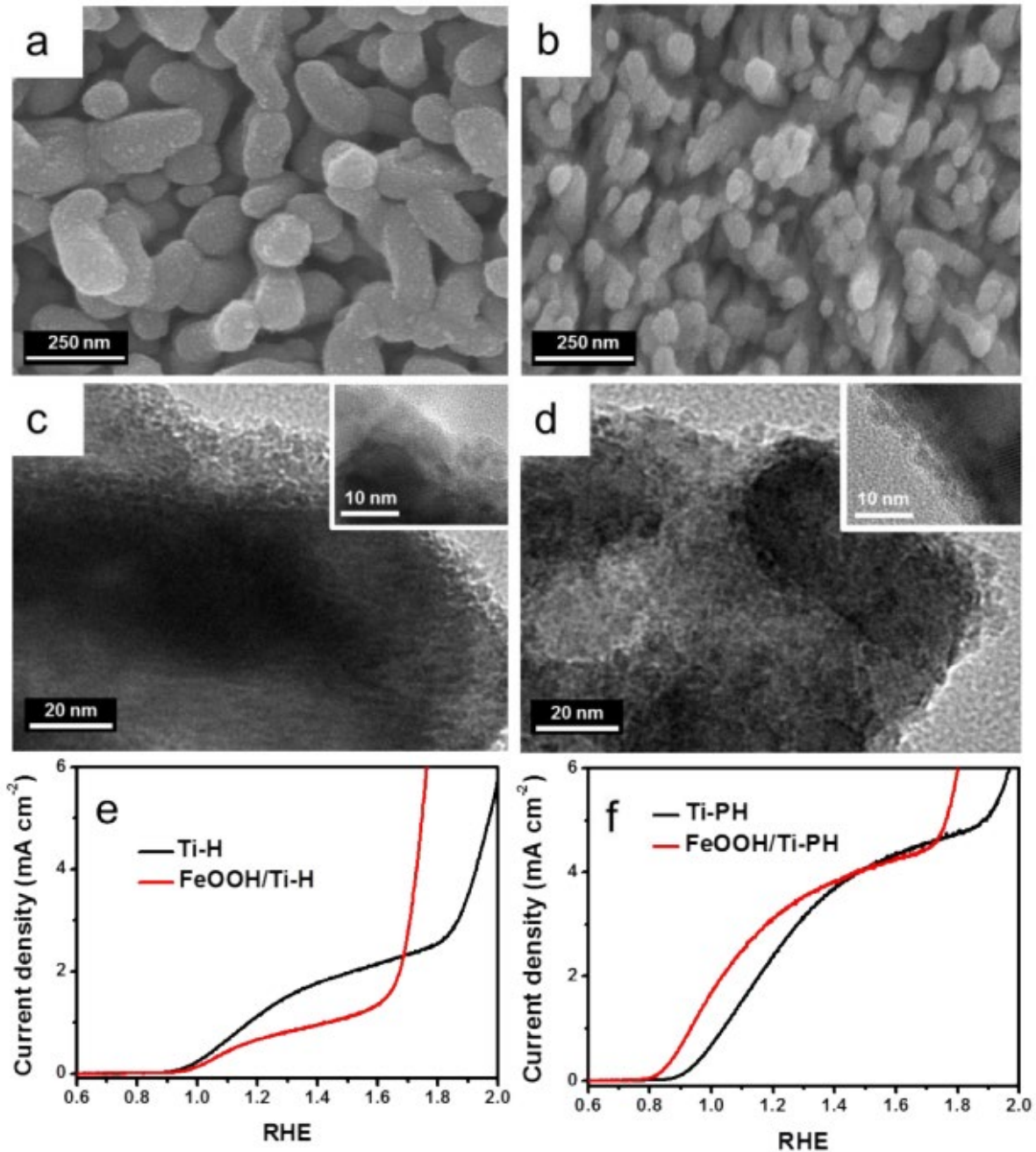


Figure 2.6. Comparison of SEM images of (a) FeOOH loaded Ti doped hematite and (b) FeOOH loaded Ti doped porous hematite. Two electrodes were made by same condition by using 1.5 mM FeCl₃. The comparison of TEM images of (c) FeOOH loaded Ti doped hematite and (d) FeOOH loaded Ti-PH. LSV curves under 1 SUN condition in the basic electrolyte (1 M NaOH) of (e) FeOOH loaded Ti doped hematite and (f) FeOOH loaded Ti doped porous hematite.

After loading FeOOH on Ti-H, the diameter of FeOOH/Ti-H nanorod was much larger than that of Ti-H nanorod. This means that FeOOH is thickly coated on the Ti-H surface, as shown in Figures 2.6a and c. In the case of Ti-PH, it was confirmed that the nanorod of Ti-PH was maintained almost as it was even when FeOOH was coated, as shown in Figures 2.6b and d. This indicates that the growth of FeOOH on the SiO_x surface is more inhibited than on the Fe₂O₃ surface. Therefore, Ti-PH can be effectively used in the PEC system by reducing the light shielding effect on the surface of the photocatalyst when coating the FeOOH co-catalyst, as shown in Figure 2.6e and f. Therefore, FeOOH grows relatively well on the inner pore side with Fe₂O₃ surface, and FeOOH coating was suppressed on the outer surface with SiO_x surface (Figure 2.3 f and i). The third column is images of Ti-FeOOH cocatalyst loaded onto Ti-PH, as shown in Figures 2.3d, g, and h). It was confirmed that the pores of Ti-FeOOH/Ti-PH were maintained differently from FeOOH/Ti-PH. Additional results for the selective adsorption of co-catalysts (FeOOH or Ti-FeOOH) were confirmed in Figures 2.7-2.9. To explain the selective adsorption of co-catalysts (FeOOH or Ti-FeOOH) on the inner surface of Ti-PH, we created nonporous hematite (Ti-H) w/o the SiO_x overlayer using 150 mM FeCl₃ solution. Ti-H coated with SiO_x was achieved by using APTMS solution after manufacturing nonporous hematite (Ti-H). When Ti-FeOOH was loaded on Ti-H with or without SiO_x overlayer, Ti-FeOOH was coated as a thick film in the absence of SiO_x, but in the case of SiO_x overlayer, it was loaded in the form of nanoparticles. Therefore, Ti-FeOOH is also favorably loaded on the Fe₂O₃ surface. The increase in light absorption in UV-vis showed a distinct light shielding effect. It was confirmed that Ti-H without SiO_x significantly increased UV-Vis absorption in 300-600 nm when loading the Ti-FeOOH cocatalyst. However, Ti-H coated with SiO_x showed only a slight increase in UV-Vis absorption. Since Ti-FeOOH has no photoactivity, the increase in UV-Vis absorption means that the intensity of light that hematite can receive is reduced.

Ti-FeOOH showed a low O²⁻ signal of 21% and high OH⁻ signal of 68%, but Ti-H showed a high O²⁻ signal of 60% and low OH⁻ signal of 20% as shown in Figure 2.7a. Therefore, the fact that OH⁻ occupies a relatively high portion compared to O²⁻ portion means that Ti-FeOOH grows well on the hematite surface compared to the SiO_x surface, as shown in Figure 2.7a and b. This also means that Ti-FeOOH grows well on the Fe₂O₃ surface. In addition, it was observed that the size of Ti-FeOOH nanoparticles (2-5 nm) was formed smaller than that of FeOOH nanoparticles (4-8 nm). This is probably because the hydrolysis constant of Ti³⁺ is larger than that of Fe³⁺, preventing the growth of FeOOH, and Ti-doped FeOOH produces smaller size nanoparticles.^{19,20} Smaller size nanoparticles can increase the OER site and reduce the light shielding effect. Therefore, Ti-FeOOH can be utilized for hematite-based electrodes more efficiently than FeOOH.

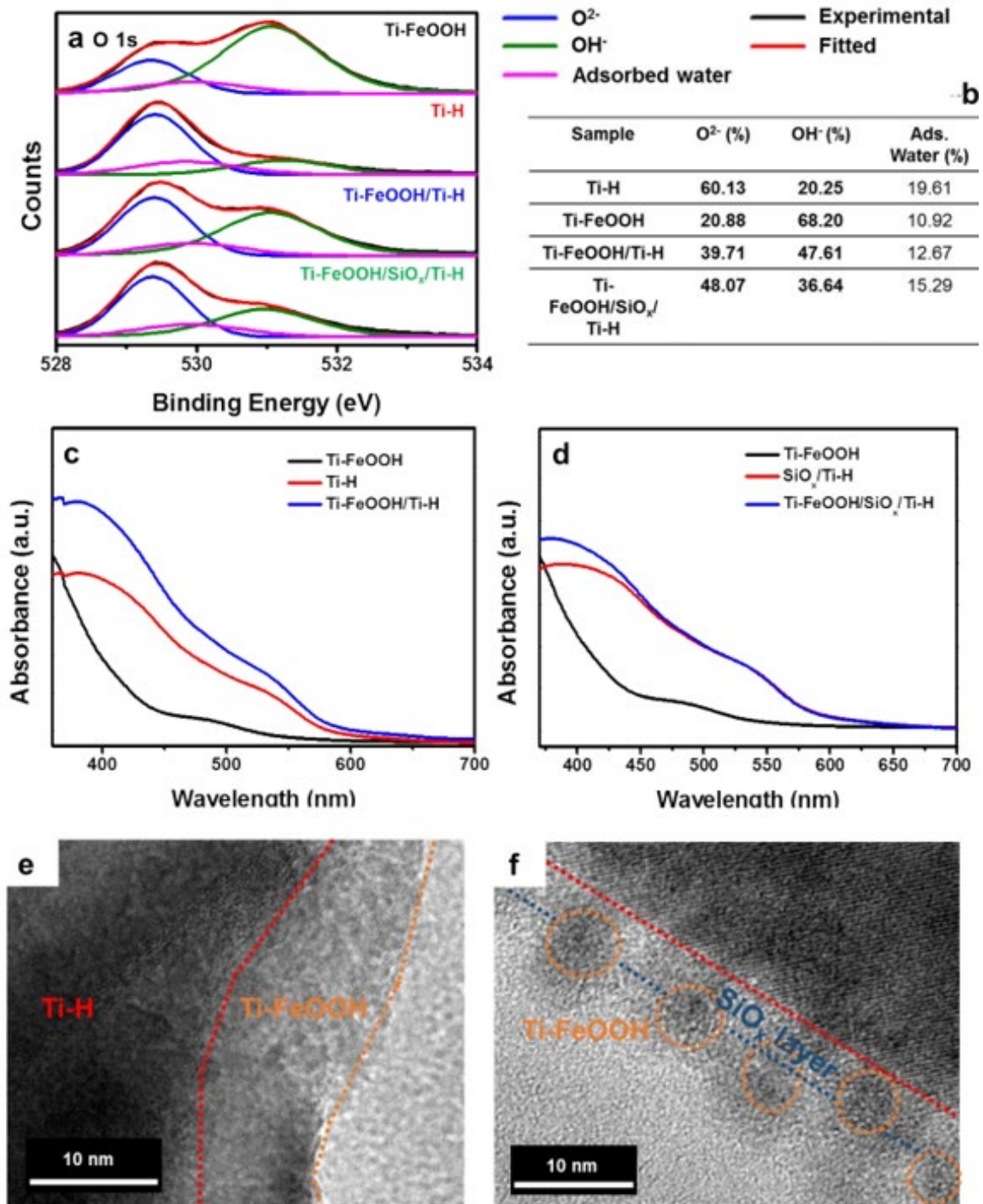


Figure 2.7 XPS spectra of O 1s. (a) of Ti-FeOOH film on FTO glass, Ti-H without SiO_x overlayer, Ti-FeOOH/Ti-H, and TiFeOOH/SiO_x/Ti-H. (b) Deconvolution peaks of O 1s peaks to confirm the relative portion of O²⁻, OH⁻, and adsorbed water. UV-Vis spectra for light shielding effect. (c) Ti-FeOOH/Ti-H and (d) Ti-FeOOH/SiO_x/Ti-H. TEM images of (e) Ti-FeOOH/Ti-H and (f) Ti-FeOOH/SiO_x/Ti-H.

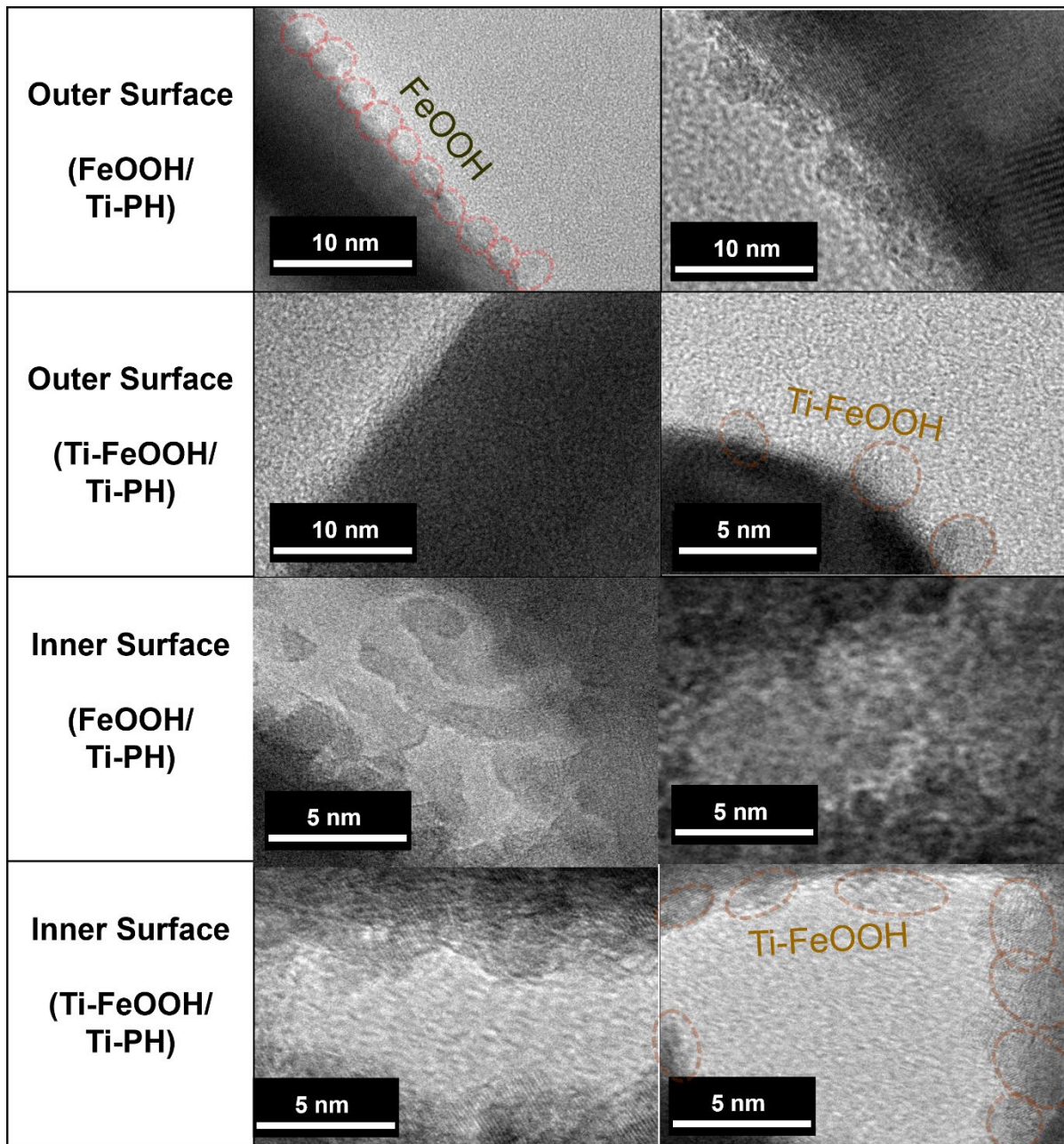


Figure 2.8. Various TEM images to confirm the selective deposition of FeOOH and Ti-FeOOH co-catalyst on outer and inner surface of Ti-PH.

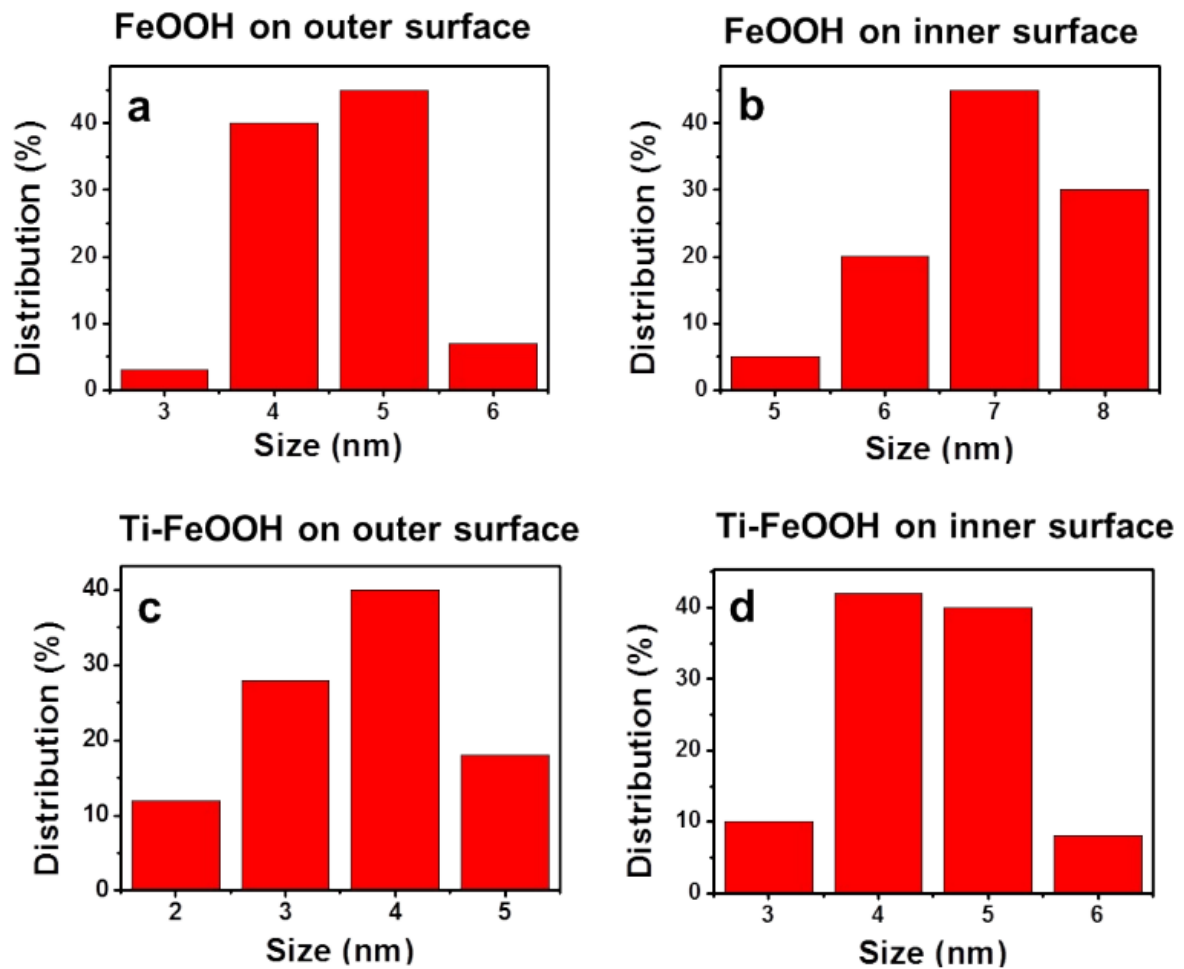


Figure 2.9. Comparison of statistic data for the size distribution of FeOOH co-catalyst nanoparticles on (a) outer and (b) inner surface of Ti-PH and the size distribution of Ti-FeOOH nanoparticles on (c) outer and (d) inner surface of Ti-PH.

By confirming that Ti-FeOOH formed smaller nanoparticles than FeOOH and is advantageous for selective loading on Ti-PH electrode, The following advantages can be obtained from the PEC system: (i) By minimizing the loading of the co-catalyst on the outer surface, the intensity of light received by hematite can be maximized. (ii) Because the pores are maintained, the increased OER site of Ti-PH can be utilized. (iii) The electrical conductivity of the cocatalyst is improved due to Ti doping, making electron transport easier as shown in Figure 2.10. FeOOH or Ti-FeOOH co-catalyst loaded on Ti-PH were observed by XPS measurements as shown in Figure 2.11. Considering the X-ray penetration depth (around 5 nm) for the XPS measurement, the XPS signal for Ti 2p peak was not detected from the FeOOH co-catalyst on the surface of Ti-PH since the thickness of FeOOH was above 5 nm in our limited system. The XPS signals for OH⁻ (529.7 eV), O₂⁻ (529.0 eV), and adsorbed water (530.8 eV) were confirmed on O 1s peaks of FeOOH film. Comparing the O 1s of FeOOH and Ti-FeOOH, it was confirmed that the O 1s signals of Ti-FeOOH were overall upshifted. This means that FeOOH is well doped with Ti as previously reported work.²¹ Figure 2.12a compared the LSV curves of 4 types of electrodes with front side illumination. Ti-H showed a photocurrent density of about 1.2 mA cm⁻² at 1.23V_{RHE}, and Ti-PH showed a photocurrent density of about 2.4 mA cm⁻² at 1.23V_{RHE}, which was increased by about two times compared to Ti-H. The reason for the improvement is increased surface area and reduced hole travel due to porosity of Ti-PH, as mentioned above. After loading FeOOH on Ti-PH, FeOOH/Ti-PH showed a photocurrent density of about 3.3 mA cm⁻², which was about 1.4 times higher than that of Ti-PH. Ti-FeOOH/Ti-PH showed the photocurrent density of above 4 mA cm⁻², which was around 3 times higher than that of Ti-H with proper faradaic efficiency of 85-90 % as shown in Figure 2.13. We analyze the OER performance of the four types of electrodes, the LSV was measured under dark conditions as shown in Figure 2.12b. The OER performance of Ti-PH was better than that of Ti-H by porous structure. After loading FeOOH cocatalyst, FeOOH/Ti-PH showed better OER performance than Ti-PH since FeOOH has a faster OER kinetic than hematite. Interestingly, Ti-PH loaded with Ti-FeOOH showed worse OER performance than FeOOH/Ti-PH. This is probably expected to be caused by the difference in the loading amount of the co-catalyst. To clearly demonstrate this, we confirmed the FeOOH and Ti-FeOOH film with similar amount loading on FTO glass as shown in Figure 2.14a. As can be seen in the LSV curves, it was shown that the OER kinetic of Ti-FeOOH was much faster than that of FeOOH. This reason is described by the different values in zeta potential measurement caused by Ti doping. By doping with Ti, the zeta potential value (from -30.7 to -24.6 mV) becomes more positive due to Ti⁴⁺, and the adsorption of OH⁻ can be further promoted in the electrolytes by shuttling more OH⁻ ions to the OER mechanism in Figure 2.14b and c.²²⁻²⁴ Besides, Ti-FeOOH has outstanding electrical property by Ti doping compared to FeOOH as shown in Figure 2.10, which makes electron generated during oxygen evolution reaction move fast through Ti-FeOOH co-catalyst.

Therefore, Ti-FeOOH can have faster OER kinetic than FeOOH. Electrochemical impedance spectroscopy (EIS) was conducted at the range of 100kHz to 0.1 Hz frequency in the same electrolyte under 1 SUN illumination to understand photoelectrochemical behavior for co-catalyst. Fig. 2.12c showed the EIS curves to investigate the influence on the interface of co-catalyst/Fe₂O₃ and the interface of electrolyte/electrode. The resistance of charge transfer (R_{ct} value) of Ti-PH was lower than that of Ti-H, indicating that porous structure can increase the OER sites. In FeOOH coated Ti-PH, FeOOH can further reduce the resistance of charge transfer by improving the OER kinetic and after loading on Ti-FeOOH on Ti-PH, the additional decrease of the resistance of charge transfer was confirmed. This means that the resistance of charge transfer between the electrolyte and the surface of Ti-FeOOH/Ti-PH is lowest, demonstrating the better OER kinetic of Ti-FeOOH than that of FeOOH, and modified surface decoration with co-catalyst achieved by efficiently receiving the light due to low co-catalyst concentration on the hematite surface in the case of the Ti-FeOOH co-catalyst. In addition, the onset points in EIS curves in the high frequency region, which implies the resistance of sheet (R_s), was almost similar for all samples, proving that the pore creation or the decoration of Ti-FeOOH or FeOOH on hematite electrode did not affect the resistance between hematite and FTO substrate. The details for fitted experimental results were summarized in Table 2.1. The chopped curves of electrodes presented the stable curve shapes without any change at 1.23V_{RHE}, indicating that SiO_x, FeOOH, and Ti-FeOOH has good stability in basic electrolyte without any side reactions. The IPCE spectra can directly explain the light shielding effect. We conducted IPCE measurement at 1.23V_{RHE}. Ti-PH showed higher IPCE efficiency in 300-700 nm than that of Ti-H indicating that Ti-PH is more photoactive material as shown in Figure 2.12e. When Ti-FeOOH co-catalysts were loaded on the surface of Ti-PH, the IPCE values were increased, and Ti-FeOOH/Ti-PH showed the highest IPCE results over the wide range reaching 66% at 300 nm and 92% at 400 nm. The IPCE values of FeOOH/Ti-PH steadily decreased from 320 to 580 nm compared with Ti-FeOOH/Ti-PH, in which the FeOOH loaded Ti-PH photoanode (dark yellow dot) showed strong UV-vis absorption, as shown in Figure 2.12f. Therefore, the light shielding effect by the co-catalyst that we claim can adversely affect the semiconductor in the PEC system, and an efficient design for photoelectrode is needed to solve this.

Our Ti-FeOOH co-catalyst has the ability of selective decoration in inner pores rather than outer surface. and loading amount can be adjusted with density control on the surface of hematite. We confirmed the PEC efficiency by LSV curve (Figure 2.16a) with the long-term stability (Figure 2.16b) of Ti-PH photoanodes coupled with representative other co-catalysts. The photocurrent density of Co-Pi/Ti-PH or IrO₂/Ti-PH at 1.23 V vs. RHE measured is similar to previous values as reported and Ti-FeOOH decorated Ti-PH showed is the best PEC efficiency as shown in Figures 2.16a and b. Although Co-Pi or IrO₂ are a representative and excellent co-catalysts having outstanding OER properties, it is difficult

to control the loading amount of co-catalyst content between the inner and outer surface in our hematite with porous structure, as shown in Figure 2.16c. Thus, our modified FeOOH with Ti doping co-catalyst reached the highest efficiency by improving the light absorption to reduce the light shielding effect of hematite, as shown in Figure 2.16d. To demonstrate the long-term stability of our photoanode, we confirmed photocurrent density at fixed voltage (1.23 V vs. RHE) under 1 SUN illumination. Our Ti-FeOOH decorated Ti-PH showed little decrease in the photocurrent density for 36 hours (Figure 2.16). This means that the SiO_x overlayer and Ti-FeOOH co-catalyst can be used for a long time in the basic electrolyte. For IrO₂ nanoparticle loaded Ti-PH, IrO₂/Ti-PH photoanode confirmed that the PEC efficiency gradually decreased. This is because IrO₂ is simply physically adsorbed and bubbles are generated during the photoelectrochemical water oxidation, and PEC efficiency decreases as the particles gradually detached from the surface of Ti-PH, as reported.²⁵

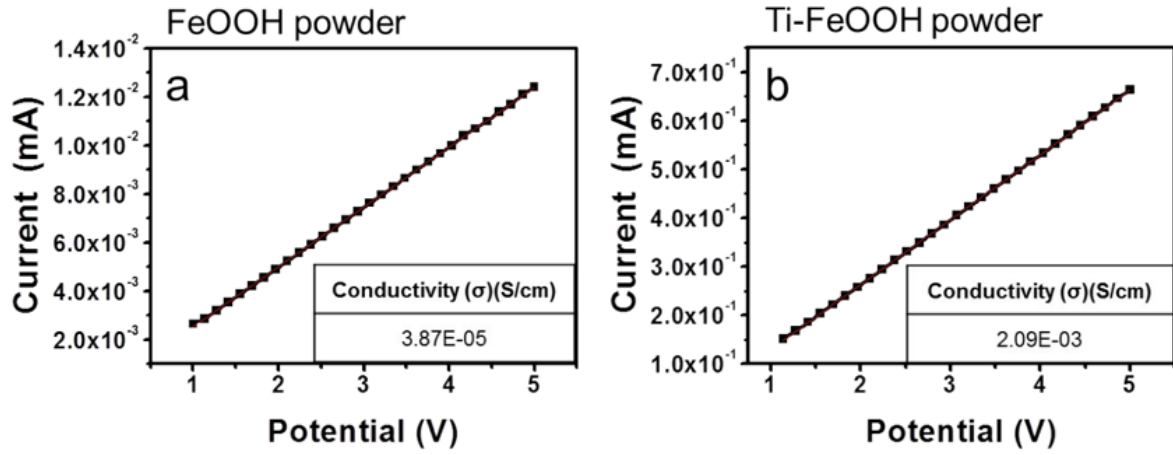


Figure 2.10. Electrical conductivity measurements by (a) FeOOH and (b)Ti-FeOOH powders.

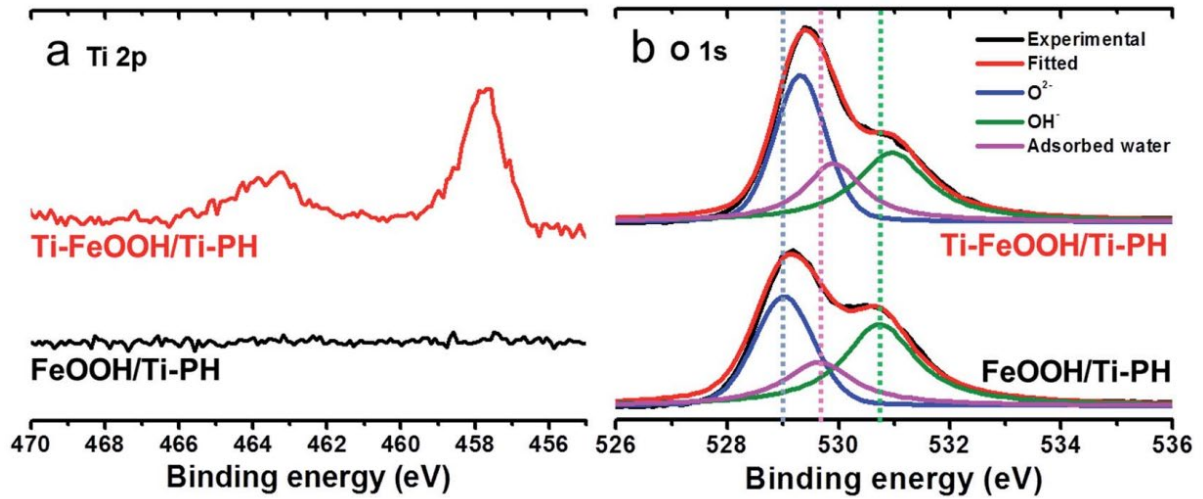


Figure 2.11. (a) Ti 2p peaks and (b) O 1s peaks of FeOOH/Ti-PH and Ti-FeOOH/Ti-PH.

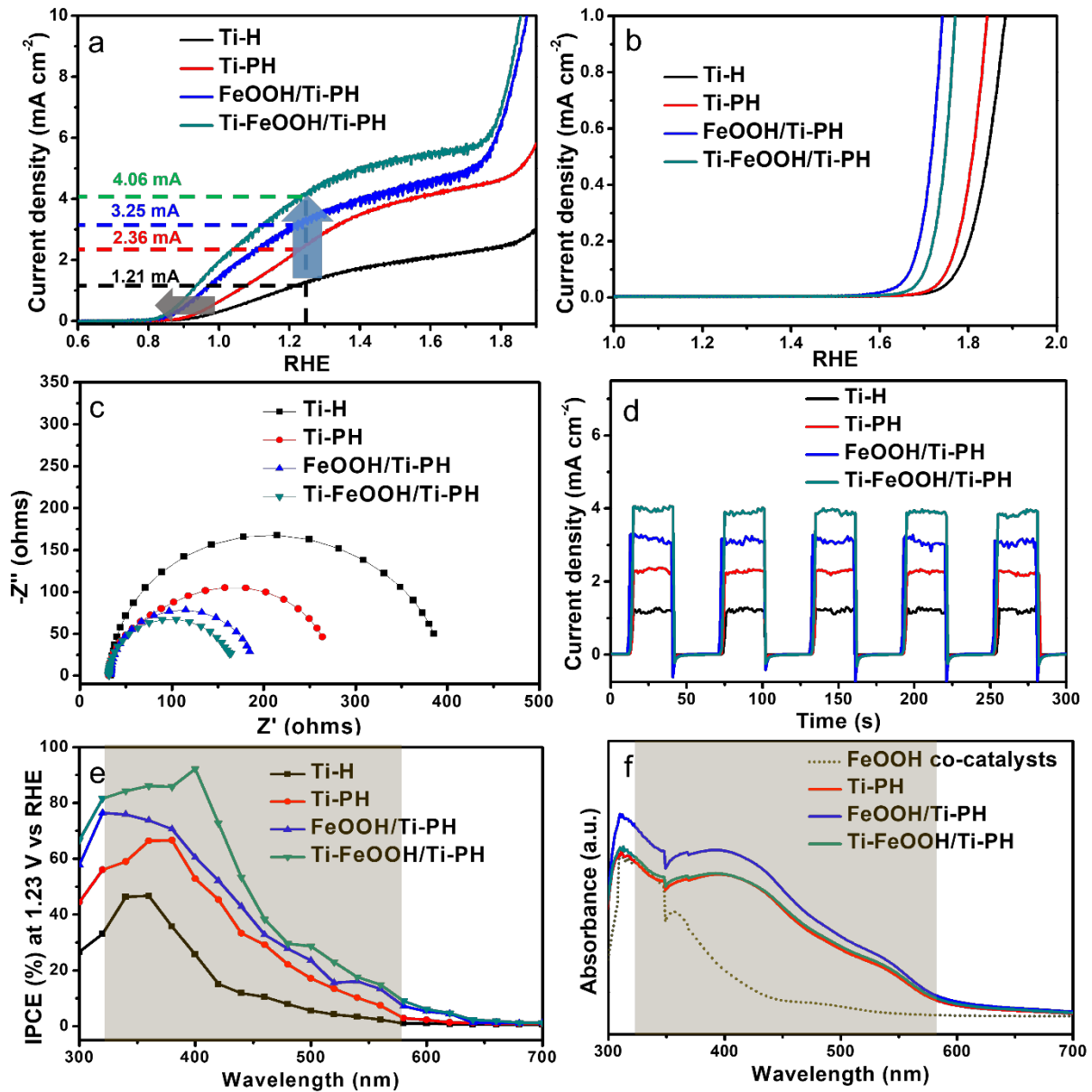


Figure 2.12. Comparison of LSV curves of each photoanode in 1M NaOH under (a) light and (b) dark conditions. (c) Electrochemical impedance spectroscopy (EIS) curves at 1.23 V vs. RHE. (d) Stability test with chopped light conditions at 1.23 V vs. RHE. (e) IPCE spectra for each sample measured at 1.23 V vs. RHE. (f) Normalized UV-Vis absorption spectrum.

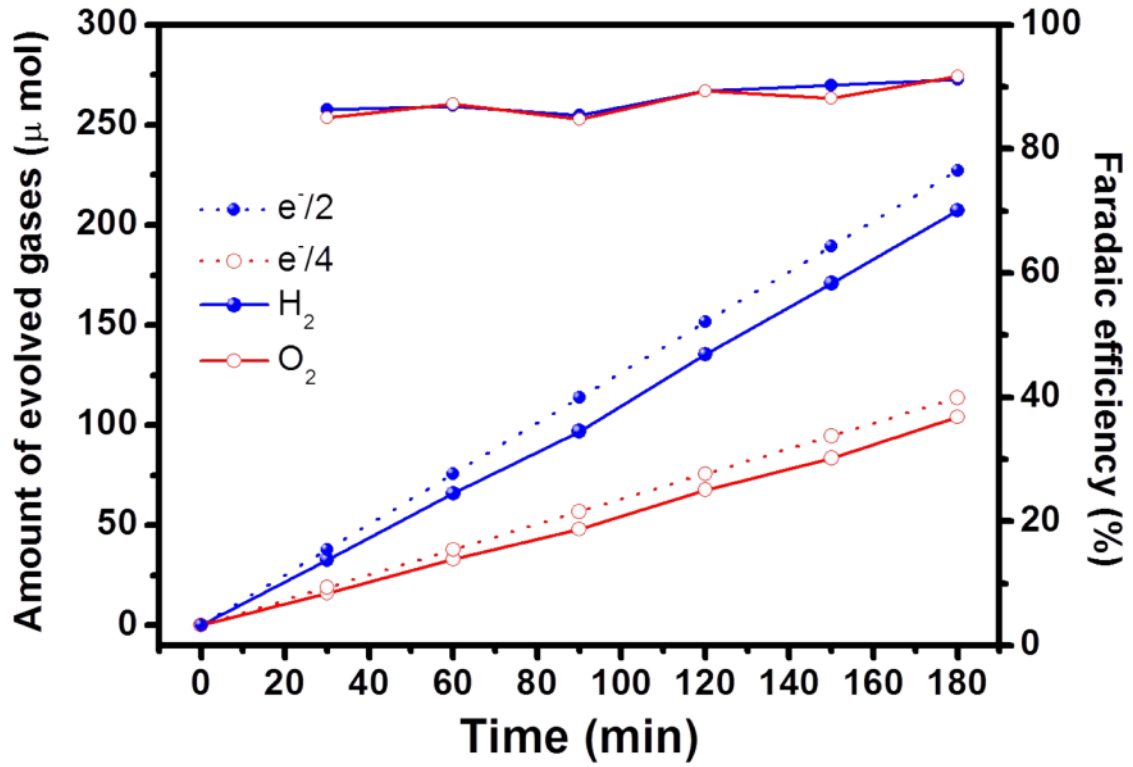


Figure 2.13. Faradaic efficiency of Ti-FeOOH/Ti-PH at 1.23 V vs RHE under AM 1.5 illumination in a 1 M NaOH electrolyte.

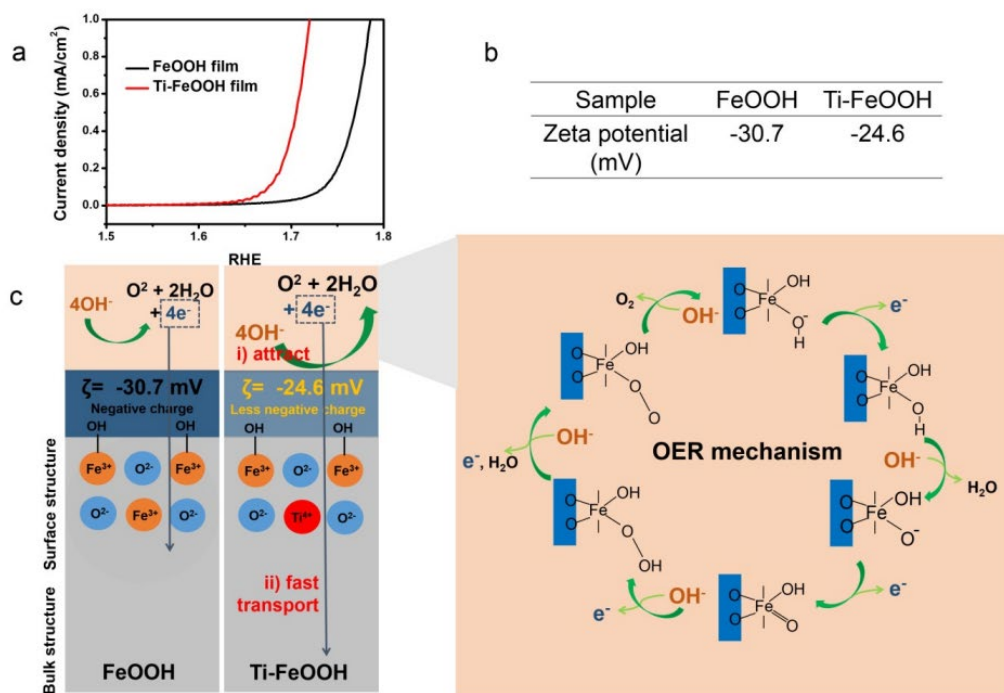


Figure 2.14. (a) LSV curves in 1M NaOH under the dark condition. For same concentration of FeOOH and Ti-FeOOH, film type electrode was made on FTO substrate. (b) Zeta potential measurement. (c) Scheme of the OER mechanism by FeOOH and Ti-FeOOH.

$R/\Omega \text{ cm}^2$	R_{bulk}	R_{CT}
Ti-H	70.5	290.6
Ti-PH	55.5	188.0
FeOOH/Ti-PH	54.5	156.8
Ti-FeOOH/Ti-PH	48.1	132.4

Table 2.1. The values by fitted resistance calculated from the EIS results.

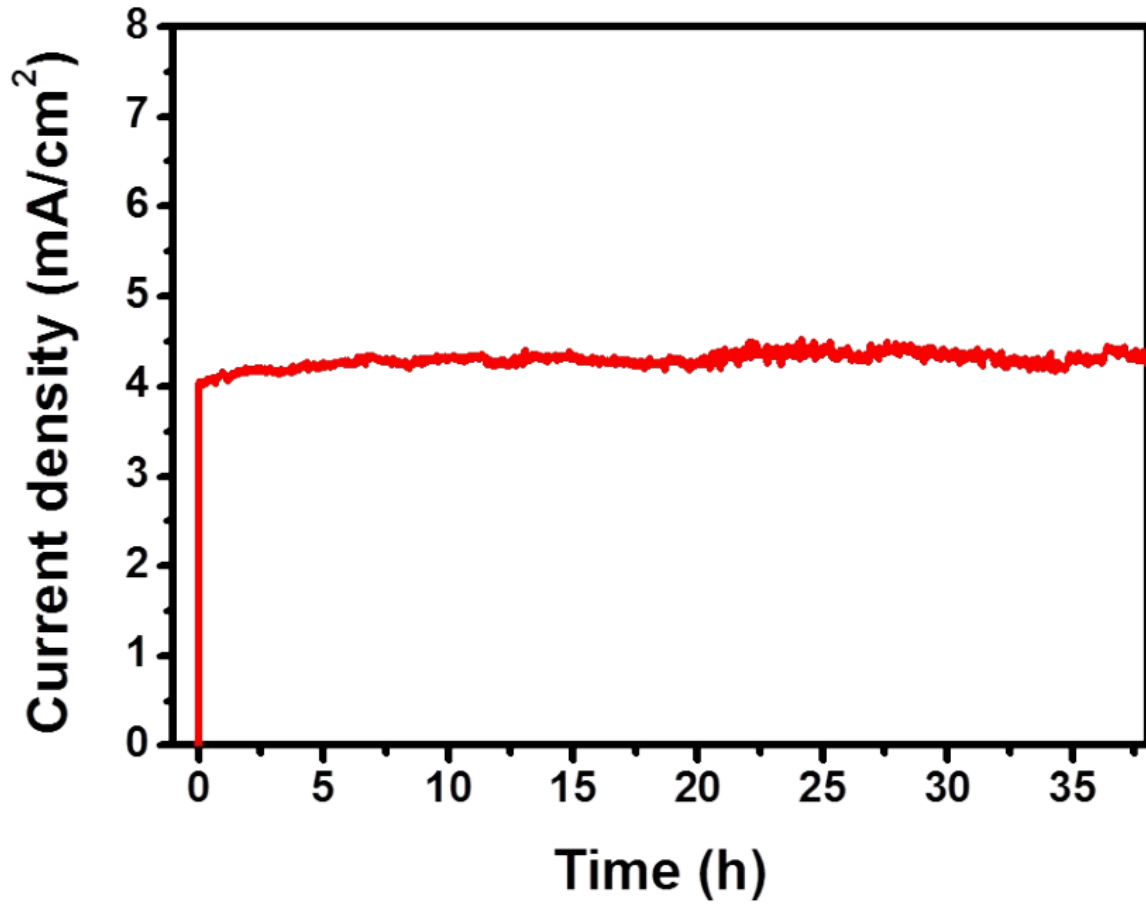


Figure 2.15. Long-term stability of Ti-FeOOH/Ti-PH.

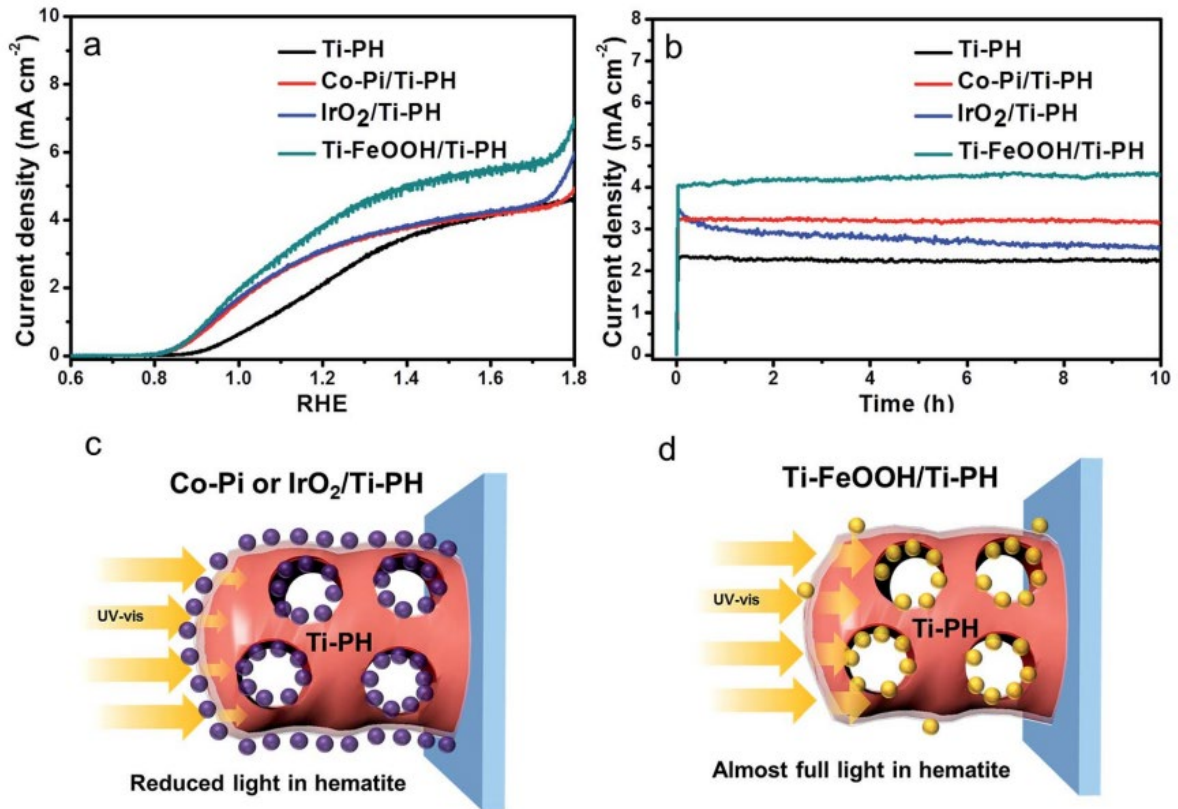


Figure 2.16. (a) LSV curves with various co-catalyst and (b) long-term stability with representative co-catalyst loaded on Ti-PH. Schematic images to the light absorption by co-catalyst and light shielding effect of (c) Co-Pi or IrO₂ deposited Ti-PH and (d) Ti-FeOOH/Ti-PH.

2.4. Conclusion

In summary, we have demonstrated how to manufacture porous hematite with a more efficient structure by using SiO_x overlayer. The efficient structure showed approximately double the PEC efficiency compared to the general nonporous structure. In addition, when creating a porous structure using an overlayer, the physical properties of the outer and inner surfaces of hematite were different. The catalytic effect was further amplified by Ti doping into FeOOH, one of the representative oxygen evolution catalysts, by improving the electrical conductivity. Utilizing the similar crystal planes of FeOOH and Fe_2O_3 , we succeeded in selectively growing Ti-FeOOH in the inner pores to minimize the light shielding effect by co-catalyst. As a result, superior PEC performance and excellent stability were secured compared to Co-Pi, IrO_2 , or FeOOH catalysts. Our research results can suggest ways to utilize the optimized design of efficient hematite fabrication and catalyst utilization without any specific equipment.

2.5. References

- (1) Kim, J. Y.; Magesh, G.; Youn, D. H.; Jang, J.-W.; Kubota, J.; Domen, K.; Lee, J. S. Single-Crystalline, Wormlike Hematite Photoanodes for Efficient Solar Water Splitting. *Sci. Rep.* **2013**, *3* (1), 2681. <https://doi.org/10.1038/srep02681>.
- (2) Ahn, H.-J.; Yoon, K.-Y.; Kwak, M.-J.; Park, J.; Jang, J.-H. Boron Doping of Metal-Doped Hematite for Reduced Surface Recombination in Water Splitting. *ACS Catal.* **2018**, *8* (12), 11932–11939. <https://doi.org/10.1021/acscatal.8b03184>.
- (3) Cao, D.; Luo, W.; Feng, J.; Zhao, X.; Li, Z.; Zou, Z. Cathodic Shift of Onset Potential for Water Oxidation on a Ti⁴⁺ Doped Fe₂O₃ Photoanode by Suppressing the Back Reaction. *Energy Environ. Sci.* **2014**, *7* (2), 752–759. <https://doi.org/10.1039/C3EE42722F>.
- (4) Li, C.; Li, A.; Luo, Z.; Zhang, J.; Chang, X.; Huang, Z.; Wang, T.; Gong, J. Surviving High-Temperature Calcination: ZrO₂-Induced Hematite Nanotubes for Photoelectrochemical Water Oxidation. *Angew. Chemie Int. Ed.* **2017**, *56* (15), 4150–4155. <https://doi.org/10.1002/anie.201611330>.
- (5) Lan, H.; Xia, Y.; Feng, K.; Wei, A.; Kang, Z.; Zhong, J. Co-Doped Carbon Layer to Lower the Onset Potential of Hematite for Solar Water Oxidation. *Appl. Catal. B Environ.* **2019**, *258*, 117962. <https://doi.org/10.1016/j.apcatb.2019.117962>.
- (6) Zhou, Z.; Huo, P.; Guo, L.; Prezhdo, O. V. Understanding Hematite Doping with Group IV Elements: A DFT+U Study. *J. Phys. Chem. C* **2015**, *119* (47), 26303–26310. <https://doi.org/10.1021/acs.jpcc.5b08081>.
- (7) Puthirath Balan, A.; Radhakrishnan, S.; Woellner, C. F.; Sinha, S. K.; Deng, L.; Reyes, C. de los; Rao, B. M.; Paulose, M.; Neupane, R.; Apte, A.; Kochat, V.; Vajtai, R.; Harutyunyan, A. R.; Chu, C.-W.; Costin, G.; Galvao, D. S.; Martí, A. A.; van Aken, P. A.; Varghese, O. K.; Tiwary, C. S.; Malie Madom Ramaswamy Iyer, A.; Ajayan, P. M. Exfoliation of a Non-van Der Waals Material from Iron Ore Hematite. *Nat. Nanotechnol.* **2018**, *13* (7), 602–609. <https://doi.org/10.1038/s41565-018-0134-y>.
- (8) Kong, T.-T.; Huang, J.; Jia, X.-G.; Wang, W.-Z.; Zhou, Y.; Zou, Z.-G. Nitrogen-Doped Carbon Nanolayer Coated Hematite Nanorods for Efficient Photoelectrocatalytic Water Oxidation. *Appl. Catal. B Environ.* **2020**, *275*, 119113. <https://doi.org/10.1016/j.apcatb.2020.119113>.
- (9) Cesar, I.; Kay, A.; Gonzalez Martinez, J. A.; Grätzel, M. Translucent Thin Film Fe₂O₃ Photoanodes for Efficient Water Splitting by Sunlight: Nanostructure-Directing Effect of Si-Doping. *J. Am. Chem. Soc.* **2006**, *128* (14), 4582–4583. <https://doi.org/10.1021/ja060292p>.
- (10) Chemelewski, W. D.; Hahn, N. T.; Mullins, C. B. Effect of Si Doping and Porosity on Hematite's (α -Fe₂O₃) Photoelectrochemical Water Oxidation Performance. *J. Phys. Chem. C* **2012**, *116* (8), 5255–5261. <https://doi.org/10.1021/jp210877u>.
- (11) Tamirat, A. G.; Rick, J.; Dubale, A. A.; Su, W.-N.; Hwang, B.-J. Using Hematite for Photoelectrochemical Water Splitting: A Review of Current Progress and Challenges. *Nanoscale Horizons* **2016**, *1* (4), 243–267. <https://doi.org/10.1039/C5NH00098J>.
- (12) Kim, K.; Kim, I.-H.; Yoon, K.-Y.; Lee, J.; Jang, J.-H. α -Fe₂O₃ on Patterned Fluorine Doped Tin Oxide for Efficient Photoelectrochemical Water Splitting. *J. Mater. Chem. A* **2015**, *3* (15), 7706–7709. <https://doi.org/10.1039/C5TA00027K>.

- (13) Ahn, H.-J.; Yoon, K.-Y.; Kwak, M.-J.; Lee, J.-S.; Thiagarajan, P.; Jang, J.-H. MoS_x Supported Hematite with Enhanced Photoelectrochemical Performance. *J. Mater. Chem. A* **2015**, *3* (43), 21444–21450. <https://doi.org/10.1039/C5TA06743J>.
- (14) Monllor-Satoca, D.; Bärtsch, M.; Fàbrega, C.; Genç, A.; Reinhard, S.; Andreu, T.; Arbiol, J.; Niederberger, M.; Morante, J. R. What Do You Do, Titanium? Insight into the Role of Titanium Oxide as a Water Oxidation Promoter in Hematite-Based Photoanodes. *Energy Environ. Sci.* **2015**, *8* (11), 3242–3254. <https://doi.org/10.1039/C5EE01679G>.
- (15) Zhang, H.; Li, D.; Byun, W. J.; Wang, X.; Shin, T. J.; Jeong, H. Y.; Han, H.; Li, C.; Lee, J. S. Gradient Tantalum-Doped Hematite Homo Junction Photoanode Improves Both Photocurrents and Turn-on Voltage for Solar Water Splitting. *Nat. Commun.* **2020**, *11* (1), 4622. <https://doi.org/10.1038/s41467-020-18484-8>.
- (16) Annamalai, A.; Subramanian, A.; Kang, U.; Park, H.; Choi, S. H.; Jang, J. S. Activation of Hematite Photoanodes for Solar Water Splitting: Effect of FTO Deformation. *J. Phys. Chem. C* **2015**, *119* (7), 3810–3817. <https://doi.org/10.1021/jp512189c>.
- (17) Morales-Guio, C. G.; Mayer, M. T.; Yella, A.; Tilley, S. D.; Grätzel, M.; Hu, X. An Optically Transparent Iron Nickel Oxide Catalyst for Solar Water Splitting. *J. Am. Chem. Soc.* **2015**, *137* (31), 9927–9936. <https://doi.org/10.1021/jacs.5b05544>.
- (18) Kim, J. Y.; Youn, D. H.; Kang, K.; Lee, J. S. Highly Conformal Deposition of an Ultrathin FeOOH Layer on a Hematite Nanostructure for Efficient Solar Water Splitting. *Angew. Chemie Int. Ed.* **2016**, *55* (36), 10854–10858. <https://doi.org/https://doi.org/10.1002/anie.201605924>.
- (19) Shen, S.; Kronawitter, C. X.; Wheeler, D. A.; Guo, P.; Lindley, S. A.; Jiang, J.; Zhang, J. Z.; Guo, L.; Mao, S. S. Physical and Photoelectrochemical Characterization of Ti-Doped Hematite Photoanodes Prepared by Solution Growth. *J. Mater. Chem. A* **2013**, *1* (46), 14498–14506. <https://doi.org/10.1039/C3TA13453A>.
- (20) Pecsok, R. L.; Fletcher, A. N. Hydrolysis of Titanium(III). *Inorg. Chem.* **1962**, *1* (1), 155–159. <https://doi.org/10.1021/ic50001a031>.
- (21) Yu, Q.; Meng, X.; Wang, T.; Li, P.; Ye, J. Hematite Films Decorated with Nanostructured Ferric Oxyhydroxide as Photoanodes for Efficient and Stable Photoelectrochemical Water Splitting. *Adv. Funct. Mater.* **2015**, *25* (18), 2686–2692. <https://doi.org/https://doi.org/10.1002/adfm.201500383>.
- (22) Minguzzi, A.; Lugaresi, O.; Achilli, E.; Locatelli, C.; Vertova, A.; Ghigna, P.; Rondinini, S. Observing the Oxidation State Turnover in Heterogeneous Iridium-Based Water Oxidation Catalysts. *Chem. Sci.* **2014**, *5* (9), 3591–3597. <https://doi.org/10.1039/C4SC00975D>.
- (23) Zhang, Y.; Ouyang, B.; Xu, J.; Jia, G.; Chen, S.; Rawat, R. S.; Fan, H. J. Rapid Synthesis of Cobalt Nitride Nanowires: Highly Efficient and Low-Cost Catalysts for Oxygen Evolution. *Angew. Chemie Int. Ed.* **2016**, *55* (30), 8670–8674. <https://doi.org/https://doi.org/10.1002/anie.201604372>.
- (24) Lu, X.; Yim, W.-L.; Suryanto, B. H. R.; Zhao, C. Electrocatalytic Oxygen Evolution at Surface-Oxidized Multiwall Carbon Nanotubes. *J. Am. Chem. Soc.* **2015**, *137* (8), 2901–2907. <https://doi.org/10.1021/ja509879r>.
- (25) Sivula, K.; Le Formal, F.; Grätzel, M. Solar Water Splitting: Progress Using Hematite (α -Fe₂O₃) Photoelectrodes. *ChemSusChem* **2011**, *4* (4), 432–449. <https://doi.org/https://doi.org/10.1002/cssc.201000416>.

- (26) Yoon, K.-Y.; Ahn, H.-J.; Kwak, M.-J.; Kim, S.-I.; Park, J.; Jang, J.-H. A Selectively Decorated Ti-FeOOH Co-Catalyst for a Highly Efficient Porous Hematite-Based Water Splitting System. *J. Mater. Chem. A* **2016**, *4* (48), 18730–18736. <https://doi.org/10.1039/C6TA08273D>.

Chapter 3. Insight into the dopability of hematite photoanode for an efficient water splitting

*Chapter 3 is reproduced in part with permission of “Yoon, K.-Y.; Park, J.; Lee, H.; Seo, J. H.; Kwak, M.-J.; Lee, J. H.; and Jang, J.-H.”³⁰ Copyright © 2022 American Chemical Society

3.1. Introduction

In a follow-up study in chapter 2, the phenomenon of doping was observed more fundamentally since the SiO_x over layer can cause Si-doping while acting as a hard template. Basically, Si is one of the most representative dopants used in the hematite.¹⁻⁴ A fabrication method for Si doped hematite has been reported through atmospheric pressure chemical vapor deposition (APCVD) or ultrasonic spray pyrolysis (USP).⁵⁻⁷ Although these technologies have the characteristics of a non-equilibrium process, the Si doping from the SiO_x overlayer we use is a Si-doping method through the equilibrium process.^{8,9} Therefore, we need to confirm whether there is a difference in the doping between non-equilibrium and equilibrium processes. Because our previous study showed that the structure also changed with doping, it is necessary to know which factors have a greater effect on the efficiency improvement of porous hematite. Moreover, in theoretical calculations, it has been reported that Si is difficult to dope into hematite in the equilibrium process,⁷ but our porous hematite showed an excellent improvement in the PEC performance. Therefore, it is assumed that there should be a valuable phenomenon hidden in the manufacturing process of our porous hematite that we have not been able to discover. In Chapter 3, we intensively analyzed the phenomena that were not discovered in previous studies. Through various analyzes, it was confirmed that the Ti dopant, which was simply used to improve efficiency, enables Si doping in equilibrium process. By understanding the interaction between Si and Ti, we can further improve the efficiency of porous hematite. This study proposes a method to easily manufacture materials that could only be produced in non-equilibrium in the equilibrium state using the interaction of two dopants.

3.2. Experimental section

3.2.1 Fabrication of Si-Fe₂O₃ or Si:Ti-Fe₂O₃ electrodes.

Si doped or Si:Ti co-doped Fe₂O₃ was prepared by growing FeOOH or Ti-FeOOH with 150 mM FeCl₃ w/wo TiCl₃ precursor. For SiO_x coating, FeOOH or Ti-FeOOH electrode was immersed in APTMS solution for 30 min, and then washed with D.I. water and dried with N₂ gas. SiO_x coated FeOOH or Ti-FeOOH electrode are heat treated at 850 °C for 20 min to make Si-Fe₂O₃ or Si:Ti-Fe₂O₃ electrodes.

3.2.2 Fabrication of NiFeO_x coated Si:Ti-Fe₂O₃ electrodes.

To load the NiFeO_x OER co-catalyst Si:Ti-Fe₂O₃ photoanode, precursors, nickel(II) 2-ethylhexanoate (78% w/w in 2-ethylhexanoic acid) as Ni source and iron(III) 2-ethylhexanoate (50% w/w in mineral spirits) as iron source was mixed in hexane solution. After making stock solution by mixture, the dilution was conducted to 50 mM metal complex. The loading of NiFeO_x on Si:Ti-Fe₂O₃ was achieved by spin coating method and then, the electrode was exposed with UV light for 1h. Final step was that the electrode is annealed at 100 °C for 1h.

3.2.3 PEC measurements.

PEC measurements were carried out as half-cell measurements. The half-cell test was based on a three-electrode system made of an Ag/AgCl electrode by KCl saturated solution and a platinum mesh as reference and counter parts, respectively. The exposed area for measuring PEC efficiency was fixed at 0.44 cm² by O-ring. The electrolyte was applied as 1M NaOH (pH=13.6) in all PEC measurements. The scan rate is the same for all of them at 20 mVs⁻¹. EIS results were fitted using Z-view software for accurate analysis. IPCE measurement was conducted out by Xe lamp with monochromatic light.

3.2.4 DFT calculation details.

The first principle density functional theory calculations were executed in the spin-polarized framework along with the projector augmented wave (PAW) approach¹⁰ using the Vienna ab-initio simulation package (VASP).¹¹ The exchange-correlation functional was considered using the generalized gradient approximation (GGA) in Perdew, Burke, and Ernzerhof (PBE) parameterization. The cut-off energy for the planewave basis was set to 500 eV, and Monkhorst-Pack k-point mesh of 4 × 4 × 1 was used for

calculation of density of state of all the slab structure of α -Fe₂O₃ (hematite). All the ionic positions were relaxed *via* conjugate gradient method until atomic force convergence of 0.01 eV Å⁻¹ was achieved. In case of transition metal oxide systems 3d electronic states are strongly correlated, hence considering the same, we employed the spin polarized GGA + U formalism due to improper action of d-electrons with standard DFT.¹² The GGA + U calculations depends on the values of U-J and were set to 4.2 eV which are in accordance with the experimental band gap value of hematite (2.2 eV). The hexagonal unit cell of α -Fe₂O₃ was optimized with a layered antiferromagnetic (AFM) ordering. In case of pure α -Fe₂O₃ unit cell, the lattice parameters calculated within PBE + U and found to be a = b = 5.07 Å and c = 13.88 Å, and consistent with the experimental values of a = b = 5.04 Å and c = 13.75 Å.¹³

3.3. Results and discussion

To consider in-depth mechanism of Si doping, we observed any changes w/wo Ti dopant as shown in Figure 3.1a. In terms of structure, it was confirmed through SEM and TEM that almost similar porous structures were formed regardless of the presence or absence of Ti dopant as shown in Figures 3.1b and c. Through the SEM and TEM structures, we can prove that the structural change is formed through the SiO_x overlayer regardless of Ti dopant since both conditions confirmed that nonporous general hematite was formed w/wo Ti dopant as shown in Figure 3.2. In Chapter 2, we explained that the mechanism of the porous structure is due to evaporation of water, but additionally, we confirmed the Kirkendall effect by confirming the hematite manufacturing under various conditions by BET analysis as shown in Figure 3.3.¹⁴

Interesting results were found in the PEC system. It has been confirmed that porous hematite (denoted as $\text{Si-Fe}_2\text{O}_3$) with a porous structure without Ti has almost no photoactivity. This is clearly outside the predicted range since Si is one of the dopants commonly used in hematite with Ti dopant. as shown in Figure 3.1d, Ti doped Fe_2O_3 (denoted as $\text{Ti-Fe}_2\text{O}_3$) showed a photocurrent density of around 1.2 mA cm^{-2} , which is about 2 times higher than that of pristine hematite (denoted as Fe_2O_3). With the structural evolution, $\text{Si:Ti-Fe}_2\text{O}_3$ exhibited a photocurrent density of round 3.0 mA cm^{-2} . It has been proved that the great efficiency improvement of $\text{Si:Ti-Fe}_2\text{O}_3$ is due to the effects of both the porous structure and doping. However, $\text{Si-Fe}_2\text{O}_3$ prepared without Ti showed a very low PEC efficiency of 0.05 mA cm^{-2} despite having a similar porous structure. Although $\text{Si:Ti-Fe}_2\text{O}_3$ and $\text{Si-Fe}_2\text{O}_3$ have almost similar optical properties as shown in Figure 3.1e and Figure 3.4 as well as structural properties, the extreme difference in IPCE results is a very interesting result as shown in Figure 3.1f. Therefore, we hypothesized that Ti plays a specific role depending on the presence or absence of Ti, thereby contributing greatly to Si doping.

Structural differences were confirmed through density functional theory (DFT) calculation to confirm fundamental differences depending on the presence or absence of Ti as shown in Figures 3.5a and b. Hematite basically consists of octahedral structures, and it was confirmed that some octahedral structures change to tetrahedral structures when Si is doped. This may have contributed to the extremely low PEC efficiency of $\text{Si-Fe}_2\text{O}_3$. In $\text{Ti-Fe}_2\text{O}_3$, tetrahedral structure was not observed. Therefore, it could be predicted that the PEC performance was improved compared to pristine Fe_2O_3 in the LSV curves. Different from the observation of many structural collapses in $\text{Si-Fe}_2\text{O}_3$ containing Si without Ti, $\text{Si:Ti-Fe}_2\text{O}_3$ also did not form a tetrahedral structure. To find out the reason, we calculated the formation energy of 4 types of hematite. A high formation energy means that doping is difficult to do, and a high formation energy means that doping is easy on the contrary. As shown in Figure 3.5c, In the absence of

Ti, Si doping confirmed that the formation energy was much higher than that in the presence of Ti. Since we need a reference point for how well doping is done, we took this reference point as the formation energy for Sn doping. It has been reported that Sn doping is easily doped as it diffuses from the FTO.

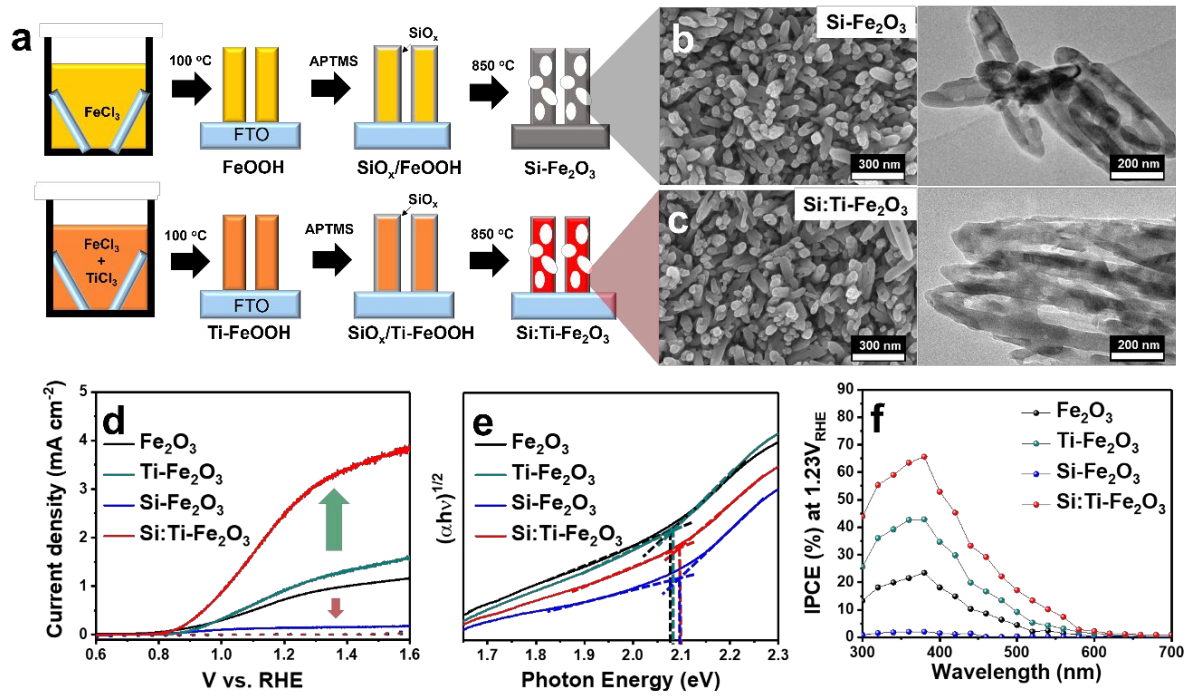


Figure 3.1. (a) Schematic images for two strategies for consideration of Si doping with and without Ti dopant. Comparison of SEM and TEM images for (b) Si doped hematite by SiO_x layer and (c) Si and Ti co-doped hematite by SiO_x layer. (d) Linear sweep voltammetry (LSV) curves with and without Ti dopant. LSV measurement was conducted in basic electrolyte (1 M NaOH solution). The LSV curves measured in the dark condition are indicated by dotted lines. (e) Comparison of tauc plots calculated from the UV-Vis spectra of four types of hematite. (f) Comparison of incident-photon-to-current efficiency (IPCE) spectra of Si doped hematite by SiO_x layer and Si and Ti co-doped hematite by SiO_x layer.

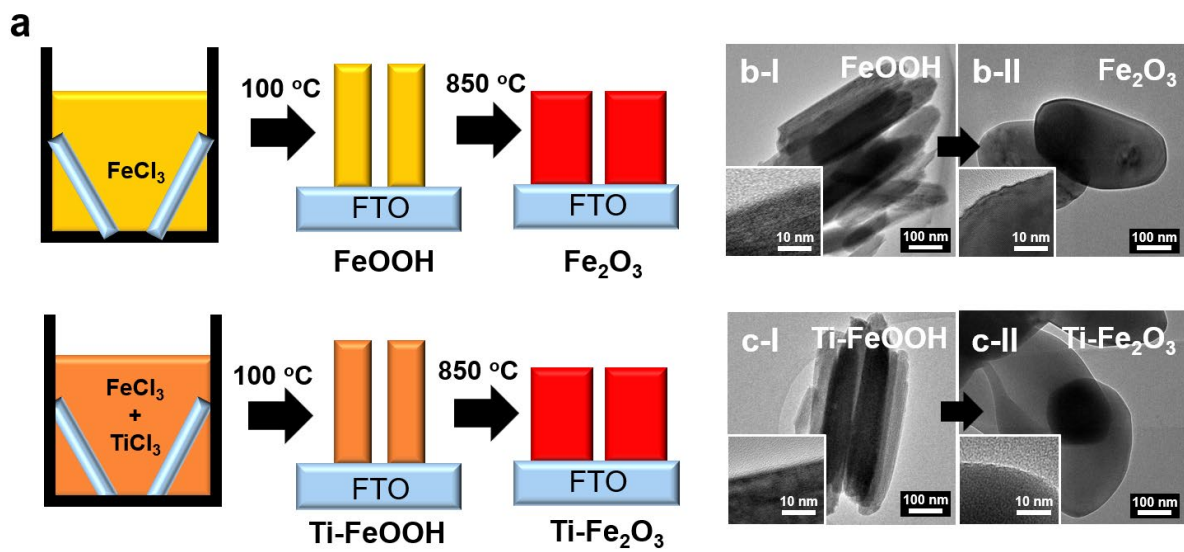


Figure 3.2. Scheme for photoanode fabrication of Fe_2O_3 and Ti doped Fe_2O_3 . TEM images of (b-I) FeOOH , (b-II) Fe_2O_3 , (c-I) Ti doped FeOOH and (c-II) $\text{Ti-Fe}_2\text{O}_3$.

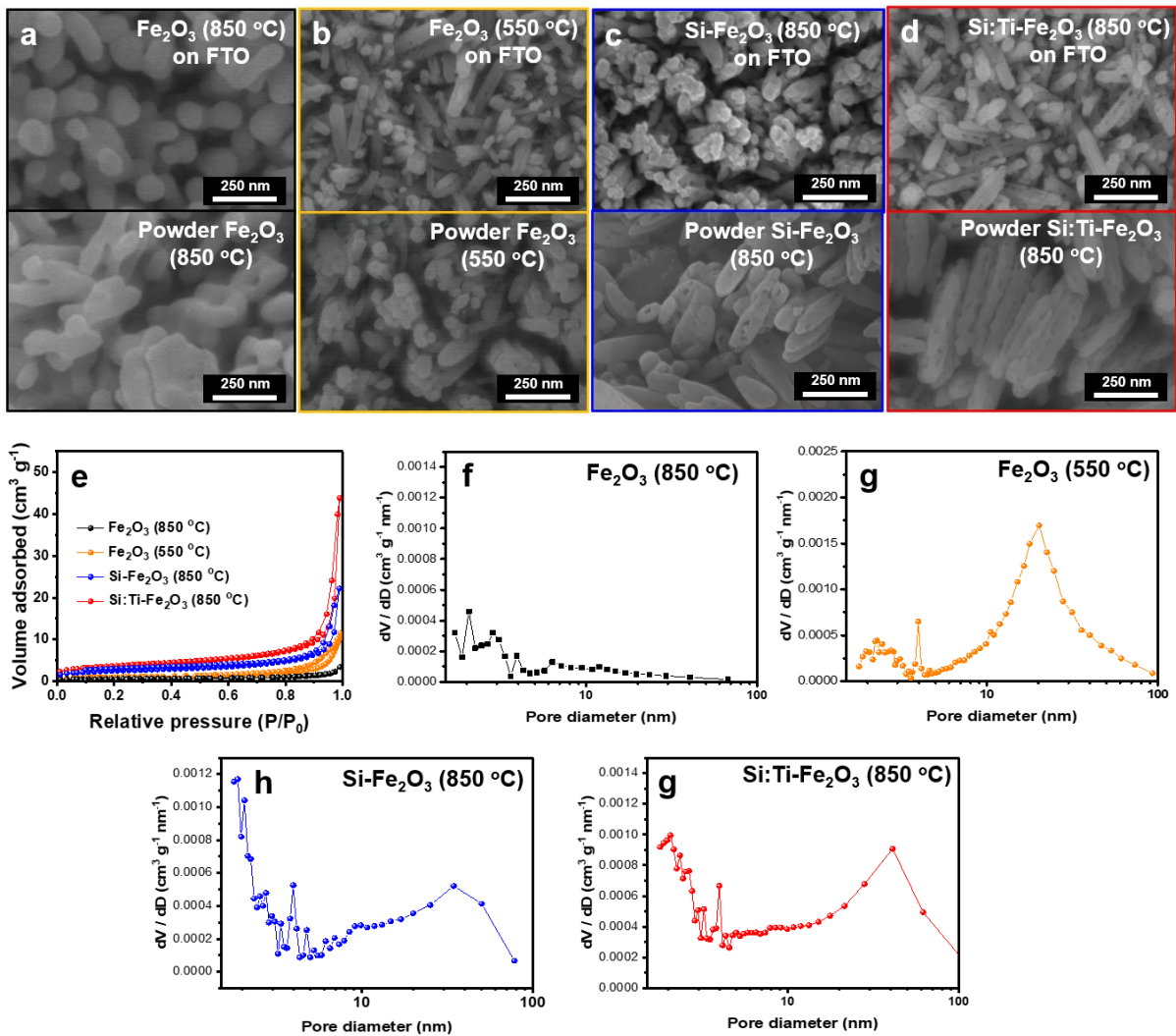


Figure 3.3. Comparison of Fe_2O_3 annealed at 850 °C and 550 °C, and Si- Fe_2O_3 and Si and Ti doped Fe_2O_3 annealed at 850 °C. SEM images of (a) Fe_2O_3 annealed at 850 °C, (b) Fe_2O_3 annealed at 550 °C and (c) Si doped Fe_2O_3 (d) Si and Ti doped Fe_2O_3 annealed at 850 °C. The upper image is hematite grown on FTO and the lower image is the powder hematite. (e) N_2 adsorption-desorption isotherms of four kinds of Fe_2O_3 . The BET surface area of each Fe_2O_3 is $2 \text{ m}^2/\text{g}$ (Fe_2O_3 , 850 °C), $5 \text{ m}^2/\text{g}$ (Fe_2O_3 , 550 °C), $9 \text{ m}^2/\text{g}$ (Si doped Fe_2O_3 , 850 °C) and $12 \text{ m}^2/\text{g}$ (Si and Ti co-doped Fe_2O_3 , 850 °C). The pore distribution of (f) Fe_2O_3 (850 °C), (g) Fe_2O_3 (550 °C), (h) Si doped Fe_2O_3 (850 °C) and (g) Si and Ti co-doped Fe_2O_3 (850 °C).

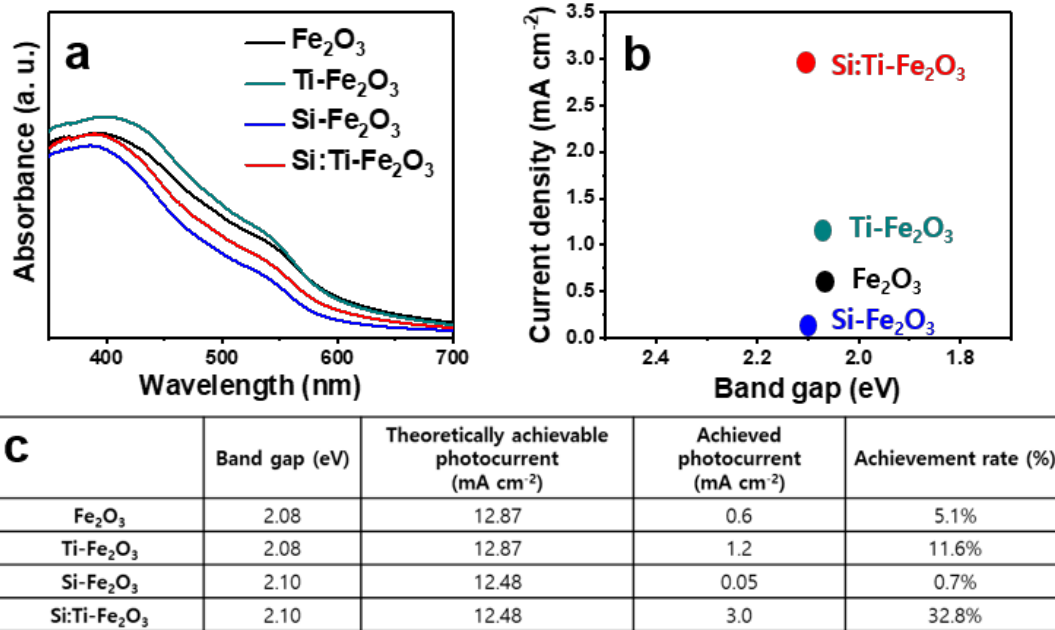


Figure 3.4. Comparison of (a) UV-Vis spectra and (b) Achieved photocurrent density with band gap. (c) Comparison of the achieved photocurrent density with the theoretically achievable values based on band gap to utilize theoretical photocurrent density by Shockley and Queisser.

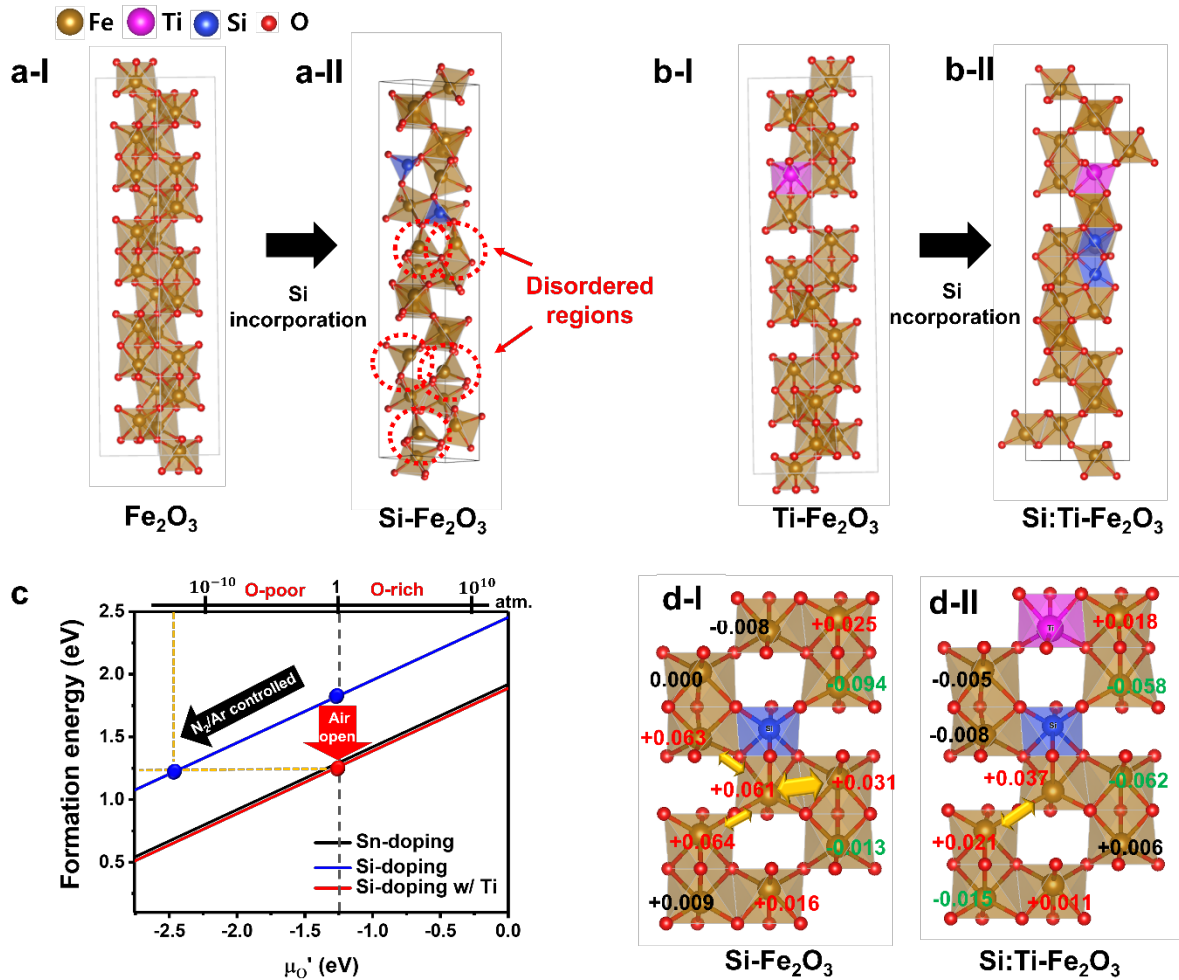


Figure 3.5. (a) Atomic arrangements for (a-I) Fe_2O_3 and (a-II) Si doped Fe_2O_3 without Ti dopant. (b) Atomic arrangements for (b-I) Ti doped Fe_2O_3 and (b-II) Si and Ti co-doped Fe_2O_3 . (c) Comparison of formation energy for effect of Ti dopant on Si doping with representative Sn doping into hematite. The black dotted line is the formation energy values at 1100k temperature and 1 atmosphere closest to the experimental condition. (d) Comparison of crystal-orbital overlap population (COOP) for the Fe atoms in (d-I) Si doped hematite and (d-II) Si and Ti co-doped hematite. Yellow arrows indicate charge repulsion between Fe atoms.

It can be seen that the formation energy for Si doping with Ti dopant is smaller than that of Sn doping, indicating that Si doping can be well achieved with the presence of Ti. Conversely, it can be seen that the formation energy for Si doping alone without Ti forms much higher values than that of Sn doping. This means that Si doping is difficult to do without Ti dopant. Therefore, we can reveal the correlation between Si doping method and formation energy reported so far through this. So far, Si doping has been successfully achieved through non-equilibrium processes such as APCVD and UPS. The best we found that there is no report so far that Si can be doped in equilibrium. Obviously, various attempts have been made, but it is expected that the Si doping was not successful through the equilibrium process because of the high formation energy of Si doping. However, the presence of Ti can lower the barrier of high formation energy, confirming that doping is possible with our equilibrium process. If it can be manufactured with the equilibrium process, it will be possible to have a more competitive edge than nonequilibrium process in terms of increasing the electrode area and manufacturing cost of the electrode. There are two main reasons why Ti can rapidly decrease the formation energy for Si doping. First, the size balance of the three ions ($\text{Si}^{4+} < \text{Fe}^{3+} < \text{Ti}^{4+}$) fits well. The excellent balance of the three ions has already been verified in previous studies,⁵ but the efficiency of Si single doping also improved because the electrodes were manufactured in non-equilibrium in previous studies. However, we have confirmed that it is possible to verify this more reasonably in the equilibrium process. The second is the charge balance of Fe ions. We calculated the Crystal-orbital overlap population (COOP) for the Fe atom as shown in Figure 3.5d. In Si-Fe₂O₃, it has been confirmed that the charge balance between Fe atoms is not matched by Si dopant, and a strong repulsive force was formed between nearby Fe atoms. This is the main reason why the structure of hematite changes to tetrahedral when only Si is doped. The COOP result when Si exists together with Ti confirmed that the repulsive force of Fe atoms is relaxed. Since Si has the property to form a strong Si-O bond and maintains the tetrahedral structure,¹⁵ when only Si is doped, it strongly induces a change in the surrounding charge, but it was confirmed that Ti can alleviate the charge repulsion. In addition, since our electrode manufacturing process can be doped with Sn, the effect on Sn needs to be considered.¹⁶⁻¹⁸ In this process, we found that Sn doping was drastically suppressed when porous hematite was manufactured using the SiO_x overlayer. Sn doping proceeds with deformation of FTO as FTO slightly melts at high temperature. This is because SiO_x acts as a hard template to prevent hematite from melting and coarsening. Therefore, the area where Sn is diffused is also reduced as shown in Figure 3.6. However, since Sn doping is not completely blocked, we also checked the effect of Sn on Si doping through the formation energy as shown in Figure 3.7. The results revealed that Sn can also play a role in lowering the formation energy for Si doping. However, in this study, since the concentration of Sn on the surface is below 1%, it is assumed that almost no Sn has reached the surface, and the influence of Sn is excluded.

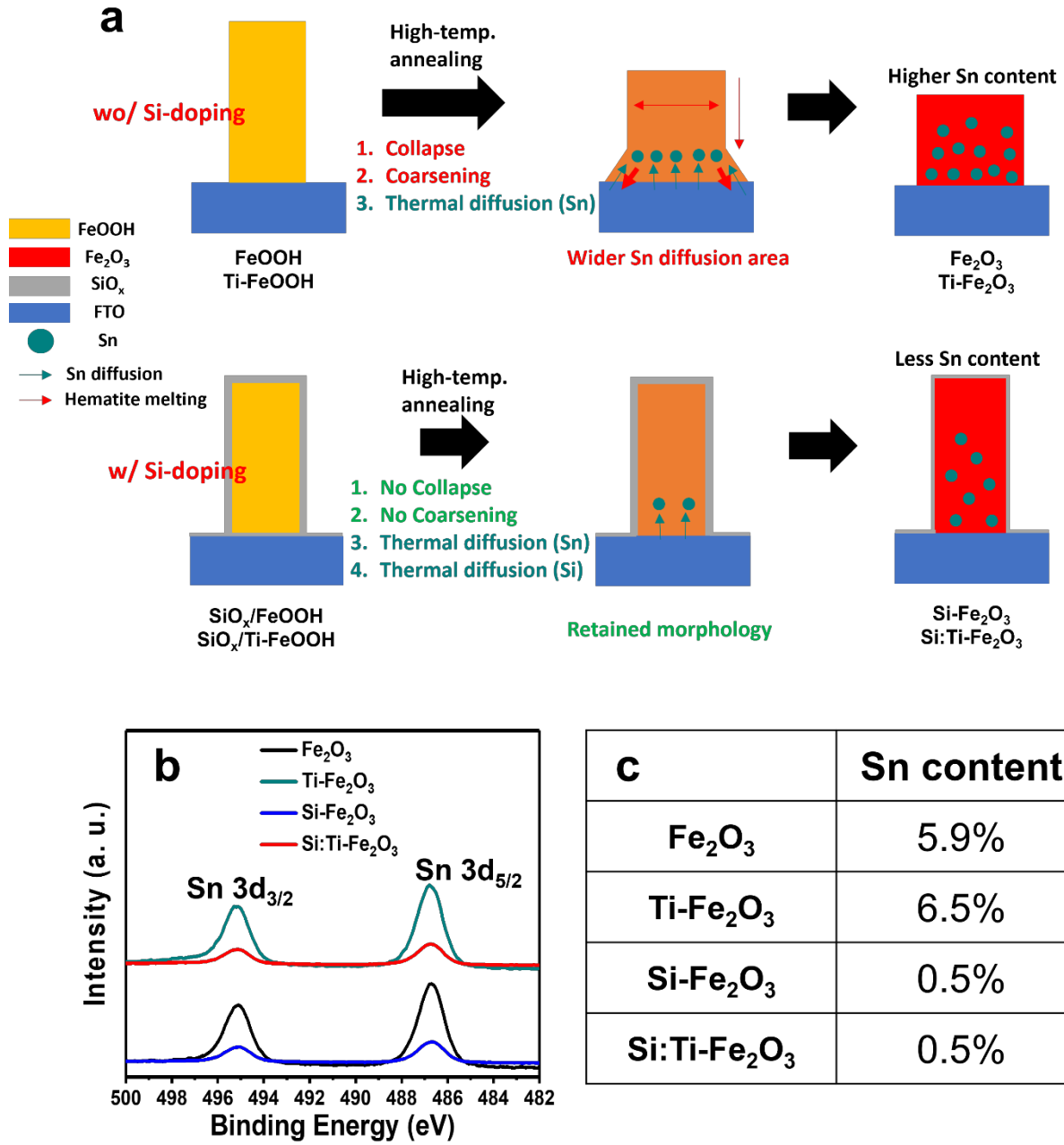


Figure 3.6. (a) Schematic images of the Sn distribution during hematite fabrication process w/w/o the SiO_x layer. (b) The comparison of XPS spectra of Sn 3d and (c) Sn content.

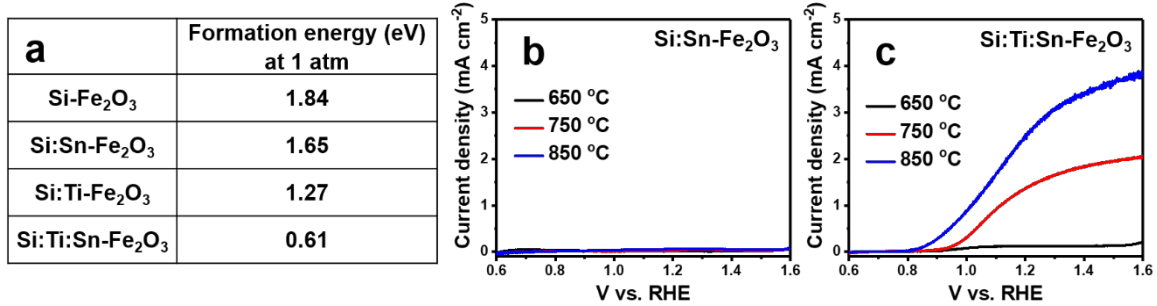


Figure 3.7. The formation energy of Fe₂O₃ for Si doping in a 2 x 2 x 1 supercell. The PEC activity of Si-doped Fe₂O₃ w/wo Ti-dopant by considering the interaction of the Sn dopant with the other two dopants (Si or Ti) by controlling the annealing temperature: (b) Si and Sn co-doped Fe₂O₃ and (c) Si, Ti, and Sn co-doped Fe₂O₃.

Photoanode	Current density at 1.23V _{RHE}	Process for Si doping (Requirement)	Si content	Reference
Si-Fe ₂ O ₃	~0.2 mA cm ⁻²	Reactive ballistic deposition (RBD, nonequilibrium process)	~5%	19
Si-Fe ₂ O ₃	~1.9 mA cm ⁻²	Atmospheric-pressure chemical vapor deposition (APCVD, nonequilibrium process)	~4.4%	5
Si-Fe ₂ O ₃	~2.3 mA cm ⁻²	Atmospheric-pressure chemical vapor deposition (APCVD, nonequilibrium process)	~1.6%	20
Si:Ti-Fe ₂ O ₃	~0.8 mA cm ⁻² (~2.2 mA cm ⁻² at 1.6 V _{RHE})	Ultrasonic spray pyrolysis (USP, nonequilibrium process)	~4%	6
Si-Fe ₂ O ₃ Co/Si-Fe ₂ O ₃	~2.2 mA cm ⁻² ~2.7 mA cm ⁻²	Atmospheric-pressure chemical vapor deposition (APCVD, nonequilibrium process)	~1.5%	21
Si:Ti-Fe ₂ O ₃	~0.8 mA cm ⁻²	Spin coating & thermal diffusion (Equilibrium process)	~0.7%	22
Si:Ti-Fe₂O₃ NiFeO_x/Si:Ti-Fe₂O₃	3.0 mA cm⁻² 4.3 mA cm⁻²	Dip coating & thermal diffusion (Equilibrium process)	~6.2%	This study

Table 3.1. Comparison of the PEC performance and Si content.

Based on the results of DFT calculation, we focused on the crystallinity of hematite through various analyses. First, 3D-TOF-SIMS analysis was performed to confirm that Si diffuses into hematite through the overlayer during high temperature annealing. As shown in Figure 3.8a, it can be seen that the Si element is intensively distributed only on the surface before annealing process. After heat treatment, it was confirmed that Si was uniformly distributed throughout the cell. It means that Si diffused into hematite during the heat treatment process. The TOF-SIMS depth profile also showed that Si element presented a more uniform distribution after heat treatment as shown in Figure 3.8b. TEM images showed that when APTMS treatment was performed on FeOOH or Ti-FeOOH, which are precursors of hematite, an amorphous SiO_x layer of about 3-5 nm was coated as shown in Figures 3.8c and d. After heat treatment, Si:Ti-Fe₂O₃ formed a porous structure and showed that the amorphous layer on the surface became thinner than that of the surface of SiO_x/Ti-FeOOH. This means that the SiO_x of the amorphous layer becomes thinner as it diffuses into hematite. In the case of Si-Fe₂O₃, however, the amorphous layer became thicker than that of the surface of SiO_x/FeOOH. This is because the thickened amorphous layer destroyed the crystal structure of hematite as SiO_x diffused into hematite. That is, the thickened amorphous layer is a mixture of SiO_x and amorphous hematite. To verify this more clearly, The SiO_x layer was removed with HF.²³ After removing the SiO_x layer, Si:Ti-Fe₂O₃ showed only a very thin amorphous layer of less than 1 nm, while Si-Fe₂O₃ still formed a thick amorphous layer as shown in Figures 3.8e and f. Therefore, the diffusion of Si for Si doping during the annealing process can greatly affect the hematite crystal structure. The doping level of Si was measured through Si:Ti-Fe₂O₃ which SiO_x was removed. In the case of Si:Ti-Fe₂O₃ without removing the SiO_x layer, the doping level cannot be accurately measured by the SiO_x layer on the surface. The doping level of Si was confirmed to be about 6.2%, which is higher than the electrodes doped with Si by the conventional nonequilibrium process. Doping can improve electrical conductivity and increase carrier density, but it can also reduce crystallinity. Therefore, it requires an optimized condition for maximum efficiency. Although we doped Si dopant through the equilibrium process, we showed a high Si doping level, which means that the method of Si doping through the interaction of Ti and Si can doping more efficiently than the conventional nonequilibrium process as shown in Table 3.1. To directly compare the differences in crystallinity, XRD analysis was performed as shown in Figure 3.8g. In the XRD patterns, it could not be confirmed that the phase change was made to any materials other than hematite during the Si diffusion process. As a result of calculating the lattice parameter through the XRD pattern, it was shown that the lattice parameter of all electrodes had almost the same value as shown in Figure 3.10. This is probably because lattice parameter calculation through XRD is a more suitable analytical method for nanofilm rather than our hundreds of nanometers bulk material analysis. Instead, we confirmed the uniform distribution of Si and Ti through STEM-EDX as shown in Figure 3.11.

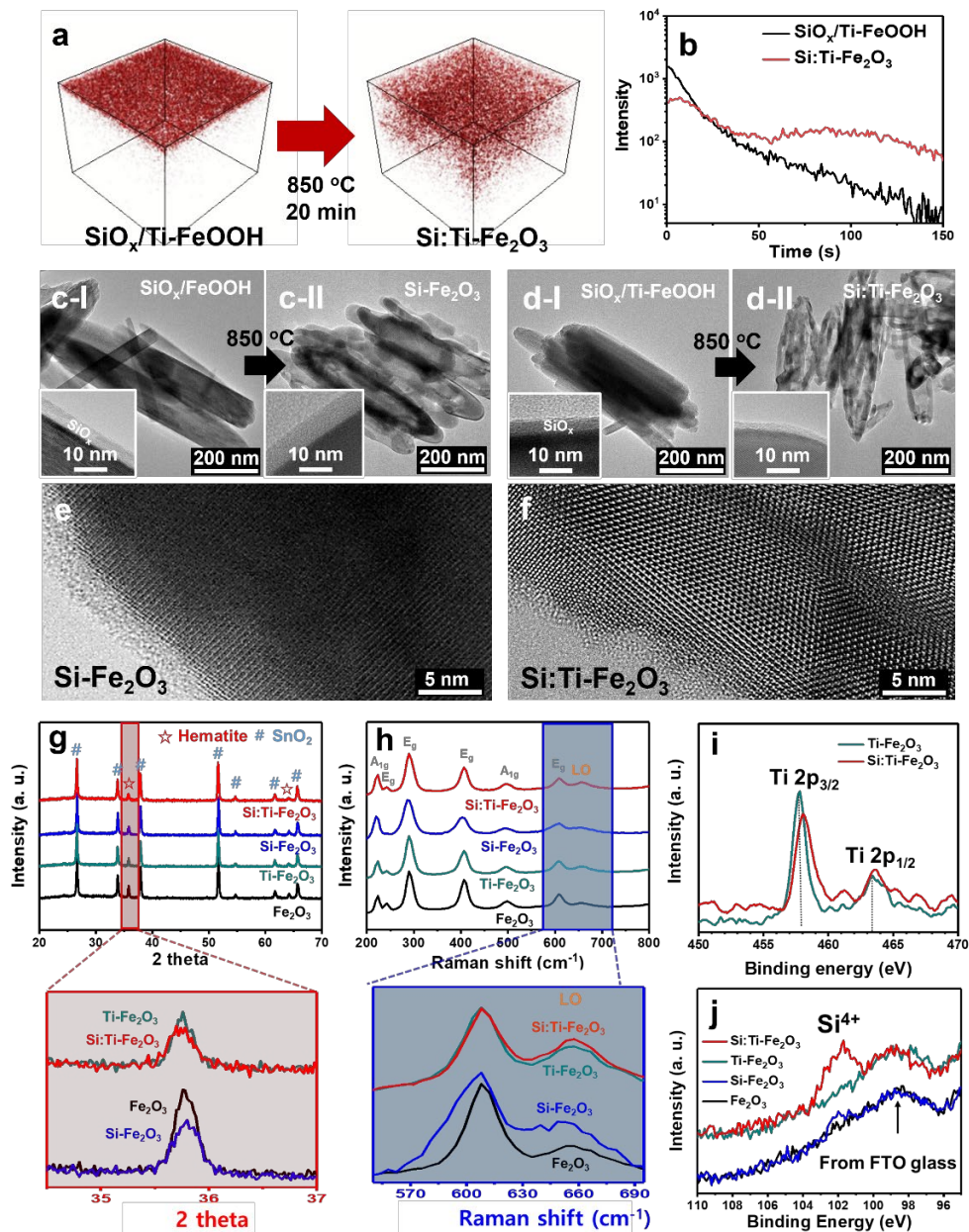


Figure 3.8. (a) Si distribution diagram by three-dimensional TOF-SIMS of (SiO_x coated Ti-FeOOH film) and after high temperature annealing process (Si and Ti co-doped Fe_2O_3 film) and (b) comparison of Si distribution by depth profiles of TOF-SIMS. TEM images of (c-I) SiO_x coated FeOOH, (c-II) Si doped Fe_2O_3 , (d-I) SiO_x coated Ti-FeOOH, and (d-II) Si and Ti co-doped Fe_2O_3 . High resolution TEM images of (e) Si doped Fe_2O_3 and (f) Si and Ti co-doped Fe_2O_3 by removing SiO_x layer. (g) XRD patterns of Fe_2O_3 , Ti doped Fe_2O_3 , Si doped Fe_2O_3 , and Si and Ti co-doped Fe_2O_3 . The Inset images are compared results by normalizing. (h) Raman spectra of Fe_2O_3 , Ti doped Fe_2O_3 , Si doped Fe_2O_3 , and Si and Ti co-doped Fe_2O_3 . The Inset images are compared results by normalizing. Comparison of XPS spectra for (i) Ti 2p for Ti effect and (j) Si 2p for the Si doping.

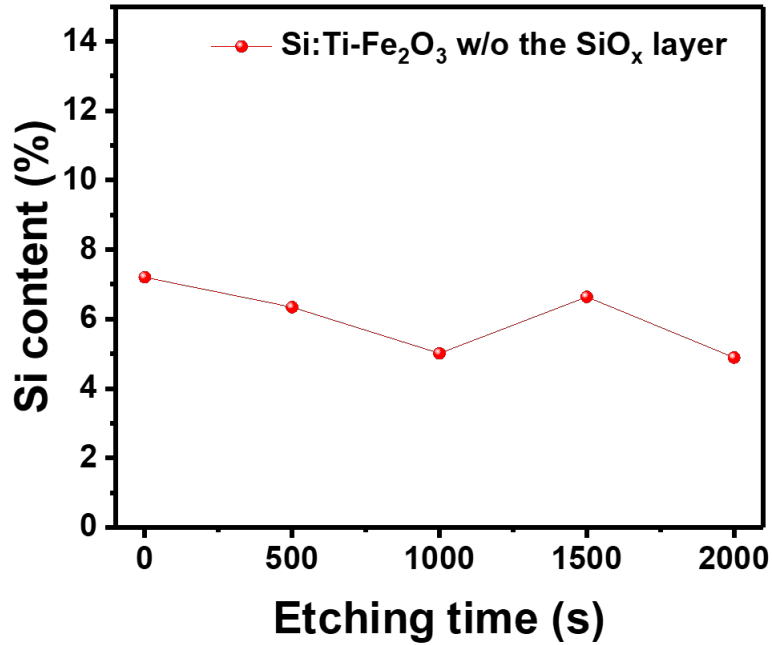


Figure 3.9. The XPS depth profiles of Si and Ti co-doped Fe_2O_3 without the SiO_x layer for Si content.

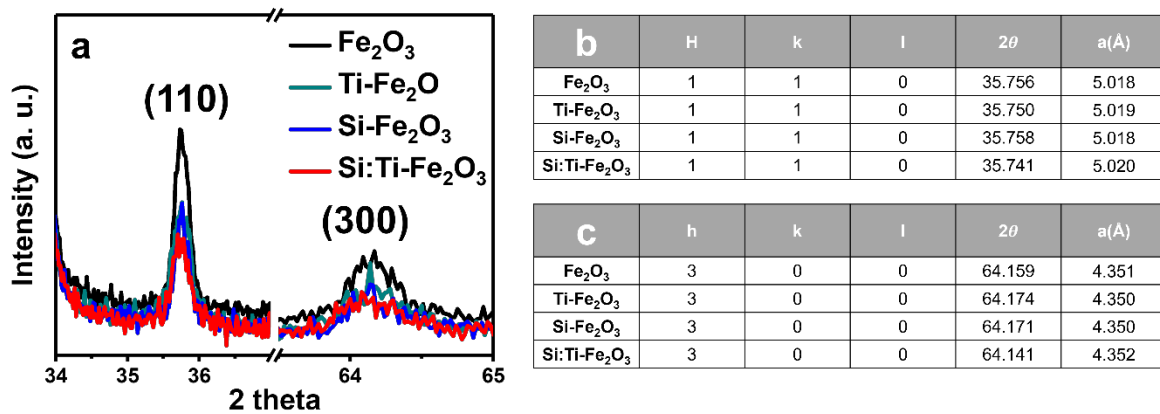


Figure 3.10. (a) Zoomed-in XRD patterns of Fe_2O_3 , Ti doped Fe_2O_3 , Si doped Fe_2O_3 , and Si and Ti co-doped Fe_2O_3 and (b) Lattice parameter calculated from XRD patterns.

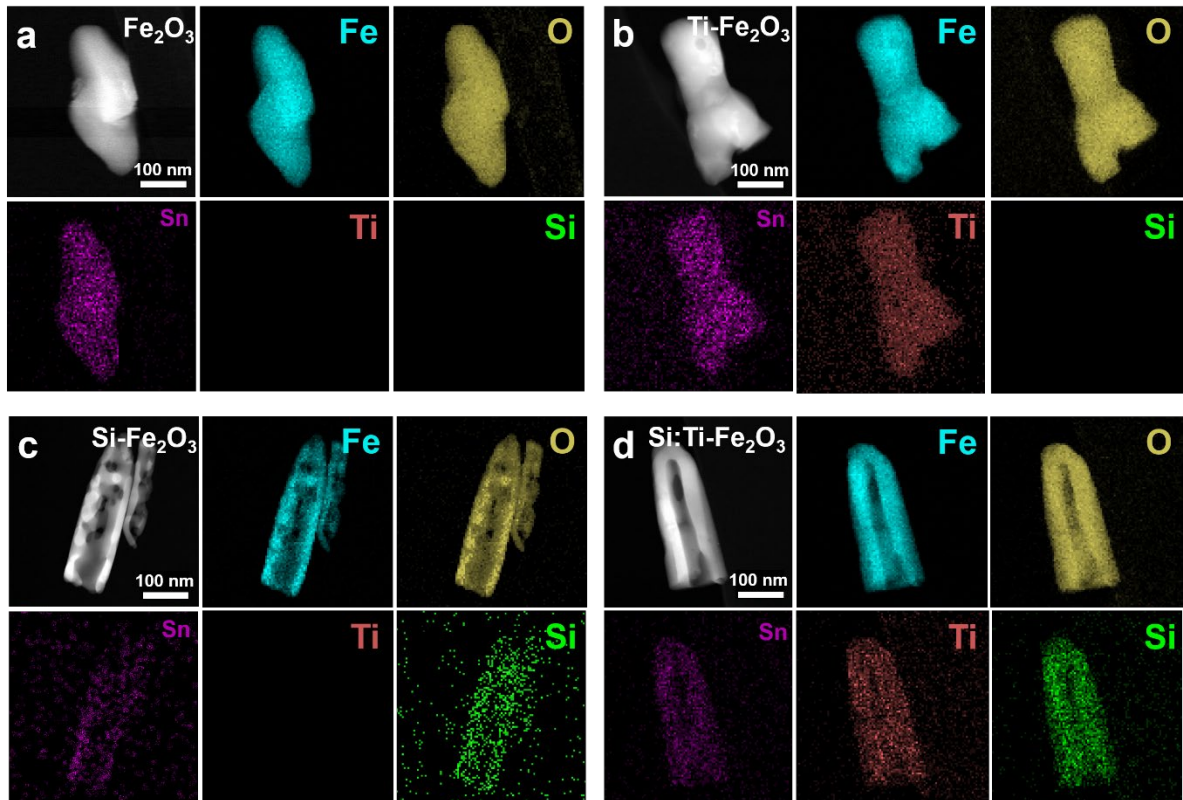


Figure 3.11. STEM-EDX elemental distribution of (a) Fe_2O_3 , (b) Ti doped Fe_2O_3 , (c) Si doped Fe_2O_3 and (d) Si and Ti co-doped Fe_2O_3 .

The (110) plane at 35.8° is known as the plane with the highest electrical conductivity among various crystal planes of hematite.²⁴ Si-Fe₂O₃ showed that the crystallinity of the (110) plane decreased by 15% compared to Fe₂O₃, whereas Si:Ti-Fe₂O₃ showed that the crystallinity of the 110 plane decreased by 5% compared to Ti-Fe₂O₃. Raman spectra is also available for crystallinity analysis. LO peak at 660 cm⁻¹ is a signal indicating the degree of disorder. It can be seen that Si-Fe₂O₃ has the widest and largest LO signal as shown in Figure 3.8h.²⁵ Therefore, Si-Fe₂O₃ has the lowest crystallinity through TEM, XRD, and Raman spectra, since it is difficult to properly do Si single doping in the equilibrium process. The role of Ti can be confirmed through the XPS measurement of Ti 2p. It was shown that the Ti 2p binding energy of Si:Ti-Fe₂O₃ is slightly higher than that of Ti-Fe₂O₃. This is because the Si-O bond, which is trying to form strongly, relaxes the characteristics of Si, which tries to form a strong tetrahedral structure by drawing electrons to Ti as shown in Figure 3.8i. The most convincing evidence for Si doping was found in the XPS spectrum of Si 2p as shown in Figure 3.8j. In order to check whether there is any clear Si⁴⁺ doping, XPS measurement was performed with the SiO_x overlayer removed because the Si⁴⁺ signal appearing in the SiO_x overlayer overlaps the doped Si⁴⁺ signal as shown in Figure 3.12. In Si:Ti-Fe₂O₃, the most distinct signal appeared at a binding energy of about 102 eV, known as the Si⁴⁺ doping signal in hematite. Although Si-Fe₂O₃ also showed weak Si⁴⁺ signals, it can be expected that the deteriorated charge transfer became more important as the hematite surface became amorphous. Following material analysis, photoelectrochemical analysis was also conducted. Through PEIS analysis, the behavior between the surface of hematite and the electrolyte was analyzed as shown in Figure 3.13a.^{26,27} We applied the equivalent circuit models to fit the achieved results in Figures 3.14–3.16 for the density of surface states (DOSS). Si:Ti-Fe₂O₃ formed the highest DOSS values in the entire measured range, whereas Si-Fe₂O₃ showed the lowest DOSS values. The Mott–Schottky plot also formed the lowest slope for Si:Ti-Fe₂O₃ and the highest slope for Si-Fe₂O₃, indicating that Si-Fe₂O₃ is hardly doped with Si, meaning that the crystal structure is the lowest compared to other electrodes as shown in Figure 3.13b. Since the Mott–Schottky plot is a measurement suitable for the film model, only indirect analysis is possible in our sample.²⁸ However, Assuming that Si-Fe₂O₃ and Si:Ti-Fe₂O₃ have almost similar structures, it is reasonable to check doping or not. For a more direct comparison, we measured the conductivity of the electrode through the FET as shown in Figure 3.17. Si:Ti-Fe₂O₃ showed the highest electrical conductivity, and Si-Fe₂O₃ showed the lowest electrical conductivity. The charge transfer efficiency was confirmed by converting the PEIS analysis result. At 1.3V vs. RHE, it was confirmed that the charge transfer efficiencies of Si:Ti-Fe₂O₃ (around 90%) and Si-Fe₂O₃ (around 2%) differed significantly by about 45 times as shown in Figure 3.13c. The charge separation efficiencies were also calculated by with or without a hole scavenger, as shown in Figure 3.13d and Figure 3.18. The charge separation efficiencies were shown with the same outcome trend as the transfer efficiency trend.

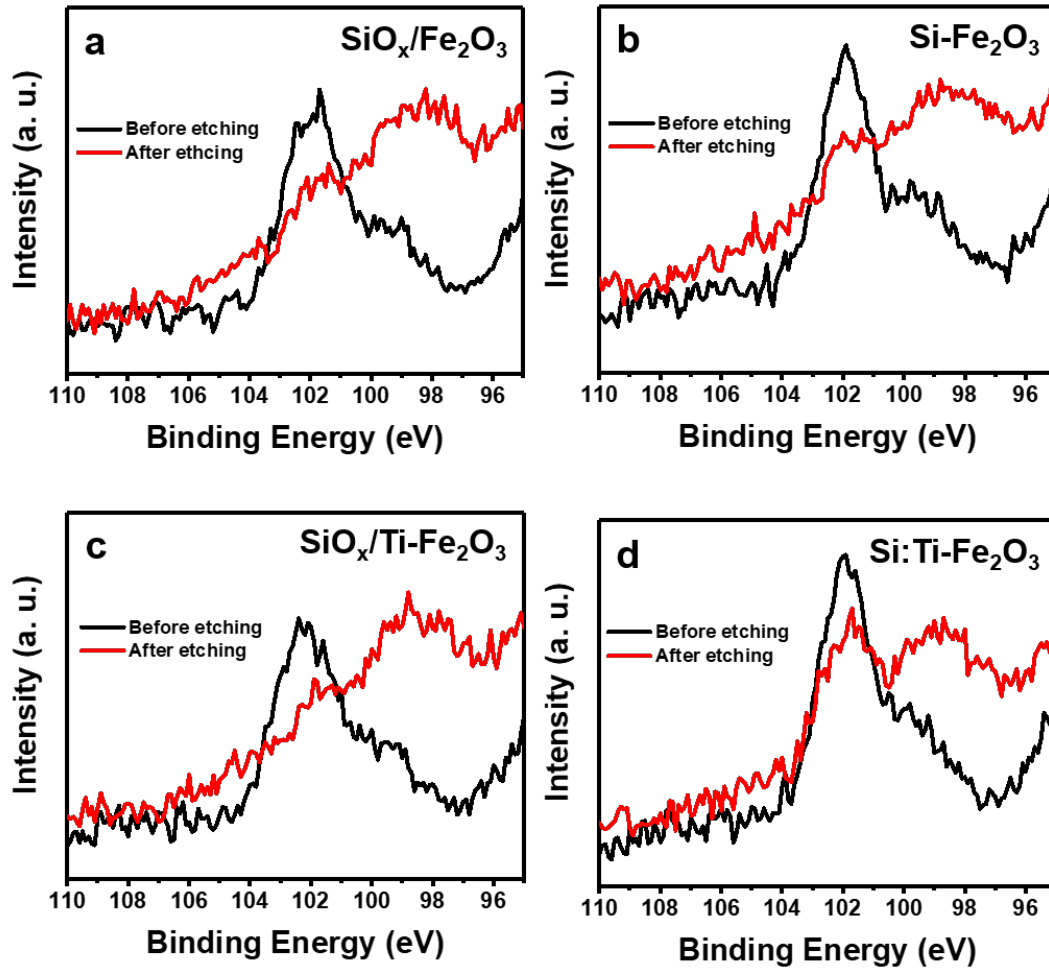


Figure 3.12. XPS spectra of Si 2p of (a) SiO_x coated Fe_2O_3 , (b) Si doped Fe_2O_3 , (c) SiO_x coated Ti- Fe_2O_3 and (d) Si and Ti doped Fe_2O_3 before and after etching the SiO_x layer.

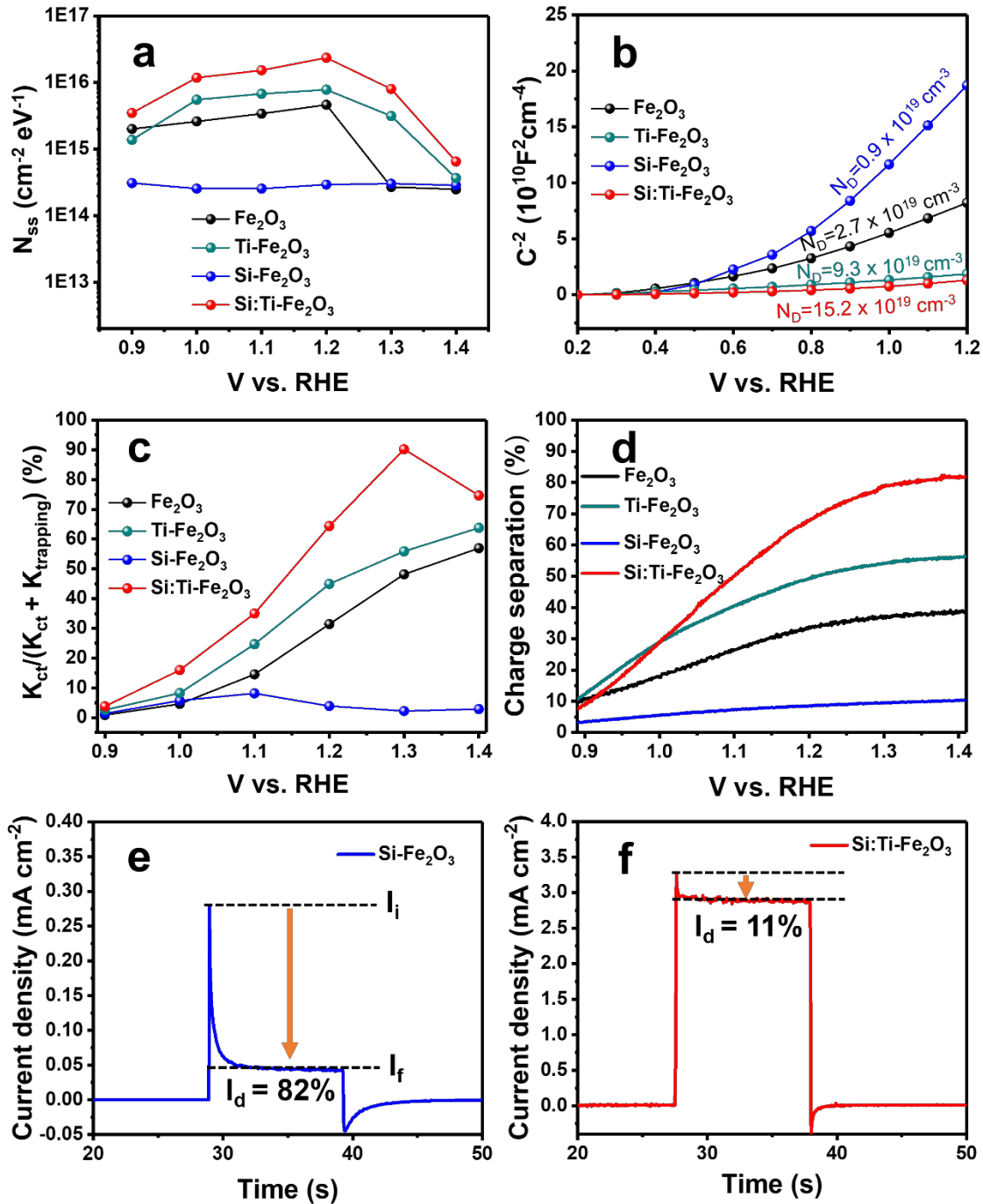


Figure 3.13. (a) Density of surface states (DOSS) by PEIS measurements in different applied potential range. (b) Mott-Schottky plots for charge density of each sample. (c) Charge transfer efficiency by calculating PEIS results. (d) Charge separation efficiency by hole scavenger system. Transient photocurrent behavior with (e) Si doped Fe_2O_3 and (f) Si and Ti co-doped Fe_2O_3 at 1.23 V_{RHE}.

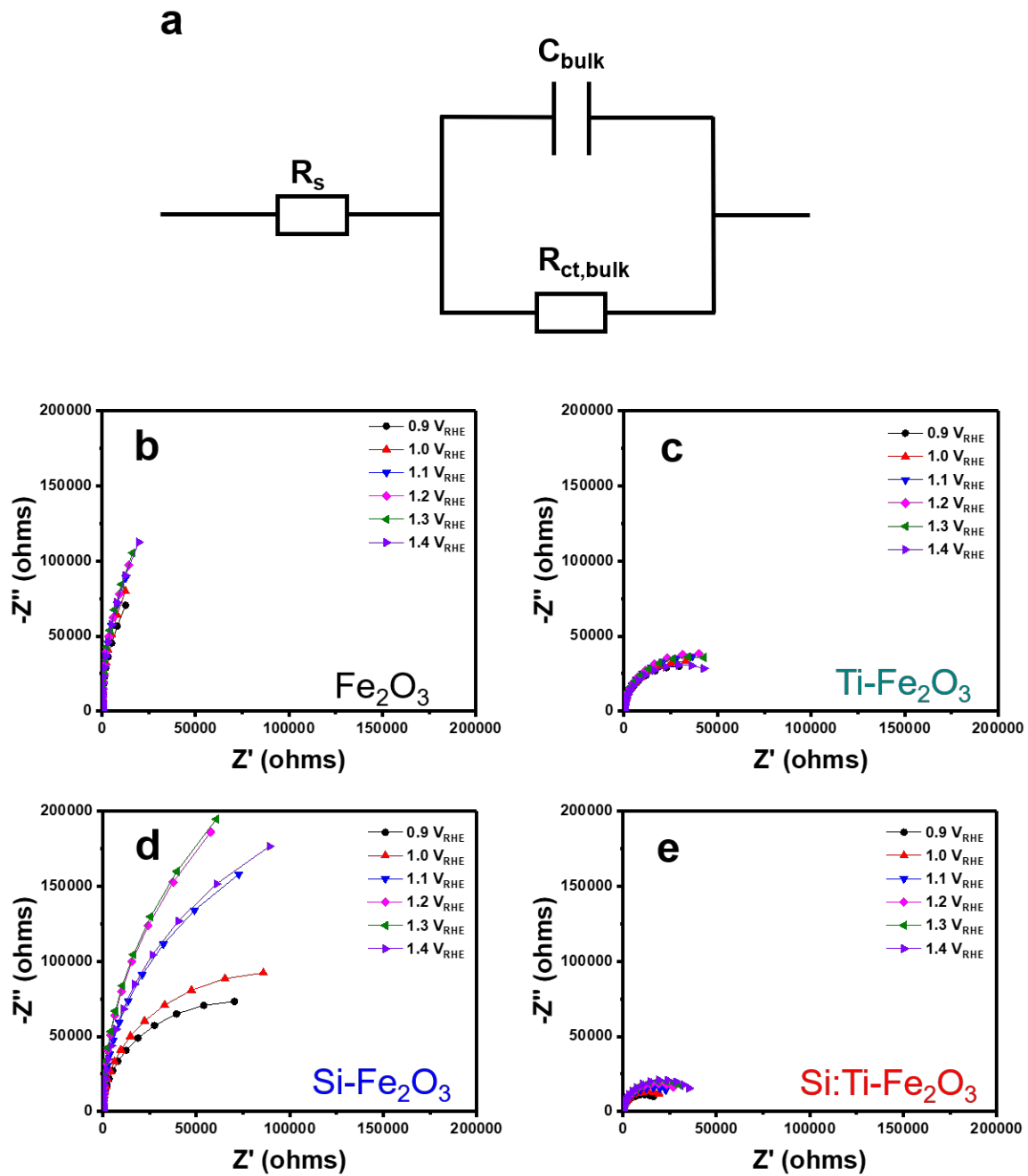


Figure 3.14. (a) The EIS circuit of hematite photoanodes under dark conditions. The comparison of Nyquist plots of (b) Fe_2O_3 , (c) Ti doped Fe_2O_3 , (d) Si doped Fe_2O_3 and (e) Si and Ti co-doped Fe_2O_3 .

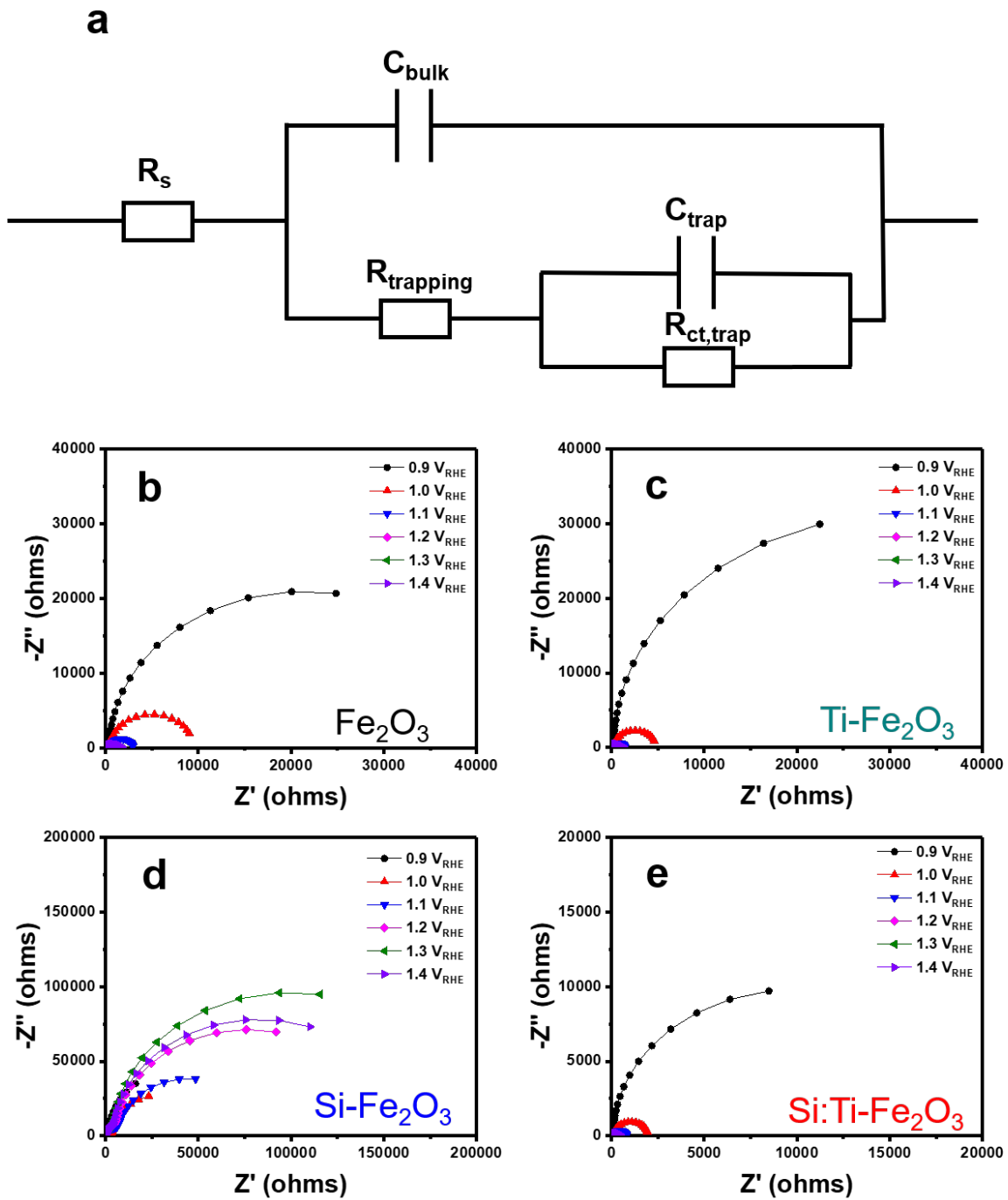


Figure 3.15. (a) The PEIS circuit of hematite photoanodes under light illumination. The comparison of Nyquist plots of (b) Fe_2O_3 , (c) Ti doped Fe_2O_3 , (d) Si doped Fe_2O_3 and (e) Si and Ti co-doped Fe_2O_3 .

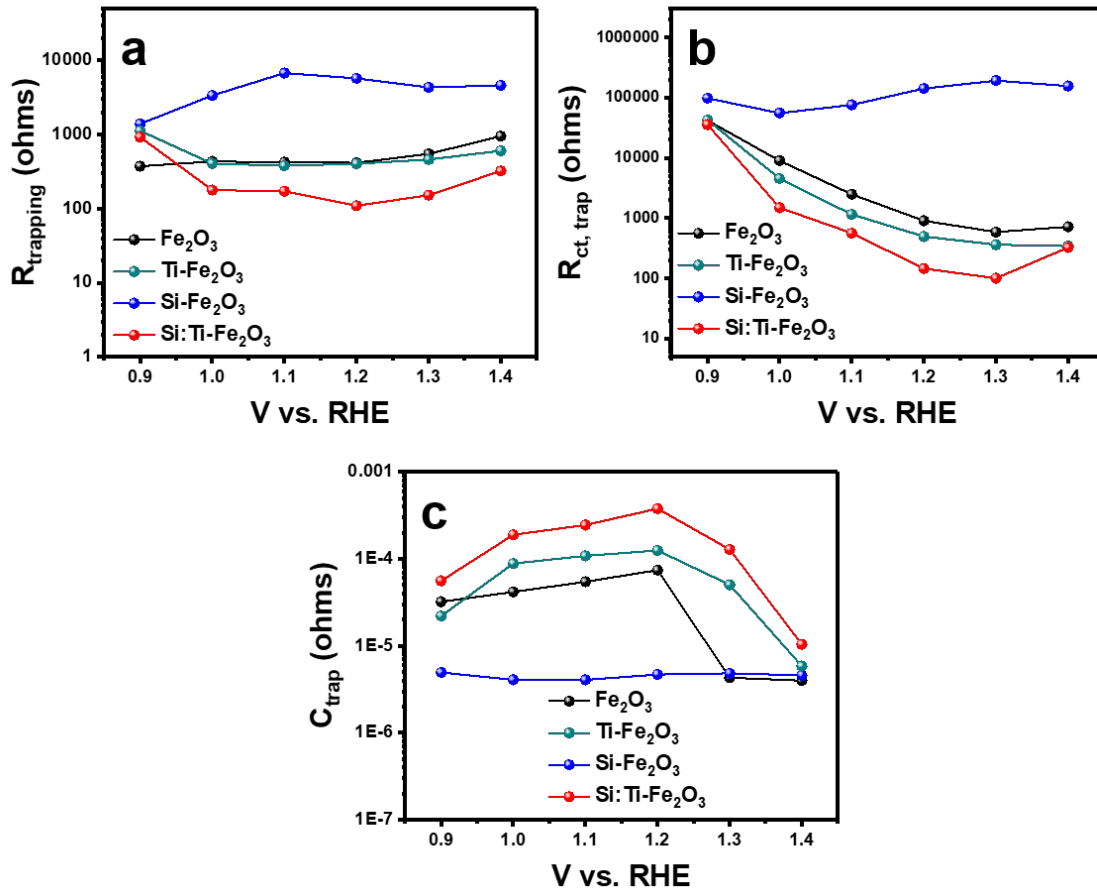


Figure 3.16. The PEIS circuit parameters by fitting PEIS data for Fe₂O₃, Ti doped Fe₂O₃, Si doped Fe₂O₃ and Si and Ti co-doped Fe₂O₃ in 1 M NaOH electrolyte under light condition. (a) R_{trappings}, (b) R_{ct,trap} and (c) C_{trap} in different applied potential.

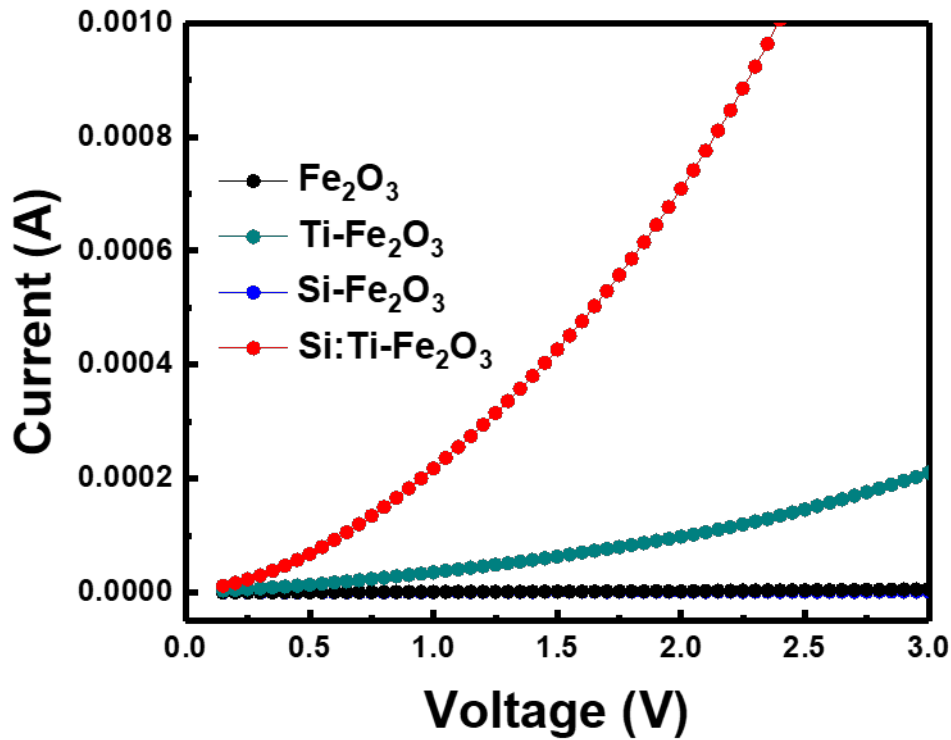


Figure 3.17. The comparison of the electrical conductivity for all samples.

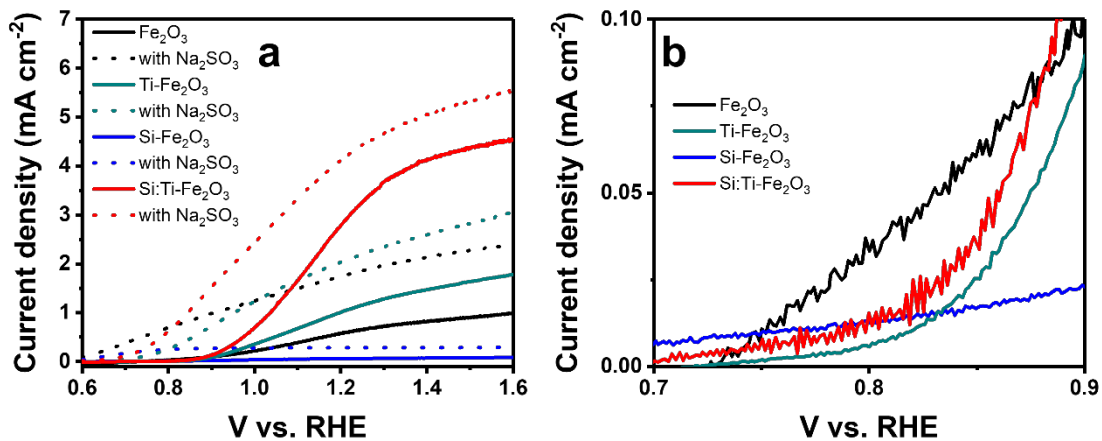


Figure 3.18. (a) LSV curves in a 1 M NaOH electrolyte (solid lines) and a 1M NaOH with 0.1 M Na₂SO₃ (dashed lines) electrolyte under light conditions. (b) The comparison of the current densities at below 0.9V_{RHE}

Transient photocurrent density measurement can analyze how adversely the charge transfer is affected when the crystals on the surface are amorphous as shown in Figures 3.13e and f. The photocurrent decay of Si-Fe₂O₃ showed a very high value of about 82%. This means that most of the electrons and holes generated by the light were reused for recombination. On the other hand, the photocurrent decay of Si:Ti-Fe₂O₃ was about 11%, which was relatively low compared to Si-Fe₂O₃. In the photoelectrochemical behavior analysis, it was confirmed that the charge transfer of Si-Fe₂O₃ was very disadvantageous due to the amorphous layer formed by Si diffusion. Through DFT calculations and intensive analysis of crystallinity, we understood the interaction between Si and Ti, and have proven that Si doping is possible in the equilibrium process. Based on these results, we tried to manufacture an electrode by controlling the concentration of Ti as shown in Figure 3.19. In previous studies including Chapter 2, we optimized the TiCl₃ content to 7 μl when preparing Ti doped hematite. If more than 7 μl of TiCl₃ is injected, the efficiency of hematite decreases due to excess Ti doping as shown in Figure 3.19a. However, in Si:Ti-Fe₂O₃, it was confirmed that additional efficiency improvement was possible even if TiCl₃ was injected more than 7 μl. It is expected that an additional Ti doping level is needed to form an appropriate balance between Ti and Si as shown in Figures 3.19b and c. To maximize PEC efficiency, NiFeO_x co-catalyst was coated on Si:Ti-Fe₂O₃ electrode. NiFeO_x is a promising oxygen evolution catalyst for hematite-based PEC system and has excellent stability and fast kinetic reaction in basic electrolytes as shown in Figure 3.20. After loading the NiFeO_x co-catalyst, NiFeO_x/Si:Ti-Fe₂O₃ showed a photocurrent density of about 4.3 mA cm⁻² at 1.23V_{RHE}, an increase of around 7 times compared pristine Fe₂O₃ (0.6mA cm⁻²) with outstanding stability for 20 hours and Faradaic efficiency over 90%. Finally, we conducted an excellent reproducibility and scale-up test, which is an advantage that can be had when manufacturing hematite with the equilibrium process as shown in Figures 3.21 and 3.22. In scalability, we found that the active area expanded, the PEC performance reduced dramatically by FTO resistance.²⁹ Therefore, it is also one of key challenges that the hematite-based photoelectrode for scalability should solve.

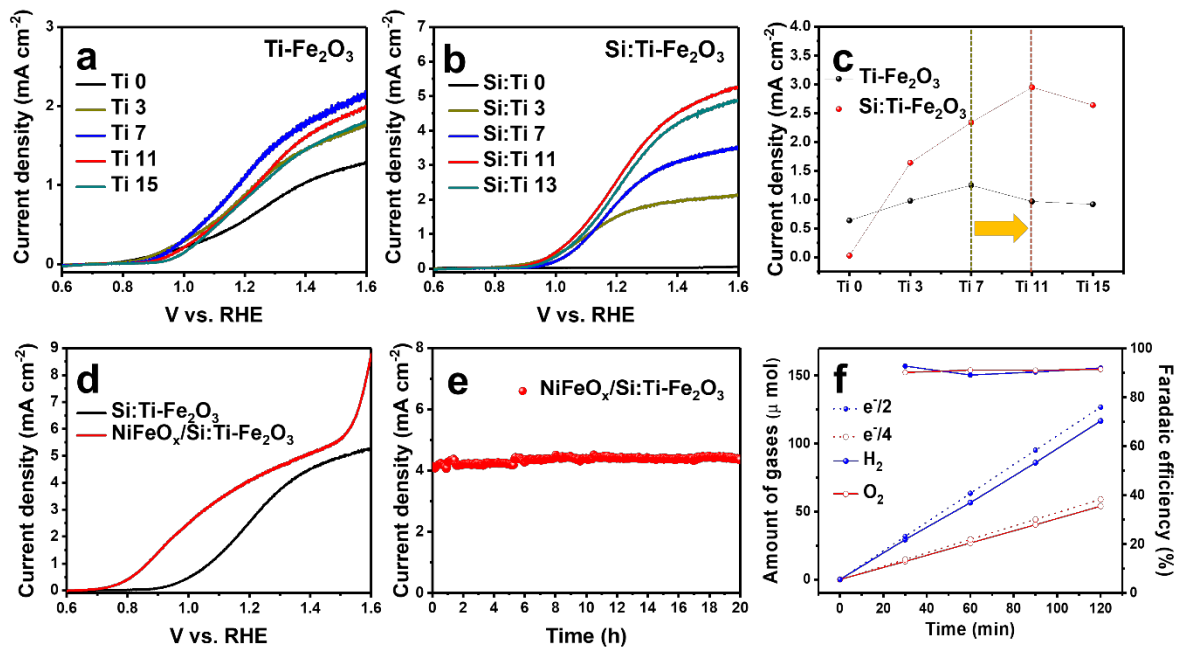


Figure 3.19. LSV curves of (a) Ti doped Fe₂O₃ and (b) Si and Ti co-doped Fe₂O₃ by injecting different Ti contents (Ti X = X μL of TiCl₃ in 100 mL of 150 mM FeCl₃). (c) Comparison of PEC efficiency by different Ti concentration at 1.23 V_{RHE}. (d) LSV curves after loading NiFeO_x on Si:Ti-Fe₂O₃. (e) Long-term stability test for NiFeO_x decorated Si and Ti co-doped Fe₂O₃ at 1.23 V_{RHE}. (f) Faradaic efficiency of NiFeO_x/Si:Ti-Fe₂O₃ at 1.23 V_{RHE}.

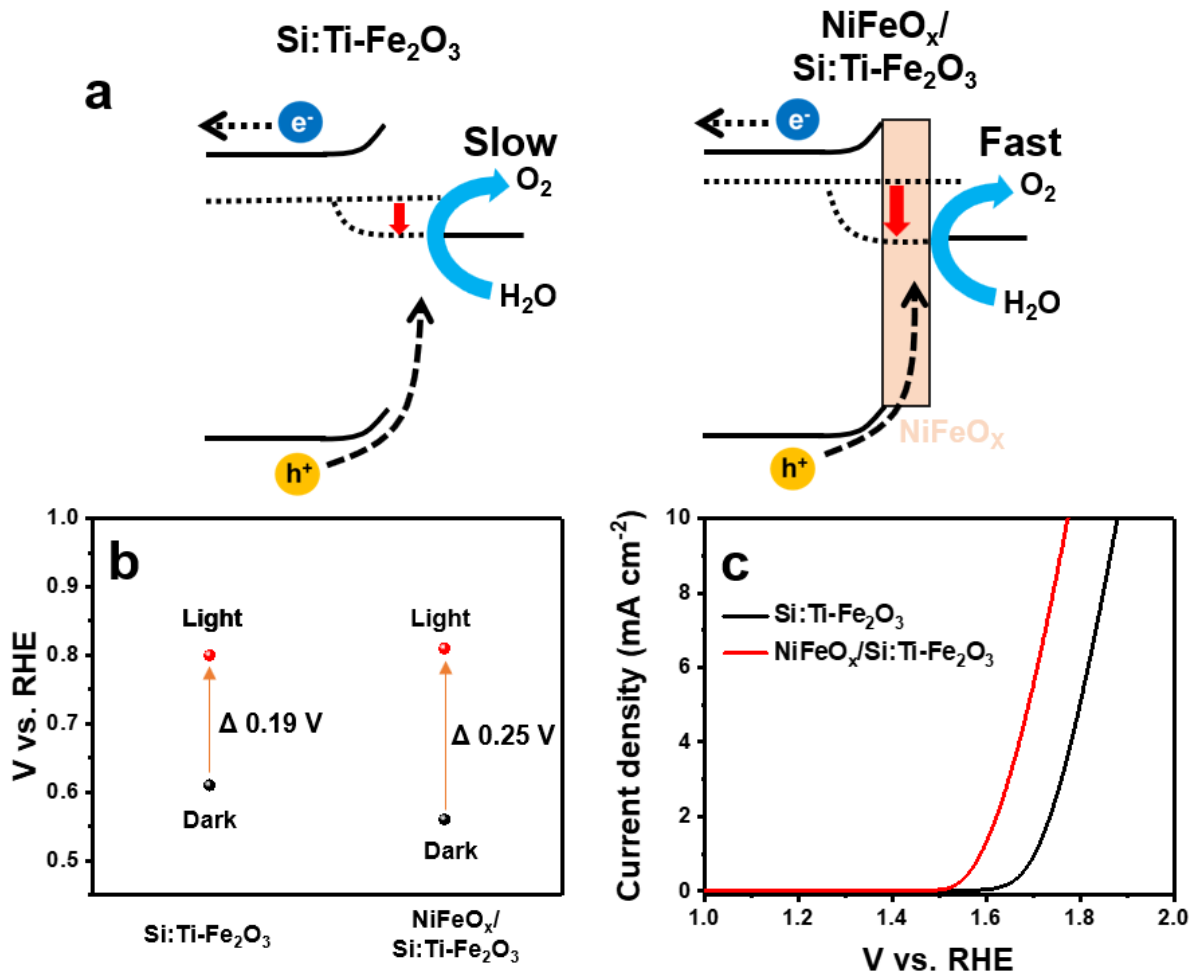


Figure 3.20. (a) A schematic illustration of a band diagram w/o a NiFeO_x catalyst. (b) Comparison of open circuit potentials of Si and Ti co-doped Fe₂O₃ and NiFeO_x coated Si and Ti co-doped Fe₂O₃. (c) Comparison of LSV curves for Si and Ti co-doped Fe₂O₃ and NiFeO_x coated Si:Ti-Fe₂O₃ in dark conditions.

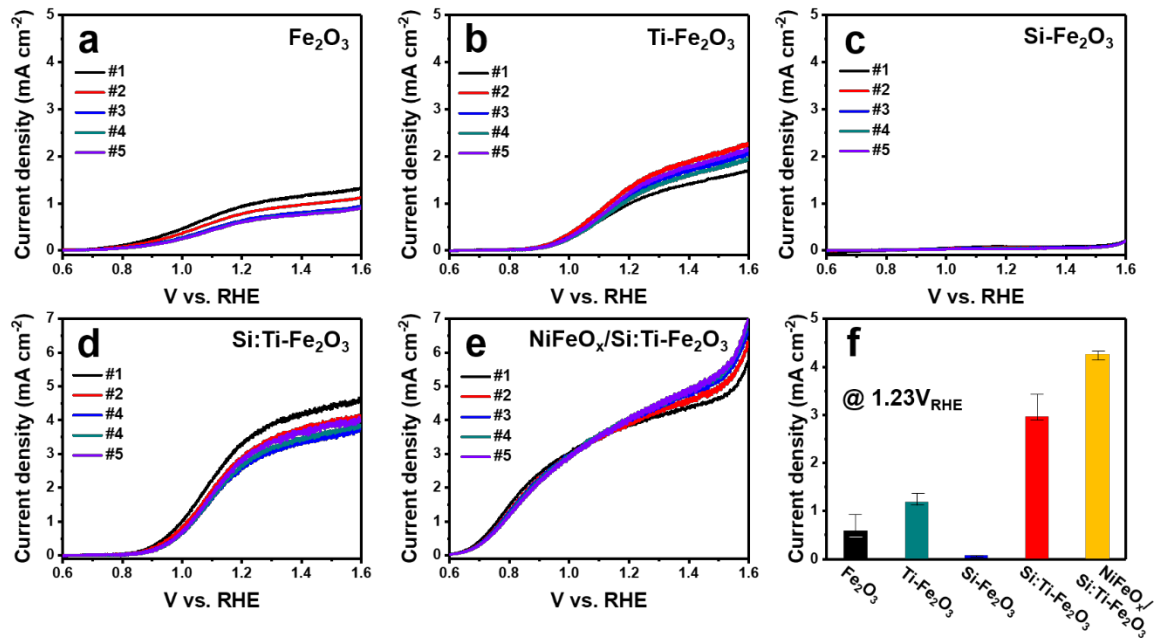


Figure 3.21. LSV curves of (a) Fe₂O₃, (b) Ti doped Fe₂O₃, (c) Si doped Fe₂O₃, (d) Si and Ti co-doped Fe₂O₃ and (e) NiFeO_x coated Si:Ti-Fe₂O₃ confirming the reproducibility of samples. (f) Statistical PEC performance data of samples at 1.23 V_{RHE}.

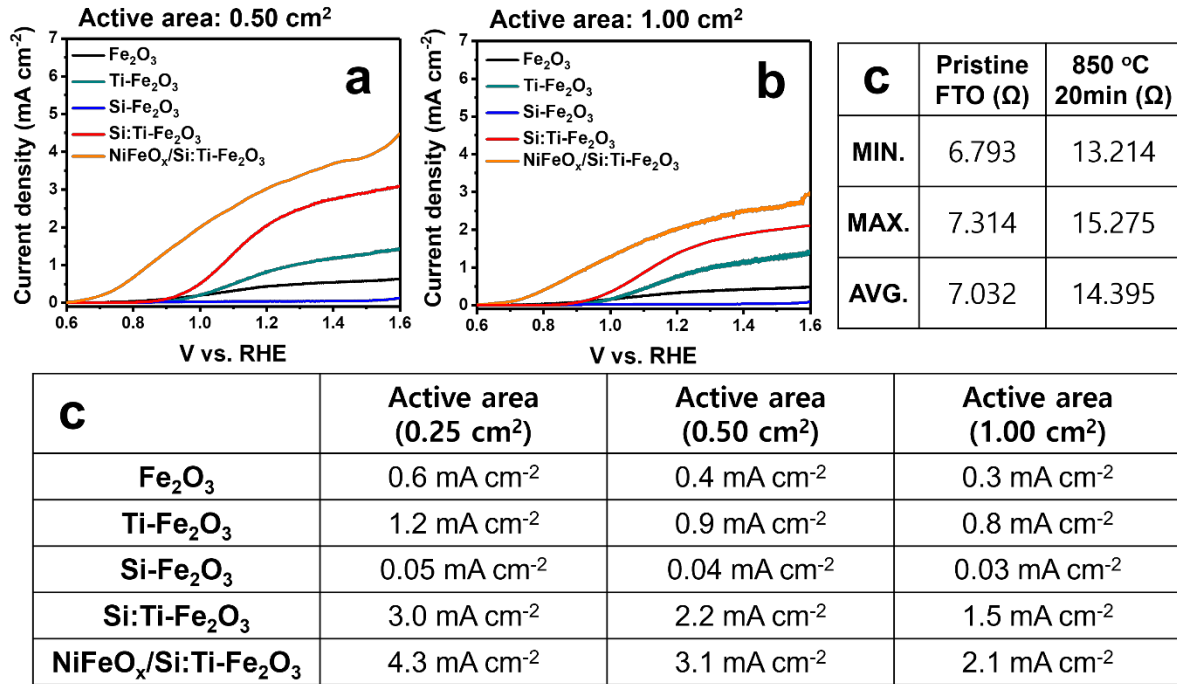


Figure 3.22. LSV curves with an active area of (a) 0.50 cm² and (b) 1.00 cm². (c) The comparison of FTO resistance before and after 850 °C annealing for 20 min. (d) Table for the current density of each sample at 1.23 V_{RHE} according to the active area.

3.4 Conclusion

In summary, we expanded the study of chapter 2 to the point of view of doping and proceeded to investigate the doping mechanism. Although hematite can be manufactured in a porous structure through the SiO_x overlayer, it has been proven that the Si diffusion that occurs at same time must be considered. $\text{Si-Fe}_2\text{O}_3$ without Ti dopant proved that Si doping is difficult through the equilibrium process due to higher formation energy than that of Sn. It was verified through DFT that Ti balances the Si for ion sizes and at the same time alleviates the structural charge repulsion in hematite caused by Si dopant. XRD, Raman, and XPS were used to confirm the effect of Si doping and crystallinity, and based on these considerations, it was possible to further improve the efficiency compared to previous studies. By fabricating NiFeO_x coated $\text{Si:Ti-Fe}_2\text{O}_3$, $\text{NiFeO}_x/\text{Si:Ti-Fe}_2\text{O}_3$ confirmed a photocurrent density of around 4.3 mA cm^{-2} . In addition, our manufacturing method has been proved to be excellent in reproducibility and large-scale manufacturing. The strategy studied in this work can be easily expanded to other photocatalysts with doping system to reach the great advancement in PEC water oxidation.

3.5 References

- (1) Park, J.; Yoon, K.-Y.; Kim, T.; Jang, H.; Kwak, M.-J.; Kim, J. Y.; Jang, J.-H. A Highly Transparent Thin Film Hematite with Multi-Element Dopability for an Efficient Unassisted Water Splitting System. *Nano Energy* **2020**, *76*, 105089. <https://doi.org/https://doi.org/10.1016/j.nanoen.2020.105089>.
- (2) Subramanian, A.; Gracia-Espino, E.; Annamalai, A.; Lee, H. H.; Lee, S. Y.; Choi, S. H.; Jang, J. S. Effect of Tetravalent Dopants on Hematite Nanostructure for Enhanced Photoelectrochemical Water Splitting. *Appl. Surf. Sci.* **2018**, *427*, 1203–1212. <https://doi.org/https://doi.org/10.1016/j.apsusc.2017.09.042>.
- (3) Seo, J. H.; Choi, K.; Nam, J.; Lee, H.; Lee, J. H. Synergetic Donor–Donor Codoping Strategy for Enhanced Photoelectrochemical Activity of Hematite. *Appl. Catal. B Environ.* **2020**, *260*, 118186. <https://doi.org/https://doi.org/10.1016/j.apcatb.2019.118186>.
- (4) Liu, J.; Liang, C.; Zhang, H.; Zhang, S.; Tian, Z. Silicon-Doped Hematite Nanosheets with Superlattice Structure. *Chem. Commun.* **2011**, *47* (28), 8040–8042. <https://doi.org/10.1039/C1CC12513C>.
- (5) Rahman, M.; Wadnerkar, N.; English, N. J.; MacElroy, J. M. D. The Influence of Ti- and Si-Doping on the Structure, Morphology and Photo-Response Properties of α -Fe₂O₃ for Efficient Water-Splitting: Insights from Experiment and First-Principles Calculations. *Chem. Phys. Lett.* **2014**, *592*, 242–246. <https://doi.org/https://doi.org/10.1016/j.cplett.2013.12.021>.
- (6) Cesar, I.; Sivula, K.; Kay, A.; Zboril, R.; Grätzel, M. Influence of Feature Size, Film Thickness, and Silicon Doping on the Performance of Nanostructured Hematite Photoanodes for Solar Water Splitting. *J. Phys. Chem. C* **2009**, *113* (2), 772–782. <https://doi.org/10.1021/jp809060p>.
- (7) Zhou, Z.; Huo, P.; Guo, L.; Prezhdo, O. V. Understanding Hematite Doping with Group IV Elements: A DFT+U Study. *J. Phys. Chem. C* **2015**, *119* (47), 26303–26310. <https://doi.org/10.1021/acs.jpcc.5b08081>.
- (8) Ahn, H.-J.; Yoon, K.-Y.; Kwak, M.-J.; Jang, J.-H. A Titanium-Doped SiO_x Passivation Layer for Greatly Enhanced Performance of a Hematite-Based Photoelectrochemical System. *Angew. Chemie Int. Ed.* **2016**, *55* (34), 9922–9926. <https://doi.org/https://doi.org/10.1002/anie.201603666>.
- (9) Yoon, K.-Y.; Ahn, H.-J.; Kwak, M.-J.; Kim, S.-I.; Park, J.; Jang, J.-H. A Selectively Decorated Ti-FeOOH Co-Catalyst for a Highly Efficient Porous Hematite-Based Water Splitting System. *J. Mater. Chem. A* **2016**, *4* (48), 18730–18736. <https://doi.org/10.1039/C6TA08273D>.
- (10) Kresse, G.; Joubert, D. From Ultrasoft Pseudopotentials to the Projector Augmented-Wave Method. *Phys. Rev. B* **1999**, *59* (3), 1758–1775. <https://doi.org/10.1103/PhysRevB.59.1758>.
- (11) Kresse, G.; Furthmüller, J. Efficient Iterative Schemes for Ab Initio Total-Energy Calculations Using a Plane-Wave Basis Set. *Phys. Rev. B* **1996**, *54* (16), 11169–11186. <https://doi.org/10.1103/PhysRevB.54.11169>.
- (12) Wang, L.; Maxisch, T.; Ceder, G. Oxidation Energies of Transition Metal Oxides within the $\text{GGA}+\text{U}$ Framework. *Phys. Rev. B* **2006**, *73* (19), 195107. <https://doi.org/10.1103/PhysRevB.73.195107>.
- (13) Finger, L. W.; Hazen, R. M. Crystal Structure and Isothermal Compression of Fe₂O₃, Cr₂O₃,

- and V₂O₃ to 50 Kbars. *J. Appl. Phys.* **1980**, *51* (10), 5362–5367.
<https://doi.org/10.1063/1.327451>.
- (14) Li, C.; Li, A.; Luo, Z.; Zhang, J.; Chang, X.; Huang, Z.; Wang, T.; Gong, J. Surviving High-Temperature Calcination: ZrO₂-Induced Hematite Nanotubes for Photoelectrochemical Water Oxidation. *Angew. Chemie Int. Ed.* **2017**, *56* (15), 4150–4155.
<https://doi.org/https://doi.org/10.1002/anie.201611330>.
- (15) Bykova, E.; Bykov, M.; Černok, A.; Tidholm, J.; Simak, S. I.; Hellman, O.; Belov, M. P.; Abrikosov, I. A.; Liermann, H.-P.; Hanfland, M.; Prakapenka, V. B.; Prescher, C.; Dubrovinskaia, N.; Dubrovinsky, L. Metastable Silica High Pressure Polymorphs as Structural Proxies of Deep Earth Silicate Melts. *Nat. Commun.* **2018**, *9* (1), 4789.
<https://doi.org/10.1038/s41467-018-07265-z>.
- (16) Pan, H.; Ao, D.; Qin, G. Synergistic Effects of Dopant (Ti or Sn) and Oxygen Vacancy on the Electronic Properties of Hematite: A DFT Investigation. *RSC Adv.* **2020**, *10* (39), 23263–23269. <https://doi.org/10.1039/D0RA01450H>.
- (17) Jeon, T. H.; Bokare, A. D.; Han, D. S.; Abdel-Wahab, A.; Park, H.; Choi, W. Dual Modification of Hematite Photoanode by Sn-Doping and Nb₂O₅ Layer for Water Oxidation. *Appl. Catal. B Environ.* **2017**, *201*, 591–599.
<https://doi.org/https://doi.org/10.1016/j.apcatb.2016.08.059>.
- (18) Annamalai, A.; Subramanian, A.; Kang, U.; Park, H.; Choi, S. H.; Jang, J. S. Activation of Hematite Photoanodes for Solar Water Splitting: Effect of FTO Deformation. *J. Phys. Chem. C* **2015**, *119* (7), 3810–3817. <https://doi.org/10.1021/jp512189c>.
- (19) Chemelewski, W. D.; Hahn, N. T.; Mullins, C. B. Effect of Si Doping and Porosity on Hematite's (α -Fe₂O₃) Photoelectrochemical Water Oxidation Performance. *J. Phys. Chem. C* **2012**, *116* (8), 5255–5261. <https://doi.org/10.1021/jp210877u>.
- (20) Zhang, M.; Luo, W.; Li, Z.; Yu, T.; Zou, Z. Improved Photoelectrochemical Responses of Si and Ti Codoped α -Fe₂O₃ Photoanode Films. *Appl. Phys. Lett.* **2010**, *97* (4), 42105.
<https://doi.org/10.1063/1.3470109>.
- (21) Kay, A.; Cesar, I.; Grätzel, M. New Benchmark for Water Photooxidation by Nanostructured α -Fe₂O₃ Films. *J. Am. Chem. Soc.* **2006**, *128* (49), 15714–15721.
<https://doi.org/10.1021/ja064380l>.
- (22) Kang, M. J.; Kang, Y. S. Ultrathin Insulating Under-Layer with a Hematite Thin Film for Enhanced Photoelectrochemical (PEC) Water Splitting Activity. *J. Mater. Chem. A* **2015**, *3* (30), 15723–15728. <https://doi.org/10.1039/C5TA03468J>.
- (23) Li, M.; Yang, Y.; Ling, Y.; Qiu, W.; Wang, F.; Liu, T.; Song, Y.; Liu, X.; Fang, P.; Tong, Y.; Li, Y. Morphology and Doping Engineering of Sn-Doped Hematite Nanowire Photoanodes. *Nano Lett.* **2017**, *17* (4), 2490–2495. <https://doi.org/10.1021/acs.nanolett.7b00184>.
- (24) Kim, J. Y.; Magesh, G.; Youn, D. H.; Jang, J.-W.; Kubota, J.; Domen, K.; Lee, J. S. Single-Crystalline, Wormlike Hematite Photoanodes for Efficient Solar Water Splitting. *Sci. Rep.* **2013**, *3* (1), 2681. <https://doi.org/10.1038/srep02681>.
- (25) Jang, J.-W.; Du, C.; Ye, Y.; Lin, Y.; Yao, X.; Thorne, J.; Liu, E.; McMahon, G.; Zhu, J.; Javey, A.; Guo, J.; Wang, D. Enabling Unassisted Solar Water Splitting by Iron Oxide and Silicon. *Nat. Commun.* **2015**, *6* (1), 7447. <https://doi.org/10.1038/ncomms8447>.
- (26) Tang, P.-Y.; Han, L.-J.; Hegner, F. S.; Paciok, P.; Biset-Peiró, M.; Du, H.-C.; Wei, X.-K.; Jin,

- L.; Xie, H.-B.; Shi, Q.; Andreu, T.; Lira-Cantú, M.; Heggen, M.; Dunin-Borkowski, R. E.; López, N.; Galán-Mascarós, J. R.; Morante, J. R.; Arbiol, J. Boosting Photoelectrochemical Water Oxidation of Hematite in Acidic Electrolytes by Surface State Modification. *Adv. Energy Mater.* **2019**, *9* (34), 1901836. <https://doi.org/10.1002/aenm.201901836>.
- (27) Tang, P.; Arbiol, J. Engineering Surface States of Hematite Based Photoanodes for Boosting Photoelectrochemical Water Splitting. *Nanoscale Horizons* **2019**, *4* (6), 1256–1276. <https://doi.org/10.1039/C9NH00368A>.
- (28) Puthirath Balan, A.; Radhakrishnan, S.; Woellner, C. F.; Sinha, S. K.; Deng, L.; Reyes, C. de los; Rao, B. M.; Paulose, M.; Neupane, R.; Apte, A.; Kochat, V.; Vajtai, R.; Harutyunyan, A. R.; Chu, C.-W.; Costin, G.; Galvao, D. S.; Martí, A. A.; van Aken, P. A.; Varghese, O. K.; Tiwary, C. S.; Malie Madom Ramaswamy Iyer, A.; Ajayan, P. M. Exfoliation of a Non-van Der Waals Material from Iron Ore Hematite. *Nat. Nanotechnol.* **2018**, *13* (7), 602–609. <https://doi.org/10.1038/s41565-018-0134-y>.
- (29) Qayum, A.; Guo, M.; Wei, J.; Dong, S.; Jiao, X.; Chen, D.; Wang, T. An in Situ Combustion Method for Scale-up Fabrication of BiVO₄ Photoanodes with Enhanced Long-Term Photostability for Unassisted Solar Water Splitting. *J. Mater. Chem. A* **2020**, *8* (21), 10989–10997. <https://doi.org/10.1039/D0TA03557B>.
- (30) Yoon, K.-Y.; Park, J.; Lee, H.; Seo, J. H.; Kwak, M.-J.; Lee, J. H.; Jang, J.-H. Unveiling the Role of the Ti Dopant and Viable Si Doping of Hematite for Practically Efficient Solar Water Splitting. *ACS Catal.* **2022**, *12* (9), 5112–5122. <https://doi.org/10.1021/acscatal.1c05106>.

Chapter 4. NiFeO_x decorated Ge-hematite/perovskite for an efficient tandem water splitting system

*Chaper4 is reproduced in part with permission of “Yoon, K.-Y.; Park, J.; Jung, M.; Ji, S.-G.; Lee, H.; Seo J. H.; Kwak, M.-J.; Seok, S. I.; Lee, J. H.; and Jang, J.-H.”³⁶ Copyright © 2021 Springer Nature.

4.1 Introduction

In Chapters 2 and 3, we verified that effective structural control is possible using the overlayer, but the doping part due to the diffusion of the overlayer's constituent materials should be considered and it has also been proven that the consideration for can be approximated with the formation energy for doping.^{1,2} Based on the doping system through the overlayer we made, we decided to try manufacturing Ge doped hematite. In many theoretical doping designs,³⁻⁶ Ge is known to be the most suitable dopant for hematite.⁷ Ge⁴⁺ has an ionic radius almost identical to that of Fe³⁺, and it has been reported that it can improve the crystallinity of hematite. Therefore, many researchers have tried to use Ge dopant with favorable properties for hematite, but lower efficiency has been reported compared to Sn,⁸⁻¹² Si,¹³⁻¹⁶ and Ti¹⁷⁻²¹ dopants that have been typically used. The discrepancy between the theoretical design and the experimental results must be resolved through a rational method, and the causes of the discrepancy must be resolved to enable a more optimized hematite doping design in the future. We hypothesized that the cause of this discrepancy might be due to the interaction of Sn and Ge. Because Sn doping from FTO is a phenomenon that occurs only in a specific manufacturing method,²² and this Sn doping is not considered when designing a theoretical doping design. We have already confirmed that Sn was suppressed from FTO by the method of manufacturing porous hematite using the overlayer. Here, we attempted to fabricate Ge-doped porous hematite using a GeO₂ overlayer. GeO₂ overlayer can also make porous hematite, and it has been confirmed that Sn doping is also suppressed. In this process, we confirmed that the interaction of Ge and Sn adversely affects the efficiency of hematite. After maximizing the efficiency of hematite using NiFeO_x co-catalyst, a tandem device was constructed using perovskite solar cell (PSC). A photocurrent density of 3.9 mA cm⁻² was confirmed in the tandem device configured in our study. without an external voltage applied. Our doping system that we have verified can serve as a stepping-stone to improving the efficiency of hematite, which is currently stagnant in PEC system of hematite photoanode.

4.2 Experimental section

4.2.1 Fabrication of Fe₂O₃ and Ge doped hematite (Ge-H) photoanode.

Fe₂O₃ photoanode was prepared by hydrothermal method under the same conditions as chapters 2 and 3. Briefly, using 150 mM FeCl₃ solution and reacting at 100 °C for 3 hours, FeOOH nanorods were grown on FTO substrate. Then, heat treatment was performed at 800 °C for 20 min through a furnace. Ge doped Fe₂O₃ (Ge-H) photoanode was manufactured through the following process. After dissolving 40 mM GeO₂ powder in D.I. water, 500 μl of Ge solution was added to 100 ml of 150mM FeCl₃ solution and reacting at 100 °C for 3 hours, Ge doped FeOOH nanorods were grown on FTO substrate. Then, heat treatment was performed at 800 °C for 20 min through a furnace.

4.2.2 Fabrication of Ge doped porous hematite (Ge-PH) photoanode.

Ge doped porous Fe₂O₃ (Ge-PH) photoanode was manufactured through the following process. After growing FeOOH nanorods on the FTO substrate in the same manner as in the Fe₂O₃ manufacturing process, FeOOH nanorods was immersed in 40 mM GeO₂ solution for 30min and washed with D.I. water. Then, heat treatment was performed at 800 °C for 20 min through a furnace.

4.2.3 Fabrication of NiFeO_x decorated Ge-PH photoanode.

To load the NiFeO_x OER co-catalyst Ge-PH photoanode, precursors, nickel(II) 2-ethylhexanoate (78% w/w in 2-ethylhexanoic acid) as Ni source and iron(III) 2-ethylhexanoate (50% w/w in mineral spirits) as iron source is mixed in hexane solution. After making stock solution by mixture, the dilution was conducted to 50 mM metal complex. The loading of NiFeO_x on Si:Ti-Fe₂O₃ was achieved by spin coating method and then, the electrode was exposed with UV light for 1h. Final step was that the electrode is annealed at 100 °C for 1h.

4.2.4 PEC measurements.

PEC measurements were carried out as half-cell measurements. The half-cell test was based on a three-electrode system made of an Ag/AgCl electrode by KCl saturated solution and a platinum mesh as reference and counter parts, respectively. The exposed area for measuring PEC efficiency was fixed at 0.44 cm² by O-ring. The electrolyte was applied as 1M NaOH (pH=13.6) in all PEC measurements. The

scan rate is the same for all of them at 20 mVs^{-1} . EIS results were fitted using Z-view software for accurate analysis. IPCE measurement was conducted out by Xe lamp with monochromatic light.

4.2.5 Synthesis of methylammonium iodide (MAI).

To synthesize methylammonium iodide, 57% aqueous hydroiodic acid (HI, 30 mL) was added in to 40% aqueous methylamine (19.6 mL) solution with vigorous stirring for 2 hours under an ice bath. The solvent was removed under vacuum and the products was dissolved in ethanol and it is recrystallized in diethyl ether. The recrystallized products were collected through the filtration and the collected products were dried at $60 \text{ }^\circ\text{C}$ under vacuum condition.

4.2.6 Synthesis of FAPbI₃ and MAPbBr₃ powders.

FAPbI₃ powders were synthesized by dissolving FAI and PbI₂ in 2-methoxyethanol with vigorous stirring at $120 \text{ }^\circ\text{C}$ for 30 min and MAPbBr₃ powders were synthesized by dissolving MAI and PbBr₂ in 2-methoxyethanol with vigorous stirring at $100 \text{ }^\circ\text{C}$ for 30 min. The FAPbI₃ and MAPbBr₃ were gathered by filtration and dried under vacuum condition.

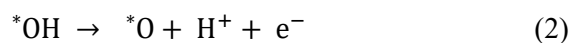
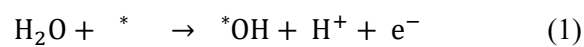
4.2.7 Photovoltaic device fabrication.

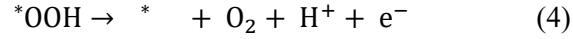
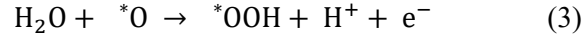
First, for coating of TiO₂ hole blocking layer (bl-TiO₂), FTO substrate (Pilkington, TEC8) was rinsed in detergent, acetone, and ethanol by using ultrasonic for 30 min, respectively. Titanium diisopropoxide bis(acetylacetonate) solution as precursor solution diluted in ethanol solvent with a 1:10 ratio (v:v) and The diluted solution was sprayed onto the FTO substrate at $450 \text{ }^\circ\text{C}$. TiO₂ particles (average size was around 50 nm) were coated on the bl-TiO₂/FTO substrate by spin coating at 1500 rpm for 50 s and then, mesoporous TiO₂ layer (mp-TiO₂) was formed on bl-TiO₂/FTO substrate. After annealing at $500 \text{ }^\circ\text{C}$ for 1 hour in air condition, the prepared FaPbI₃ and MAPbBr₃ powders were dissolved in in the mixed solution. The mixed solution is made in a 4:1 volume ratio of N-N-dimethylformamide (DMF) and dimethylsulfoxide (DMSO) at $60 \text{ }^\circ\text{C}$ for 1 hour under stirring. The prepared perovskite solution is loaded on the mp-TiO₂/bl-TiO₂/FTO substrate using various spin coating conditions at 1000-5000 rpm for 15-20s. After 10 seconds during the second spin coating step, 1 mL of ether is dropped onto the substrate. After spin coating was completed, heat treatment was performed at $150 \text{ }^\circ\text{C}$ for 10 min. For loading of organic-based hole conducting material, 2,2',7,7'-tetrakis-(N,N-di-4-methoxyphenylamino)-9,9'-spirobifluorene (spiro-OMeTAD) (88 mg in 1 mL of chlorobenzene) were mixed in lithium

bis(trifluoromethanesulfonyl)imide (Li-TFSI) solution (7.5 μL) in acetonitrile (170 mg mL^{-1}) and 7.5 μL of 4-tert-butylpyridine (tBP). After synthesizing the hole conducting material, the hole conducting material was loaded on the perovskite/mpTiO₂/bl-TiO₂/FTO by spin coating at 3000 rpm for 30 s. Finally, a gold layer was deposited on the hole conducting layer using a thermal evaporator.

4.2.8 DFT calculation details.

The first principle density functional theory calculations were executed in the spin-polarized framework along with the projector augmented wave (PAW) approach²³ using the Vienna ab-initio simulation package (VASP).²⁴ The exchange-correlation functional was considered using the generalized gradient approximation (GGA) in Perdew, Burke, and Ernzerhof (PBE) parameterization.²⁵ The cut-off energy for the planewave basis was set to 500 eV, and Monkhorst-Pack k-point mesh of $4 \times 4 \times 1$ was used for calculation of density of state of all the slab structure of $\alpha\text{-Fe}_2\text{O}_3$ (hematite). All the ionic positions were relaxed *via* conjugate gradient method until atomic force convergence of 0.01 eV \AA^{-1} was achieved. In case of transition metal oxide systems 3d electronic states are strongly correlated, hence considering the same, we employed the spin polarized GGA + U formalism due to improper action of d-electrons with standard DFT.²⁶ The GGA + U calculations depends on the values of U-J and were set to 4.2 eV which are in accordance with the experimental band gap value of hematite (2.2 eV). The hexagonal unit cell of $\alpha\text{-Fe}_2\text{O}_3$ was optimized with a layered antiferromagnetic (AFM) ordering. In case of pure $\alpha\text{-Fe}_2\text{O}_3$ unit cell, the lattice parameters calculated within PBE + U and found to be $a = b = 5.07 \text{ \AA}$ and $c = 13.88 \text{ \AA}$, and consistent with the experimental values of $a = b = 5.04 \text{ \AA}$ and $c = 13.75 \text{ \AA}$.²⁷ The lattice parameters of bulk structure of pristine and Ge-doped $\alpha\text{-Fe}_2\text{O}_3$ were determined by using their fully relaxed (1×1) slab structure. To minimize the interaction between the periodic images along z-axis, a vacuum layer of at least 12 \AA was applied along z-axis. As it is renowned that, (0001) surface is one of the natural growth faces of $\alpha\text{-Fe}_2\text{O}_3$, hence, we focused on the surface interaction reaction on (0001) surface of $\alpha\text{-Fe}_2\text{O}_3$. Substitution of dopant species were made at both outmost Fe layers to achieve the maximum of the doping effect on surface reactions and to eliminate the polarization from broken symmetry. Hydrogen passivation was used to prevent the transfer of hydrogen atoms from the active site to the other surface oxygen. We passivated only one of the three surface oxygen atoms to minimize the hydrogen bonding that affects the reaction. We considered the following OER mechanism with four elementary steps.





The * represents chemisorption with the reactive sites on the surface. According to Rossemiesl et al., at standard conditions (pH=0, p=1bar, T=298K), the reaction free energy (ΔG) of each step is calculated as follows:

$$\Delta G_A = \Delta E_{*_{\text{OH}}} + (\Delta \text{ZPE} - T\Delta S)_A - e \cdot \Phi \quad (5)$$

$$\Delta G_B = \Delta E_{*_{\text{O}}} - \Delta E_{*_{\text{OH}}} + (\Delta \text{ZPE} - T\Delta S)_B - e \cdot \Phi \quad (6)$$

$$\Delta G_C = \Delta E_{*_{\text{OOH}}} - \Delta E_{*_{\text{O}}} + (\Delta \text{ZPE} - T\Delta S)_C - e \cdot \Phi \quad (7)$$

$$\Delta G_D = 4.92\text{eV} - \Delta E_{*_{\text{OOH}}} + (\Delta \text{ZPE} - T\Delta S)_D - e \cdot \Phi \quad (8)$$

$\Delta E_{*_{\text{OH}}}$, $\Delta E_{*_{\text{O}}}$ and $\Delta E_{*_{\text{OOH}}}$ are the binding energies for the adsorption of OH, O and OOH, respectively. ZPE is the zero-point energy and $T\Delta S$ is entropic contributions. Φ is the external potential. At the standard condition with $\Phi=0$, the highest free energy (ΔG_{max}) is equal to reaction potential for electrochemical reaction potential and ($\Delta G_{\text{max}} - 1.23$) is equal to overpotential (η).

4.3 Results and discussion

To confirm the Ge doping effect, three types of hematite were prepared as shown in Figure 4.1a. First, a general Fe_2O_3 manufactured by a hydrothermal method was manufactured,^{28,29} and it has a nonporous structure. The morphology of Fe_2O_3 was confirmed through SEM and TEM images to form nanorods with a diameter of about 70 nm and a length of 300 nm as shown in Figure 4.1b. Second, Ge doped hematite (Ge-H) was manufactured by adding Ge dopant to FeCl_3 in a similar way to the Ge doping method in previous studies, growing Ge doped FeOOH on FTO, and then annealed at 800 °C for 20 min. Ge-H had a nonporous structure similar to that of Fe_2O_3 with a diameter of about 70 nm and a length of 300 nm as shown in Figure 4.1c. The morphology of FeOOH and Ge- FeOOH was also almost similar as shown in Figure 4.2. Third, Ge doped porous Fe_2O_3 (Ge-PH) was fabricated utilizing a GeO_2 overlayer. FeOOH nanorods were immersed in GeO_2 solution for 30 min and then, a thin GeO_2 layer was formed on FeOOH surface as shown in Figure 4.3. After annealing process, hematite has confirmed to have a porous structure by GeO_2 overlayer as shown in Figure 4.1d. Through STEM-EDX, it was confirmed that Ge was uniformly doped over the entire region of Ge-PH as shown in Figures 4.1e-i. The mechanism by which the porous structure is formed is due to water evaporation¹⁹ and the Kirkendall effect,¹ as described in Chapter 3. Since Ge-PH also has a porous structure, in addition to the Ge doping effect, it can have the effect of reducing the recombination probability by improving the OER sites and shortening the distance of hole diffusion. We evaluated the PEC efficiency of three types of hematite as shown in Figure 4.4a. Pristine Fe_2O_3 showed a photocurrent density of $\sim 1.0 \text{ mA cm}^{-2}$ at $1.23 V_{\text{RHE}}$, whereas Ge-H showed a photocurrent density of $\sim 1.9 \text{ mA cm}^{-2}$ at $1.23 V_{\text{RHE}}$ due to the Ge doping effect. Ge-PH showed a photocurrent density of 3.5 mA cm^{-2} and showed 3.5 times more efficiency than pristine Fe_2O_3 and 1.8 times better than Ge-H photoanode. The reason for the high increase in the photocurrent density of Ge-PH is that there are effects due to Ge doping and porous structure. Therefore, it is necessary to further verify the superiority of Ge. To prove the superiority of Ge, we fabricated hematites with similar porous structures using various overlayers as shown in Figure 4.5. Through SEM and BET analysis, porous hematite doped with Sn, Ti, and Si was confirmed, and it was confirmed that the structure was almost similar to that of Ge-PH, but Ge showed the best activity in ECSA measurement. Moreover, in PEC efficiency, Ge-PH showed the highest photocurrent density. Therefore, it has been proven that Ge dopant shows the best efficiency, proving that Ge is the best dopant as a theoretical doping design.⁷ Although Ge-PH showed the highest efficiency in the porous structures, it is necessary to elucidate the cause of the lower efficiency of Ge-H compared to doped hematites with other nonporous structures. Therefore, we proceeded with a more in-depth analysis of this part.

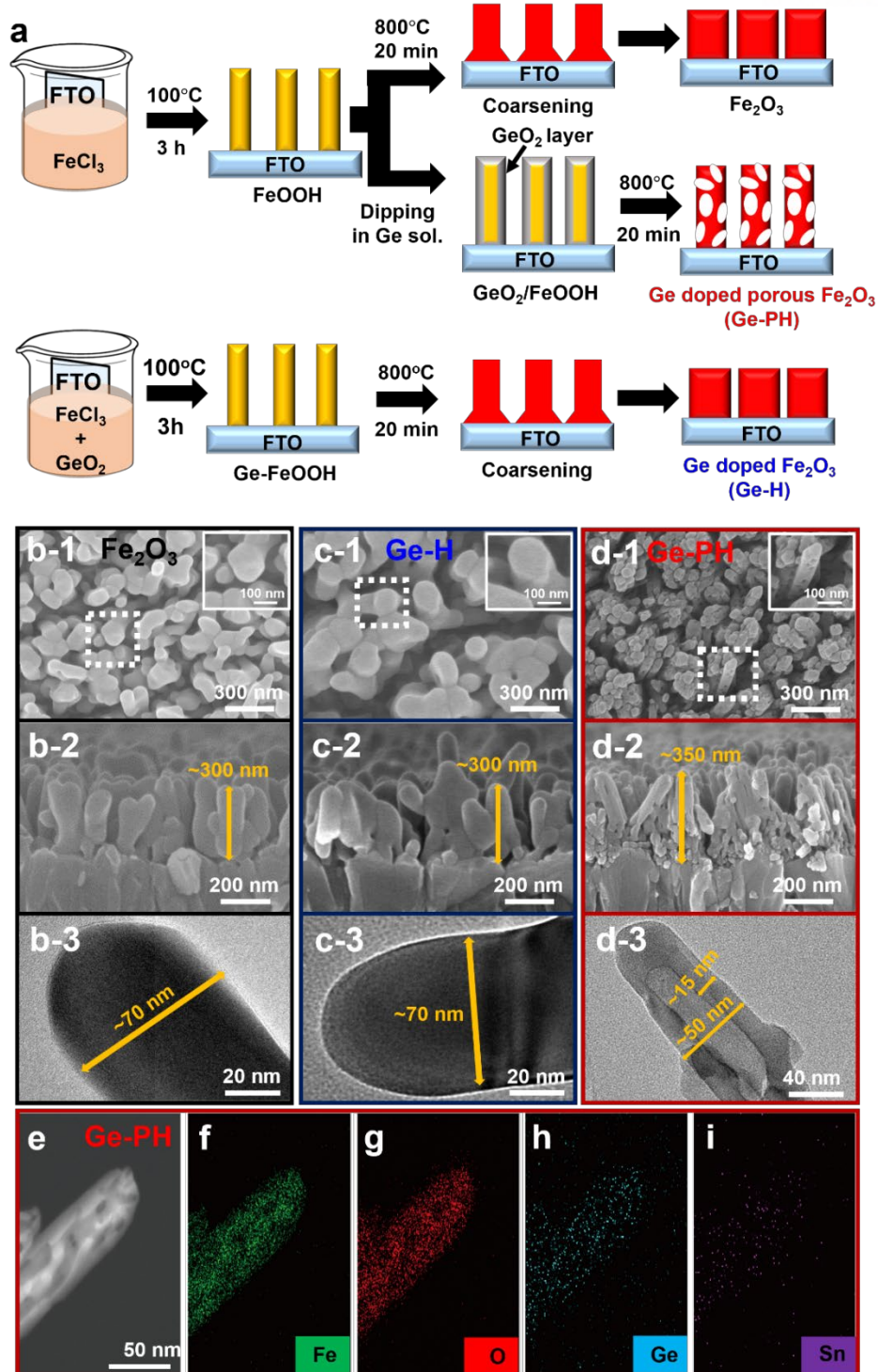


Figure 4.1. (a) Schematic images for Ge doping strategy. (b) top-view and cross-sectional SEM and TEM images for (b) Fe_2O_3 , (c) Ge-H and (d) Ge-PH. (e) Scanning transmission electron microscopy (STEM) image of Ge-PH and the corresponding mapping element of (f) Fe, (g) O, (h) Ge and (i) Sn.

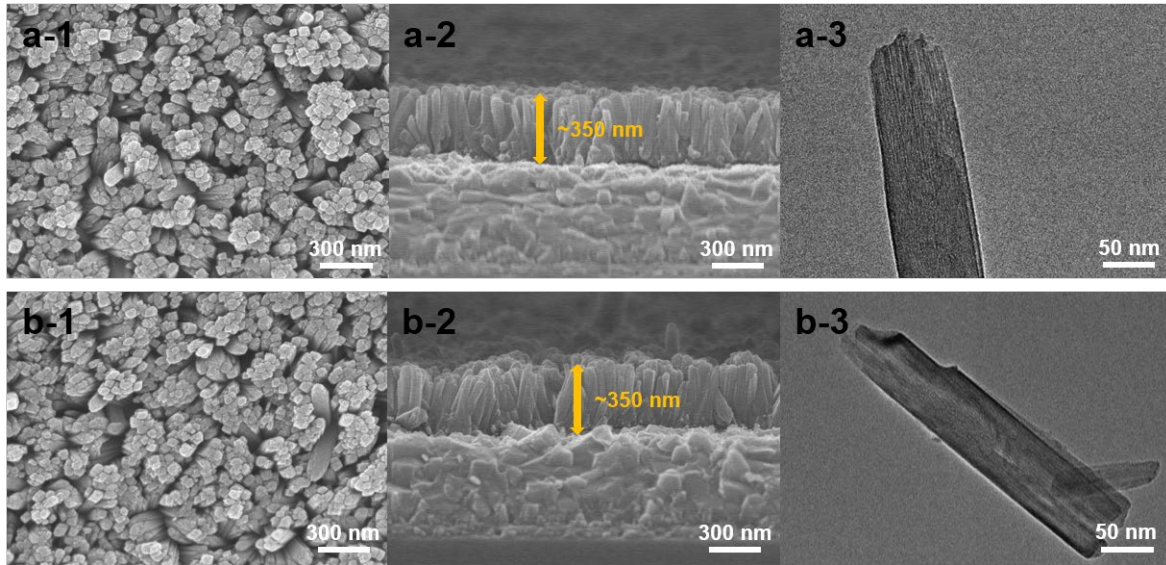


Figure 4.2. The top-view (a-1 and b-1) and cross-sectional (a-2 and b-2) SEM images and a TEM image (a-3 and b-3) of (a) FeOOH nanorod and (b) Ge-doped FeOOH nanorod.

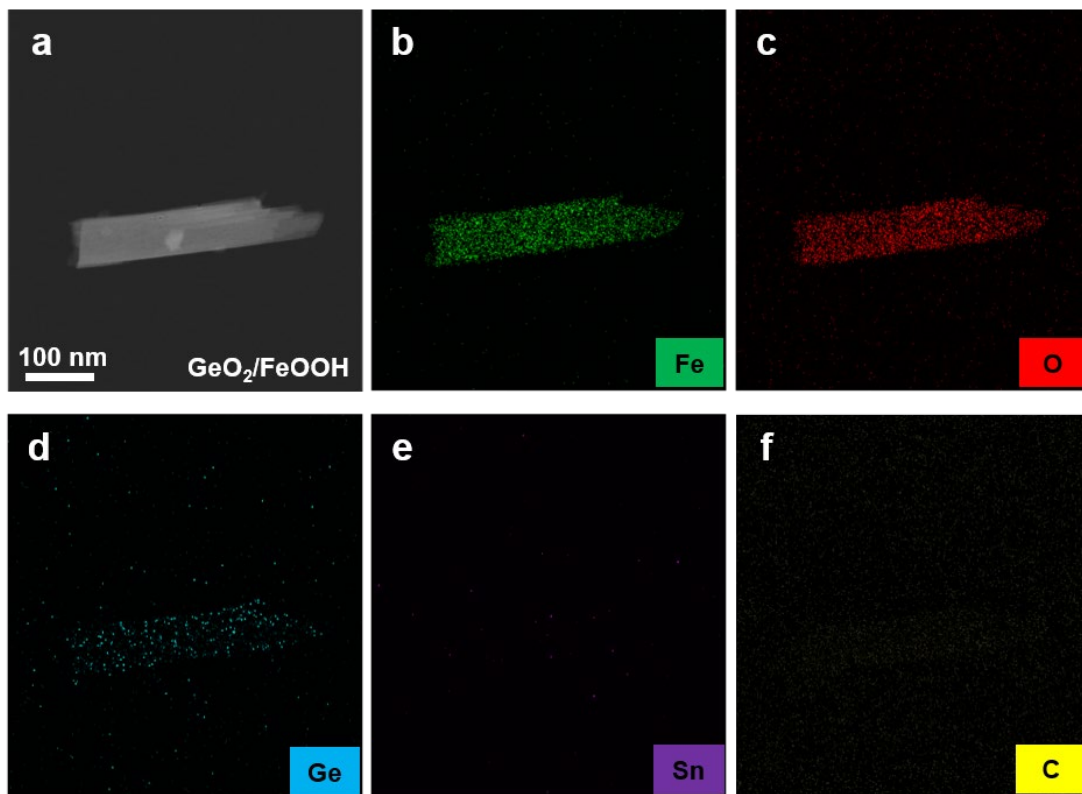


Figure 4.3. (a) STEM image of the entire GeO₂/FeOOH nanorod and the corresponding elemental mapping image of (b) Fe, (c) O, (d) Ge, (e) Sn and (f) C.

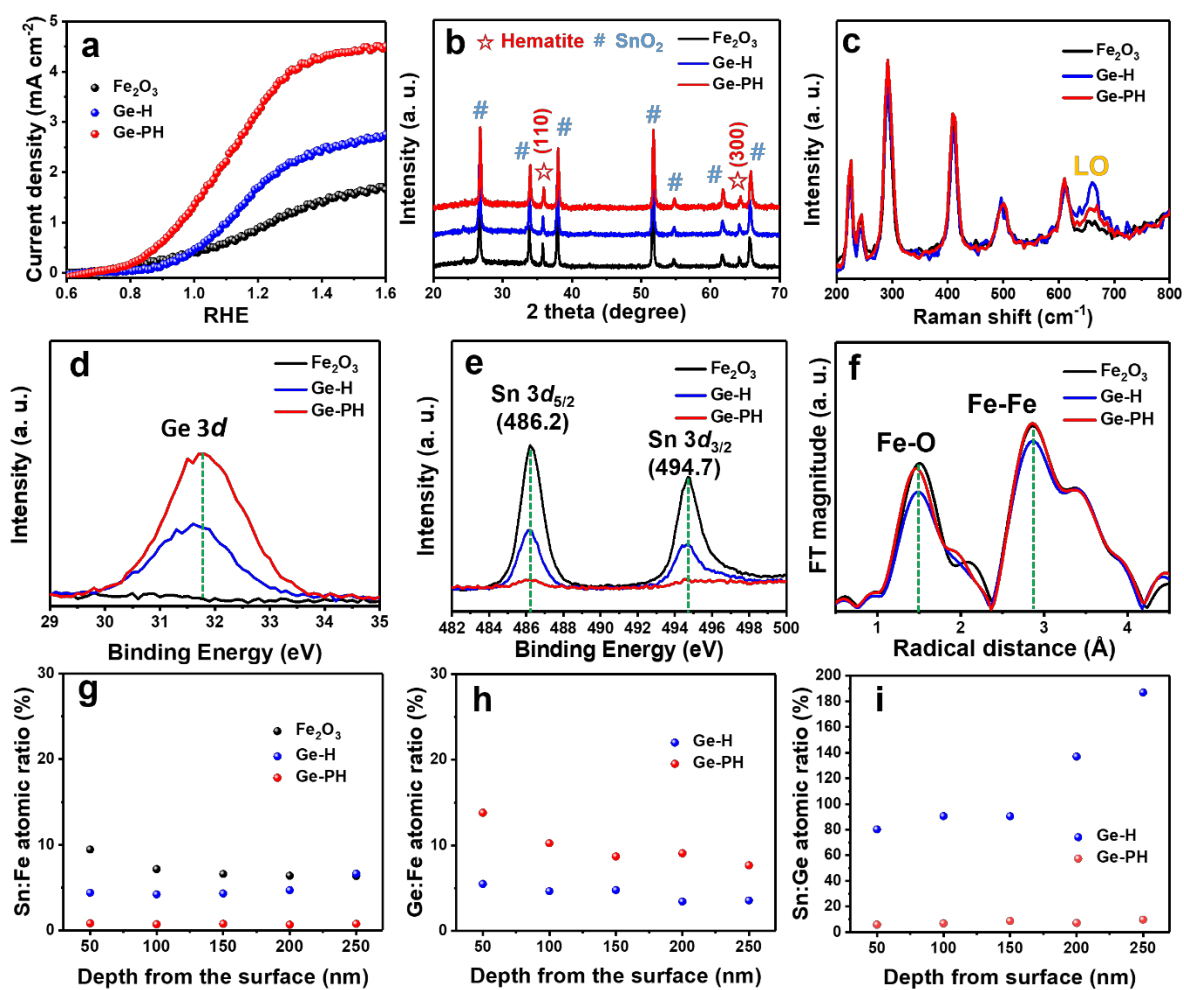


Figure 4.4. (a) LSV curves of Fe₂O₃, nonporous Fe₂O₃ with Ge doping (Ge-H), and porous Fe₂O₃ with Ge doping (Ge-PH) in basic electrolyte (1 M NaOH (pH = 13.6)) under 1 SUN illumination. (b) XRD patterns of Fe₂O₃, nonporous Fe₂O₃ with Ge doping (Ge-H), and porous Fe₂O₃ with Ge doping (Ge-PH) and (c) Raman spectra of Fe₂O₃, nonporous Fe₂O₃ with Ge doping (Ge-H), and porous Fe₂O₃ with Ge doping (Ge-PH). XPS signals for (d) Ge 3d of Fe₂O₃, nonporous Fe₂O₃ with Ge doping (Ge-H), and porous Fe₂O₃ with Ge doping (Ge-PH), and (e) Sn 3d of Fe₂O₃, nonporous Fe₂O₃ with Ge doping (Ge-H), and porous Fe₂O₃ with Ge doping (Ge-PH). (f) Fourier transform of the EXAFS data at the Fe k-edge of the hematite nanostructures in Fe₂O₃, nonporous Fe₂O₃ with Ge doping (Ge-H), and porous Fe₂O₃ with Ge doping (Ge-PH). The depth profiles by XPS measurements for (g) Sn and (h) Ge contents. (i) Calculated Sn:Ge doping ratio.

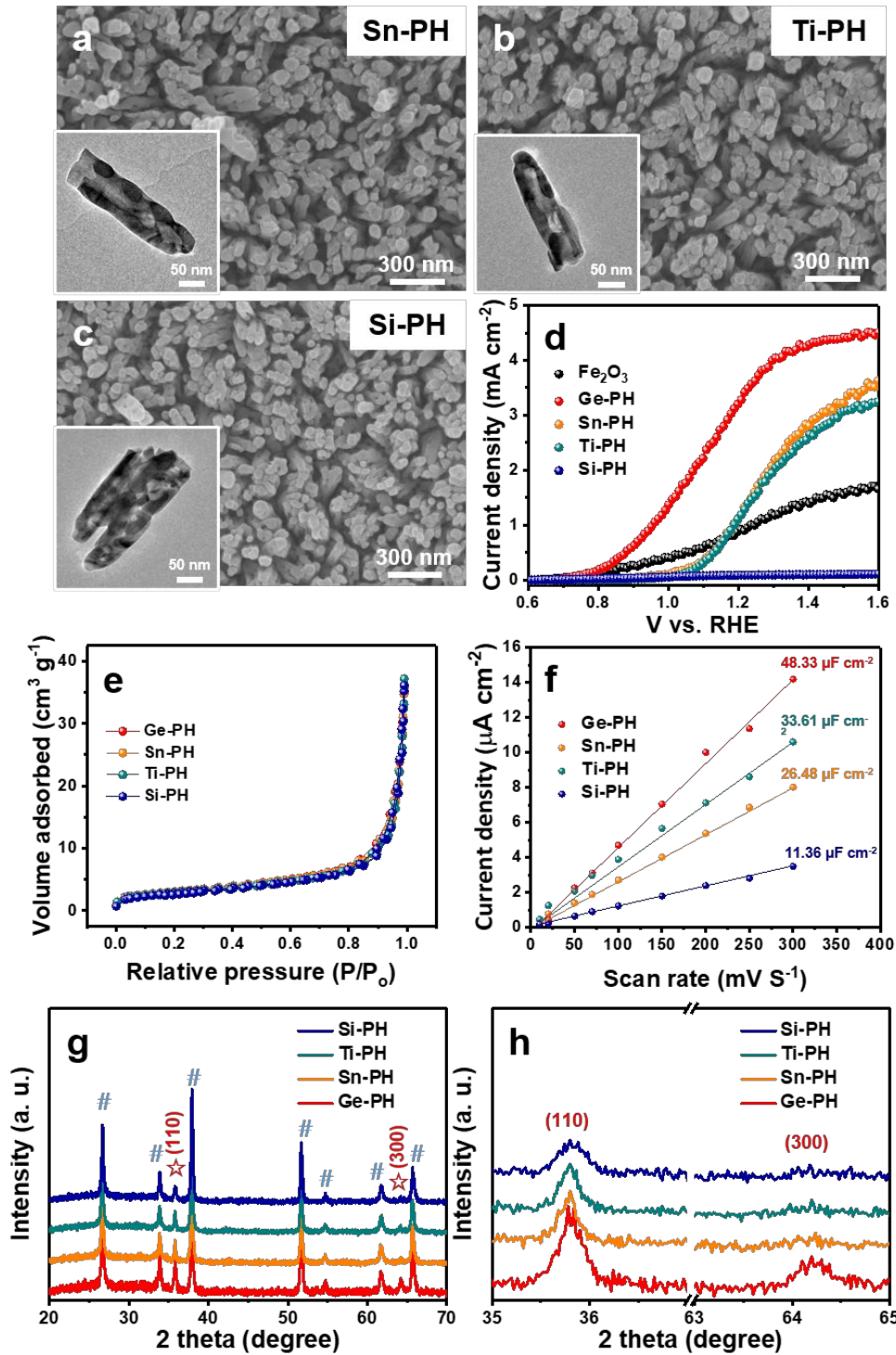


Figure 4.5. SEM and TEM images of porous hematites with (a) Sn, (b) Ti, and (c) Si doping. (d) PEC efficiency for various doped porous hematites and (e) N₂ adsorption-desorption isotherms of each sample. The BET surface area of each sample is around 10 m²/g. (f) The ECSA values of each photoanode. (g) XRD patterns of each sample and (h) the zoom-in image of XRD patterns for (110) and (300) plane.

XRD patterns showed that all three samples were well made of hematite with no other phase material formed as confirmed in Figure 4.4b. In Raman spectra, the LO signal of Ge-H was much sharper than that of Fe₂O₃ and Ge-PH as shown in Figure 4.4c. This means that Ge-H has many asymmetrically formed crystals inside hematite. XPS peaks of Ge 3d and Sn 3d can confirm that Ge and Sn are doped in hematite. In the spectrum of Ge 3d (Figure 4.4d), Ge 3d peaks at around 31.6 eV in Ge-H and Ge-PH showed that the Ge dopants were well doped into hematite as shown in Figure 4.4d. Ge-PH showed higher doping level than that of Ge-H and When the peaks were deconvoluted it was also confirmed that more Ge⁴⁺ existed in Ge-PH as shown in Figure 4.6. Ge-H. The optimization of the Ge doping level of Ge-H was achieved at a lower doping level than that of Ge-PH, confirming that the photocurrent density decreased when the doping level of Ge-H was further increased as shown in Figure 4.7. The Sn 3d peaks at 494.7 (Sn 3d_{3/2}) and 486.2 eV (Sn 3d_{5/2}) indicated that Sn dopants were well doped into hematite as shown in Figure 4.4e. As seen in the Sn 3d spectra, Ge-PH showed very little Sn doping level compared to Fe₂O₃ and Ge-H. This was because diffusion of Sn into hematite was suppressed by the overlayer as described in chapter 3. Therefore, it could be expected that the proportion of Ge and Sn mixed in Ge-PH would be less than that of Ge-H. We conducted extended X-ray absorption fine structure (EXAFS) measurements to demonstrate in order to confirm that if the amount of Sn is large, it adversely affects hematite. The oxidation state of each material was confirmed through X-ray absorption near edge structure (XANES) analysis as seen in Figure 4.8. The difference in R space in EXAFS clearly showed the difference with each doping as shown in Figure 4.4f. The intensity of signals indicates the degree of crystallinity, and Ge-PH showed an intensity almost similar to that of pristine Fe₂O₃, whereas Ge-H showed a lower intensity than that of pristine Fe₂O₃ or Ge-PH. Fe–O bonds and Fe–Fe bonds were assigned at 1.5 Å and 3 Å, respectively. Ge-H has the largest R space in Fe–O signals, meaning that it formed the low oxidation state (Fe²⁺) rather than Fe³⁺ compared to pristine Fe₂O₃ or Ge-PH. In order to more intuitively observe the results for the Ge and Sn ratio, XPS depth profile was performed. The Sn/Fe ratio of Fe₂O₃ and Ge-H was similar between about 5-10% over the entire range. However, the Ge/Sn ratio of Ge-PH was very small, less than 1% in the entire range as shown in Figure 4.4g. The Ge/Fe ratios of Ge-H and Ge-PH were 3.4-5.5% and 7.7-13.8%, respectively, as shown in Figure 4.4h. Ge-H and Ge-PH have similar total doping levels of Ge and Sn as shown in Figure 4.9, but It was confirmed that the Ge/Sn ratio of Ge-H is about 14-19 times higher than that of Ge-PH in entire range as shown in Figure 4.4i. Therefore, the interaction of Ge and Sn adversely affects hematite. To verify this, we compared the efficiency of the hematite electrode heat treated at a low temperature where Sn does not diffuse from the FTO substrate. Sn can definitely help to improve the efficiency of hematite, but it has been confirmed that it interferes with maximizing the doping efficiency of Ge, which is a better dopant than Sn (Figure 4.10).

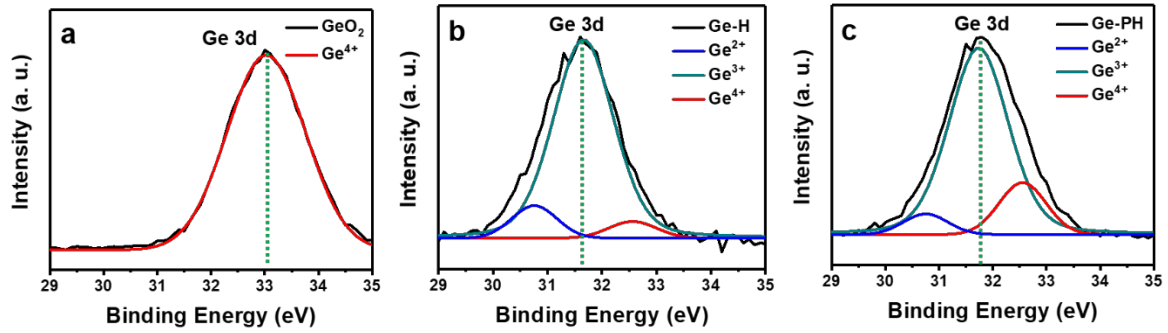


Figure 4.6. XPS spectra of Ge 3d for (a) GeO₂, (b) Ge-H and (c) Ge-PH.

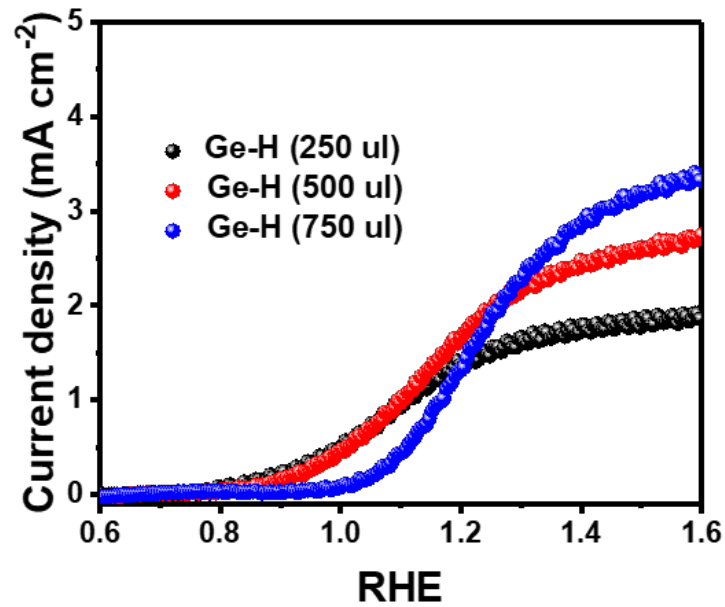


Figure 4.7. The photoelectrochemical performance of Ge-H according to the amount of different Ge precursors in 100 ml of 150 mM FeCl₃.

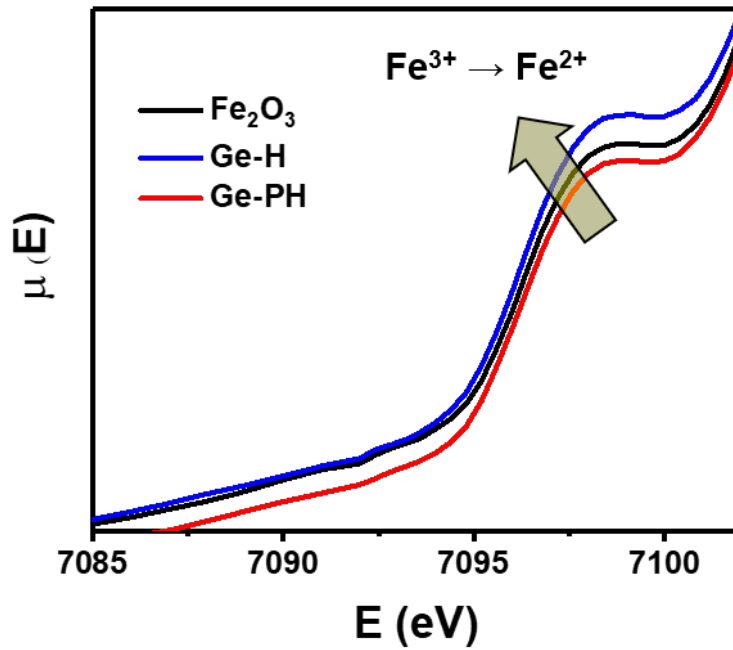


Figure 4.8. XANES spectra of Fe₂O₃, Ge-H and Ge-PH.

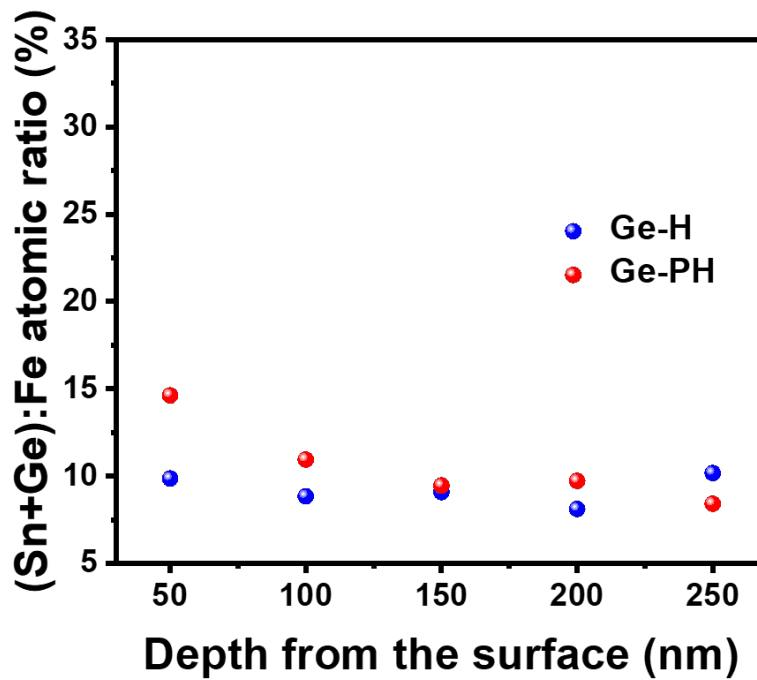


Figure 4.9. Calculated (Sn+Ge)/Fe ratio by XPS depth profiles

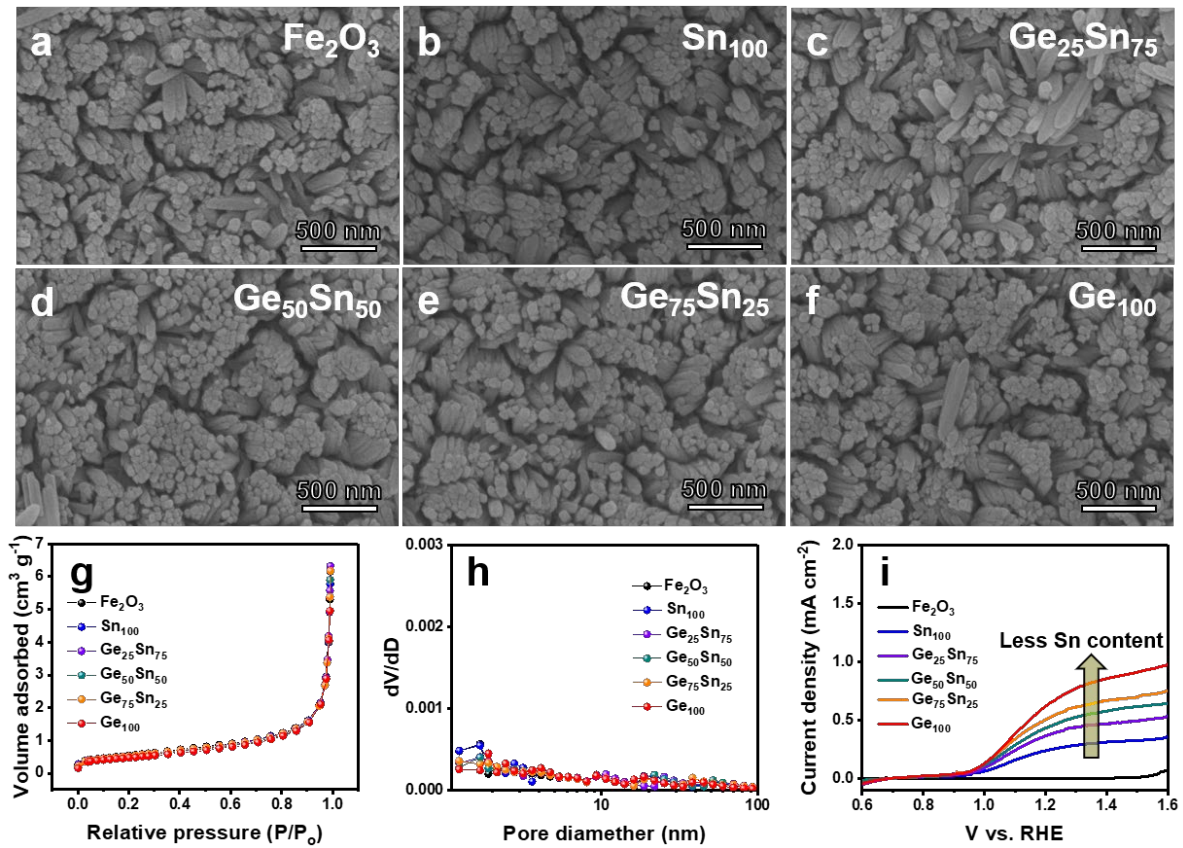


Figure 4.10. SEM images of (a) Fe_2O_3 , (b) Sn_{100} ($\text{Ge}_0\text{:Sn}_{100}$ -hematite), (c) $\text{Ge}_{25}\text{Sn}_{75}$ ($\text{Ge}_{25}\text{:Sn}_{75}$ -hematite), (d) $\text{Ge}_{50}\text{Sn}_{50}$ ($\text{Ge}_{50}\text{:Sn}_{50}$ -hematite), (e) $\text{Ge}_{75}\text{Sn}_{25}$ ($\text{Ge}_{75}\text{:Sn}_{25}$ -hematite), (f) Ge_{100} ($\text{Ge}_0\text{:Sn}_{100}$ -hematite). (g) N_2 adsorption-desorption isotherms of each sample. The BET surface area of each sample is around $2 \text{ m}^2/\text{g}$. (h) The pore size distribution in Fe_2O_3 , Ge-H, and Ge-PH. (i) J-V curves of Sn-doped, Ge-doped, and Ge:Sn co-doped hematite prepared at low temperature ($550 \text{ }^\circ\text{C}$).

We also observed the interaction of Ge with Sn through DFT calculations. It was confirmed that the formation energy of Ge doping was lower than that of Sn doping, and when Ge and Sn were co-doped, the formation energy was slightly higher than that of Sn. Therefore, Ge is superior to Sn dopant, but it means that doping becomes difficult when Ge and Sn exist together as shown in Figure 4.11a. Differences in atomic arrangement were also observed. When Ge was doped into hematite, the atomic arrangement was almost identical to that of pristine Fe_2O_3 , whereas when Ge and Sn were coexisted, one Fe atom was displaced as shown in Figure 4.11b. This was consistent with the result that Ge-H has many asymmetric structures in the Raman spectrum. Figure 4.11c explains why the interaction of Ge and Sn adversely affects the hematite structure. Ge has a similar size to that of Fe. After Ge doping, only one Fe is changed to Fe^{2+} by doping. In the case of the Sn doping, Since Sn has a larger size than Fe, Fe^{2+} that changes due to lattice strain occurs along with the formation of Fe^{2+} by doping. This is one of the reasons why Ge can achieve better efficiency than Sn. when Ge and Sn are co-doped, Fe^{2+} generated by the charge repulsion between Ge and Sn increases along with the lattice strain caused by the size of Sn. For this reason, the co-doping of Ge and Sn adversely affects the structure of hematite, causes high formation energy, and consequently affects the PEC efficiency. In XPS spectra for Fe 2p, Ge-H was directly observed to have more Fe^{2+} than Ge-PH as shown in Figure 4.11d. Therefore, when using a dopant with better performance than Sn, doping using an overlayer can be an efficient method as shown in Figure 4.11e. Experiments on electrochemical behavior were also confirmed. In Mott-Schottky plots (Figure 4.12a), Ge-PH showed the lowest slope, and the depletion layer calculated through Mott-Schottky plots was also confirmed to have the shortest Ge-PH as shown in Table 4.1. A shorter depletion layer means sharper band bending and less recombination probability. The Nyquist plots was performed to confirm the interfacial behavior between electrolyte and active material. The second semicircle, R_{ct} value, represents the resistance between the electrolyte and the active material. It was observed that the R_{ct} value of Ge-PH was significantly reduced compared to the R_{ct} value of Fe_2O_3 or Ge-H. The first semicircle, R_{trap} , is the resistance across the active substance. Ge-PH also showed the smallest R_{trap} value as shown in Figure 4.12b. The calculated free energy involved in the OER reaction can be seen in Figure 4.12c. In general, the step with the greatest resistance in the hematite based OER is reaction B ($*\text{OH} \rightarrow *\text{O}$). Therefore, it can be observed that pristine Fe_2O_3 takes the greatest resistance in reaction B with overpotential of 1.007 eV. Interestingly, in Ge-doped hematite, it was confirmed that the step with the greatest resistance changed from reaction B to reaction C. This is because doped Ge stabilizes unstable $*\text{O}$ in reaction B by donating electrons to oxygen. Therefore, since reaction B and reaction C have a trade-off relationship with each other, as reaction C increases as much as reaction B is decreased, reaction C step takes the greatest resistance. However, it was confirmed that the overpotential of the entire reaction (0.888 eV) was reduced compared to that of pristine Fe_2O_3 .

Finally, the charge separation efficiency was calculated using a hole scavenger, Na_2SO_3 as shown in Figure 4.12d. Ge-PH showed higher charge separation efficiency than Fe_2O_3 and Ge-H in the entire range and maintained charge separation efficiency of about 80% or more after $1.3V_{\text{RHE}}$. Finally, a tandem device was manufactured using Ge-PH and PSC. For tandem device, we employed a PSC fabricated using a recently developed procedure (short-circuit current (J_{sc}) = 21.60 mA cm^{-2} , open-circuit voltage (V_{oc}) = 1.16 V, and fill factor (FF) = 75.07%; power conversion efficiency (PCE) = 18.85%, Figure 4.14). The tandem system of Hematite and PSC has been reported as a system capable of producing hydrogen without an external applied voltage as shown in Figure 4.13a. Ge-PH not only has excellent PEC efficiency but is also useful for tandem system since it has a higher transmittance than Fe_2O_3 or Ge-H due to its porous structure as shown in Figure 4.15. To maximize the efficiency of the tandem system, NiFeO_x co-catalyst was loaded on the surface of Ge-PH. After loading NiFeO_x co-catalyst, our final photoanode ($\text{NiFeO}_x/\text{Ge-PH}$) showed a photocurrent density of around 4.6 mA cm^{-2} at $1.23 V_{\text{RHE}}$ as shown in Figure 4.13b. As for the operating point of the tandem device, it can be observed from the figure that the LSV of PSC and the LSV of $\text{NiFeO}_x/\text{Ge-PH}$ formed a photocurrent density of 3.9 mA cm^{-2} , which was the overlapping part as shown in Figure 4.13c. The tandem device was also confirmed to work stably for about 5 hours as shown in Figure 4.13d. Finally, we measured the Faradaic efficiency through the oxygen and hydrogen generated by the tandem device. Oxygen is generated on the surface of $\text{NiFeO}_x/\text{Ge-PH}$, and hydrogen is generated from platinum connected to PSC. The measured amounts of hydrogen and oxygen were around 68.5 and 34.0 μmol after 120 min, respectively. This means that according to the water splitting mechanism, the gases were well generated in a 2:1 ratio. Most of the holes and electrons generated by light are used only for water splitting while maintaining the efficiency of over 90% in our tandem system. To the best of our knowledge, our studies showed the highest PEC performance achieved for the hematite-based tandem device, as shown in Table 4.2.

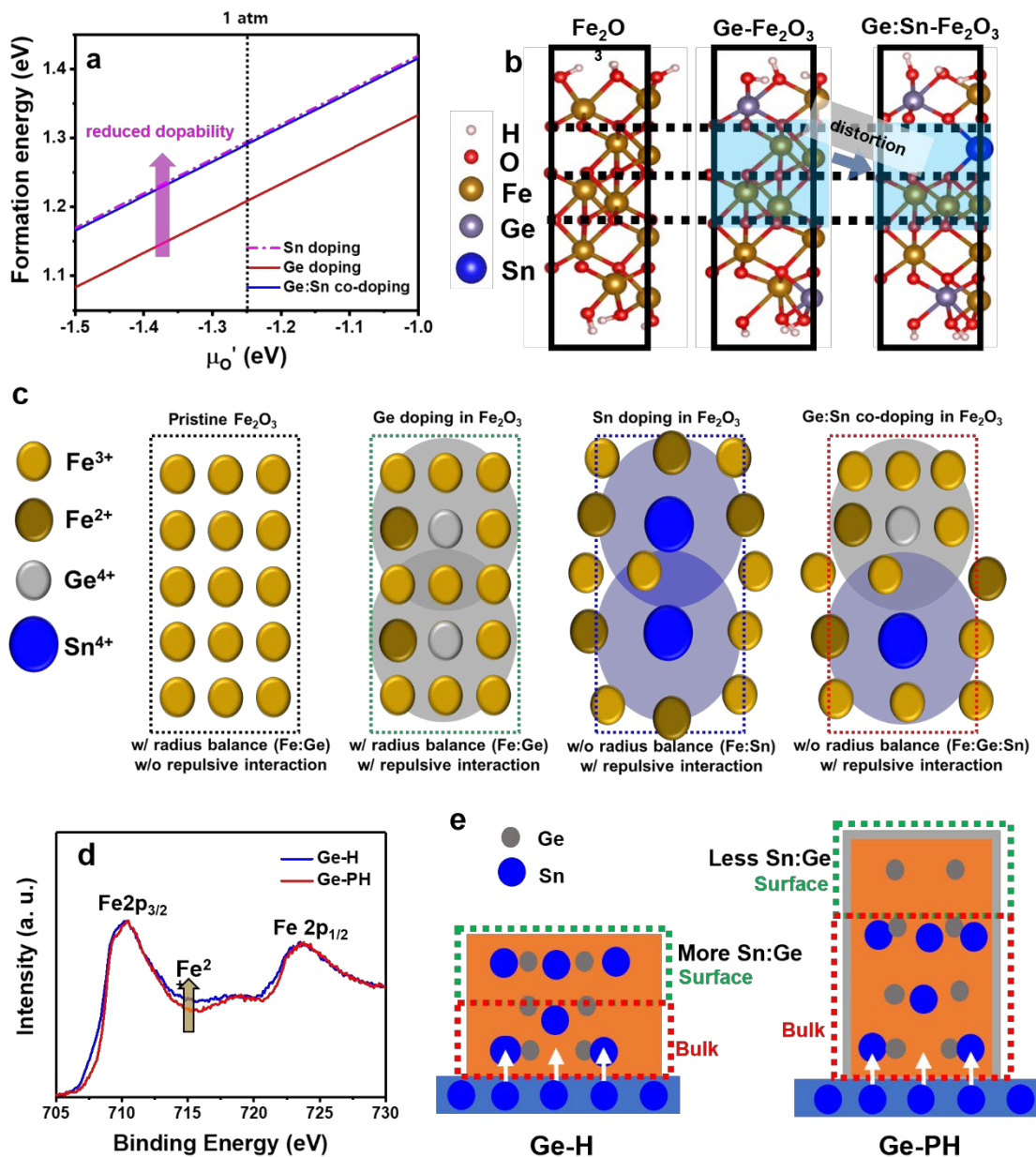


Figure 4.11. (a) Calculated formation energies of various dopants (Sn, Ge, and co-doped Ge and Sn) into hematite. The dotted line is the energy standard that matches the experimental conditions. (b) atomic structures of Fe_2O_3 , Ge doped Fe_2O_3 , and Ge and Sn co-doped Fe_2O_3 , by DFT calculations. (c) Atomic arrangements of ideal Fe_2O_3 , Ge doped Fe_2O_3 , Sn doped Fe_2O_3 and Ge and Sn co-doped Fe_2O_3 . (d) Fe 2p signals by XPS measurement. (e) The process of Sn doping from FTO and the mechanism by which Ge and Sn exist together.

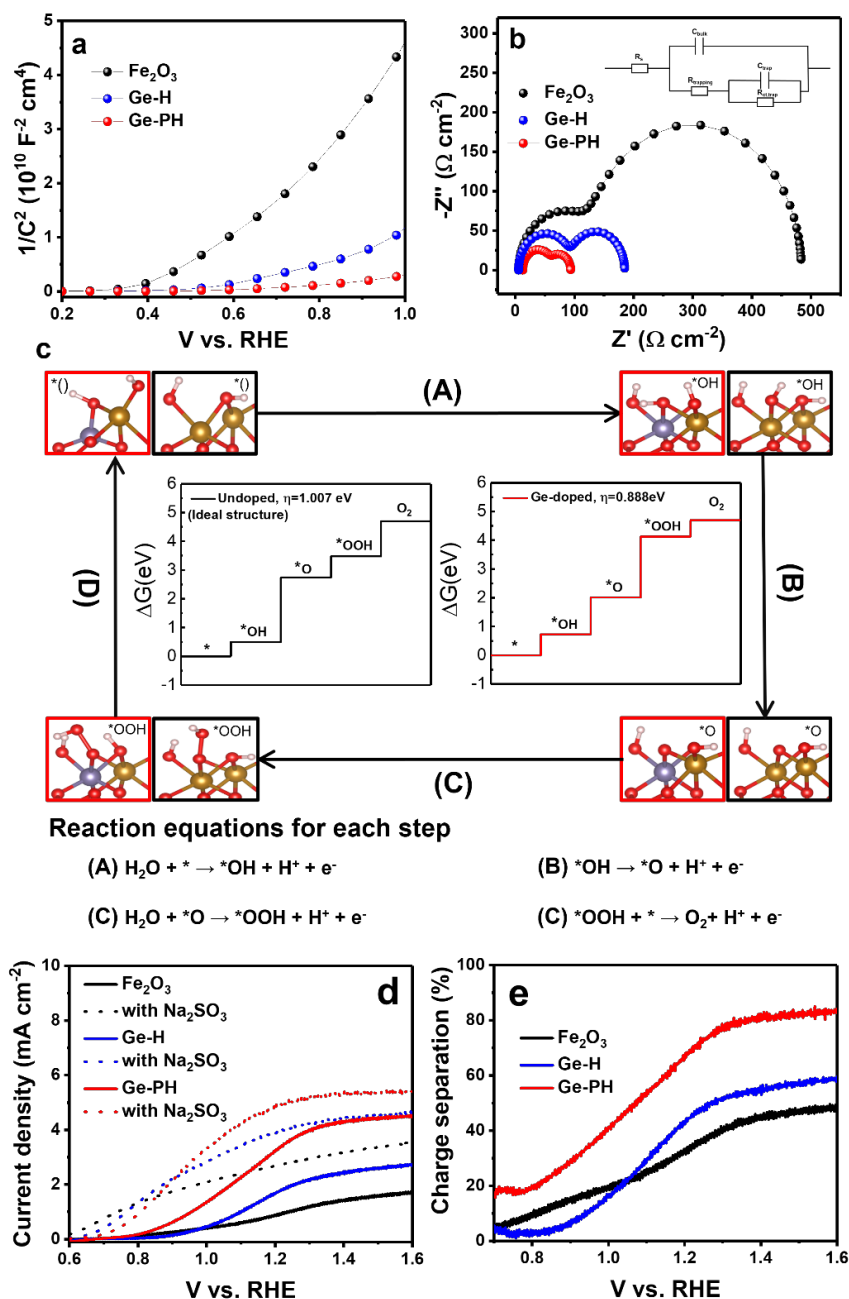


Figure 4.12. (a) Mott-Schottky measurements of Fe_2O_3 , Ge doped Fe_2O_3 and Ge and Sn co-doped Fe_2O_3 . and (b) Nyquist plot. inset image is the circuit model. (c) Free energy diagrams of the intermediates on ideal Fe_2O_3 and ideal Ge doped Fe_2O_3 . Hematite (0001) surface was used for accurate comparison with the existing literature. Brown, gray, red, and white are Fe, Ge, O, and H atoms, respectively. (d) PEC efficiency of Fe_2O_3 , Ge-H, and Ge-PH with hole scavenger, .5 M Na_2SO_3 , (dashed lines) and without hole scavenger (solid lines) in basic electrolyte (1 M NaOH). (e) Calculated charge separation efficiencies by LSV curve w/w/o hole scavenger.

	E_{FB} (V)	N_{D} (10^{20}cm^{-3})	W (nm)
Fe ₂ O ₃	0.39	0.22	12.4
Ge-H	0.53	0.70	6.26
Ge-PH	0.43	3.10	2.97

Table 4.1. Calculated results from Mott-Schottky plots for the flat band potential (E_{FB}), charge carrier concentration (N_{D}), and space charge width (W_{sc}).

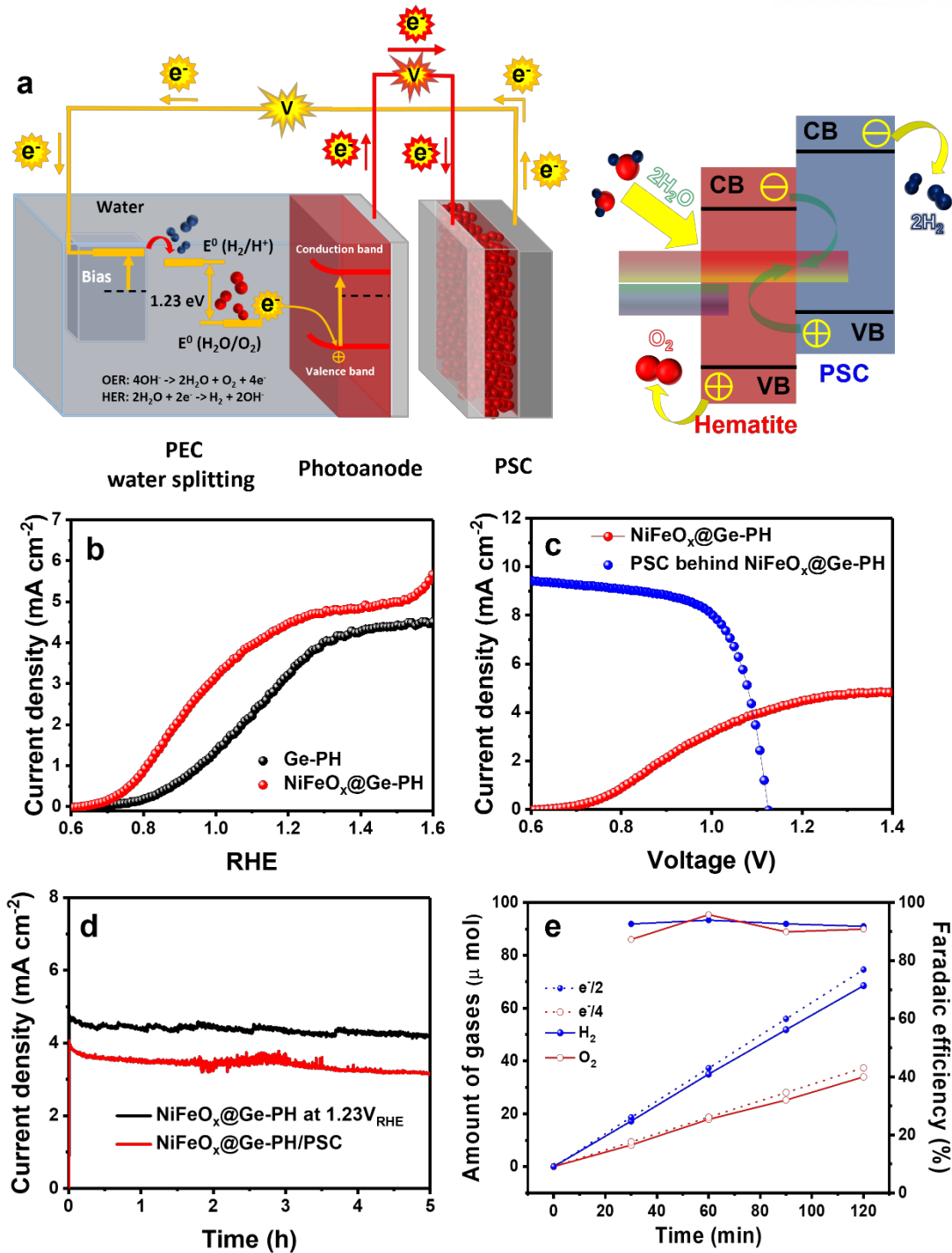


Figure 4.13. (a) Schematic images of the working principle of a tandem device composed of hematite photoanode and PSC. (b) LSV curves of Ge-PH w/wo $NiFeO_x$. (c) LSV curves of PSC behind photoanode and our final photoanode ($NiFeO_x@Ge-PH$). (d) Long-term stability test of our final photoanode ($NiFeO_x@Ge-PH$) at $1.23V_{RHE}$ and tandem device for solar water splitting. (e) Gases measurements for calculating Faradaic efficiency of the $NiFeO_x@Ge-PH$.

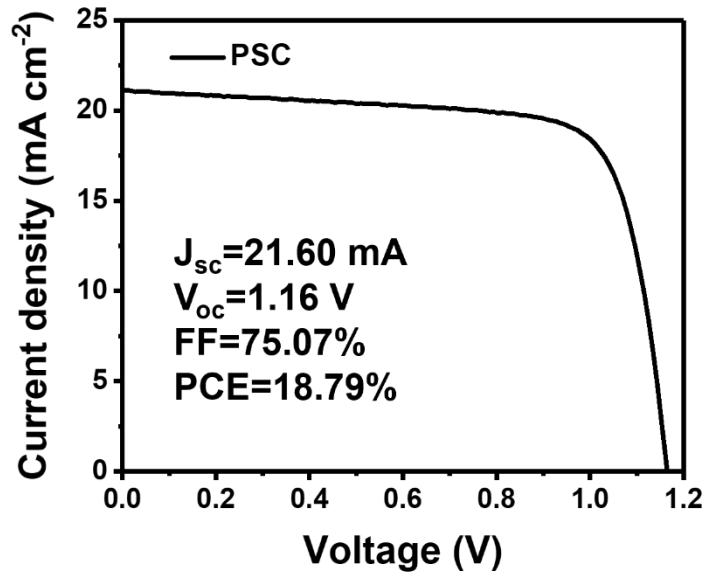


Figure 4.14. LSV curves of PSC under 1 SUN illumination.

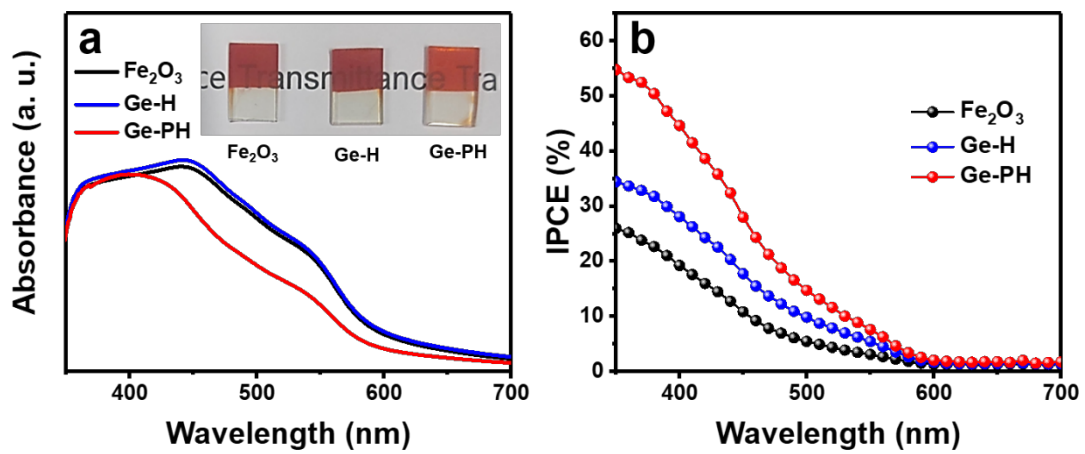


Figure 4.15. (a) UV-Vis and (b) IPCE spectra of Fe₂O₃, Ge-H and Ge-PH.

Photoanode	Measurement condition	Photocurrent density ($1.23V_{RHE}$)	In tandem with	J_{op}	STH conversion efficiency	Reference
NiFeO _x /Fe ₂ O ₃	Phosphate buffered solution (pH=11.8), 100 mW/cm ²	~1.40 mA/cm ²	a-Si:H/TiO ₂ /Pt	~0.74 mA/cm ²	~0.9%	Nat. Commun. (2015) ³⁰
TiO ₂ /Co-Fe ₂ O ₃	0.5 M Na ₂ CO ₃ (pH=11.2), 100 mW/cm ²	~3.04 mA/cm ²	PSC	~0.50 mA/cm ²	~0.6%	RSC Adv. (2018) ³¹
FeNiO _x /Al ₂ O ₃ /Si-Fe ₂ O ₃	1 M KOH (pH=13.6), 100 mW/cm ²	~2.75 mA/cm ²	PSC	~1.54 mA/cm ²	~1.9%	J. Am. Chem. Soc. (2015) ³²
Co-Pi/Mn-Fe ₂ O ₃	1 M NaOH (pH=13.6), 100 mW/cm ²	~3.50 mA/cm ²	PSC	~1.93 mA/cm ²	~2.4%	Nano Lett. (2015) ³³
Co-Pi/Sn-Fe ₂ O ₃	1 M NaOH (pH=13.6), 100 mW/cm ²	~3.90 mA/cm ²	PSC	~2.80 mA/cm ²	~3.4%	ChemSusChem. (2017) ³⁴
FeNiOOH/Fe ₂ TiO ₅ /Fe ₂ O ₃ /ITO	1 M NaOH (pH=13.6), 100 mW/cm ²	~2.20 mA/cm ²	a-Si:H/ μ c-Si:H/ μ c-Si:H	~1.10 mA/cm ²	~1.4%	ChemSusChem. (2019) ³⁵
NiFeO _x /Ti:Si-Fe ₂ O ₃ (Dual photoanode)	1 M NaOH (pH=13.6), 100 mW/cm ²	~4.00 mA/cm ²	PSC	~3.65 mA/cm ²	~4.5%	Nano Energy (2020) ¹⁶
NiFeO_x/Ge-PH	1 M NaOH (pH=13.6), 100 mW/cm²	~4.60 mA/cm²	PSC	~3.90 mA/cm²	~4.8%	This work

Table 4.2. Recent reports on hematite-based tandem systems.

4.4 Conclusion

In summary, we have proven the superiority of Ge dopant by GeO₂ overlayer. Manufacture of hematite using GeO₂ overlayer is advantageous for the PEC system by creating a porous structure, but also suppresses Sn doping from the FTO substrate, thereby maximizing the Ge doping efficiency. It has been demonstrated through Raman, EXAFS, DFT calculations, and electrochemical behavior that the crystallinity of hematite decreased as the Ge/Sn ratio increased. In addition, by confirming that Ge-doped hematite can form superior OER kinetics compared to pristine hematite through DFT calculations, it has been verified that the Ge-PH electrode can produce excellent PEC efficiency. Therefore, it was found that suppressing Sn doping from the substrate as much as possible can help to improve the efficiency of dopants that can produce better doping efficiency than Sn. Through in-sight for Ge doping, our tandem device using PSC could achieve a photocurrent density of $\sim 3.9 \text{ mA cm}^{-2}$ in basic electrolyte (1 M NaOH). Our research breaks the conventional notion of Sn doping and suggests more diverse doping designs and efficient doping methods, and at the same time can be utilized in various doping systems in various applications using solar energy conversion.

4.5 References

- (1) Li, C.; Li, A.; Luo, Z.; Zhang, J.; Chang, X.; Huang, Z.; Wang, T.; Gong, J. Surviving High-Temperature Calcination: ZrO₂-Induced Hematite Nanotubes for Photoelectrochemical Water Oxidation. *Angew. Chemie Int. Ed.* **2017**, *56* (15), 4150–4155. <https://doi.org/https://doi.org/10.1002/anie.201611330>.
- (2) Yoon, K.-Y.; Park, J.; Lee, H.; Seo, J. H.; Kwak, M.-J.; Lee, J. H.; Jang, J.-H. Unveiling the Role of the Ti Dopant and Viable Si Doping of Hematite for Practically Efficient Solar Water Splitting. *ACS Catal.* **2022**, *12* (9), 5112–5122. <https://doi.org/10.1021/acscatal.1c05106>.
- (3) Liao, P.; Toroker, M. C.; Carter, E. A. Electron Transport in Pure and Doped Hematite. *Nano Lett.* **2011**, *11* (4), 1775–1781. <https://doi.org/10.1021/nl200356n>.
- (4) Seo, J. H.; Choi, K.; Nam, J.; Lee, H.; Lee, J. H. Synergetic Donor–Donor Codoping Strategy for Enhanced Photoelectrochemical Activity of Hematite. *Appl. Catal. B Environ.* **2020**, *260*, 118186. <https://doi.org/https://doi.org/10.1016/j.apcatb.2019.118186>.
- (5) Hufnagel, A. G.; Hajiyani, H.; Zhang, S.; Li, T.; Kasian, O.; Gault, B.; Breitbach, B.; Bein, T.; Fattakhova-Rohlfing, D.; Scheu, C.; Pentcheva, R. Why Tin-Doping Enhances the Efficiency of Hematite Photoanodes for Water Splitting—The Full Picture. *Adv. Funct. Mater.* **2018**, *28* (52), 1804472. <https://doi.org/https://doi.org/10.1002/adfm.201804472>.
- (6) Pan, H.; Meng, X.; Liu, D.; Li, S.; Qin, G. (Ti/Zr,N) Codoped Hematite for Enhancing the Photoelectrochemical Activity of Water Splitting. *Phys. Chem. Chem. Phys.* **2015**, *17* (34), 22179–22186. <https://doi.org/10.1039/C5CP01489A>.
- (7) Zhou, Z.; Huo, P.; Guo, L.; Prezhdo, O. V. Understanding Hematite Doping with Group IV Elements: A DFT+U Study. *J. Phys. Chem. C* **2015**, *119* (47), 26303–26310. <https://doi.org/10.1021/acs.jpcc.5b08081>.
- (8) Ling, Y.; Wang, G.; Wheeler, D. A.; Zhang, J. Z.; Li, Y. Sn-Doped Hematite Nanostructures for Photoelectrochemical Water Splitting. *Nano Lett.* **2011**, *11* (5), 2119–2125. <https://doi.org/10.1021/nl200708y>.
- (9) Hahn, N. T.; Mullins, C. B. Photoelectrochemical Performance of Nanostructured Ti- and Sn-Doped α -Fe₂O₃ Photoanodes. *Chem. Mater.* **2010**, *22* (23), 6474–6482. <https://doi.org/10.1021/cm1026078>.
- (10) Zhou, Z.; Wu, S.; Qin, L.; Li, L.; Li, L.; Li, X. Modulating Oxygen Vacancies in Sn-Doped Hematite Film Grown on Silicon Microwires for Photoelectrochemical Water Oxidation. *J. Mater. Chem. A* **2018**, *6* (32), 15593–15602. <https://doi.org/10.1039/C8TA03643H>.
- (11) Park, J. W.; Mahadik, M. A.; Ma, H.; An, G. W.; Lee, H. H.; Choi, S. H.; Chae, W.-S.; Chung, H.-S.; Jang, J. S. Improved Interfacial Charge Transfer Dynamics and Onset Shift in Nanostructured Hematite Photoanodes via Efficient Ti⁴⁺/Sn⁴⁺ Heterogeneous Self-Doping Through Controlled TiO₂ Underlayers. *ACS Sustain. Chem. Eng.* **2019**, *7* (7), 6947–6958. <https://doi.org/10.1021/acssuschemeng.8b06544>.
- (12) Dunn, H. K.; Feckl, J. M.; Müller, A.; Fattakhova-Rohlfing, D.; Morehead, S. G.; Roos, J.; Peter, L. M.; Scheu, C.; Bein, T. Tin Doping Speeds up Hole Transfer during Light-Driven Water Oxidation at Hematite Photoanodes. *Phys. Chem. Chem. Phys.* **2014**, *16* (44), 24610–24620. <https://doi.org/10.1039/C4CP03946G>.
- (13) Cesar, I.; Sivula, K.; Kay, A.; Zboril, R.; Grätzel, M. Influence of Feature Size, Film

- Thickness, and Silicon Doping on the Performance of Nanostructured Hematite Photoanodes for Solar Water Splitting. *J. Phys. Chem. C* **2009**, *113* (2), 772–782. <https://doi.org/10.1021/jp809060p>.
- (14) Cesar, I.; Kay, A.; Gonzalez Martinez, J. A.; Grätzel, M. Translucent Thin Film Fe₂O₃ Photoanodes for Efficient Water Splitting by Sunlight: Nanostructure-Directing Effect of Si-Doping. *J. Am. Chem. Soc.* **2006**, *128* (14), 4582–4583. <https://doi.org/10.1021/ja060292p>.
- (15) Zhou, Z.; Long, R.; Prezhdo, O. V. Why Silicon Doping Accelerates Electron Polaron Diffusion in Hematite. *J. Am. Chem. Soc.* **2019**, *141* (51), 20222–20233. <https://doi.org/10.1021/jacs.9b10109>.
- (16) Park, J.; Yoon, K.-Y.; Kim, T.; Jang, H.; Kwak, M.-J.; Kim, J. Y.; Jang, J.-H. A Highly Transparent Thin Film Hematite with Multi-Element Dopability for an Efficient Unassisted Water Splitting System. *Nano Energy* **2020**, *76*, 105089. <https://doi.org/10.1016/j.nanoen.2020.105089>.
- (17) Fu, Z.; Jiang, T.; Zhang, L.; Liu, B.; Wang, D.; Wang, L.; Xie, T. Surface Treatment with Al³⁺ on a Ti-Doped α -Fe₂O₃ Nanorod Array Photoanode for Efficient Photoelectrochemical Water Splitting. *J. Mater. Chem. A* **2014**, *2* (33), 13705–13712. <https://doi.org/10.1039/C4TA02527J>.
- (18) Shen, S.; Kronawitter, C. X.; Wheeler, D. A.; Guo, P.; Lindley, S. A.; Jiang, J.; Zhang, J. Z.; Guo, L.; Mao, S. S. Physical and Photoelectrochemical Characterization of Ti-Doped Hematite Photoanodes Prepared by Solution Growth. *J. Mater. Chem. A* **2013**, *1* (46), 14498–14506. <https://doi.org/10.1039/C3TA13453A>.
- (19) Yoon, K.-Y.; Ahn, H.-J.; Kwak, M.-J.; Kim, S.-I.; Park, J.; Jang, J.-H. A Selectively Decorated Ti-FeOOH Co-Catalyst for a Highly Efficient Porous Hematite-Based Water Splitting System. *J. Mater. Chem. A* **2016**, *4* (48), 18730–18736. <https://doi.org/10.1039/C6TA08273D>.
- (20) Li, M.; Qiu, Y.; Qiu, W.; Tang, S.; Xiao, S.; Ma, S.; Ouyang, G.; Tong, Y.; Yang, S. Boosting the Photoelectrochemical Water Oxidation at Hematite Photoanode by Innovating a Hierarchical Ball-on-Wire-Array Structure. *ACS Appl. Energy Mater.* **2018**, *1* (11), 5836–5841. <https://doi.org/10.1021/acsaem.8b01266>.
- (21) Tang, S.; Li, M.; Huang, D.; Qiu, W.; Xiao, S.; Tong, Y.; Yang, S. 3D Hierarchical Nanorod@Nanobowl Array Photoanode with a Tunable Light-Trapping Cutoff and Bottom-Selective Field Enhancement for Efficient Solar Water Splitting. *Small* **2019**, *15* (14), 1804976. <https://doi.org/10.1002/sml.201804976>.
- (22) Annamalai, A.; Subramanian, A.; Kang, U.; Park, H.; Choi, S. H.; Jang, J. S. Activation of Hematite Photoanodes for Solar Water Splitting: Effect of FTO Deformation. *J. Phys. Chem. C* **2015**, *119* (7), 3810–3817. <https://doi.org/10.1021/jp512189c>.
- (23) Kresse, G.; Joubert, D. From Ultrasoft Pseudopotentials to the Projector Augmented-Wave Method. *Phys. Rev. B* **1999**, *59* (3), 1758–1775. <https://doi.org/10.1103/PhysRevB.59.1758>.
- (24) Kresse, G.; Furthmüller, J. Efficient Iterative Schemes for Ab Initio Total-Energy Calculations Using a Plane-Wave Basis Set. *Phys. Rev. B* **1996**, *54* (16), 11169–11186. <https://doi.org/10.1103/PhysRevB.54.11169>.
- (25) Perdew, J. P.; Burke, K.; Ernzerhof, M. Generalized Gradient Approximation Made Simple. *Phys. Rev. Lett.* **1996**, *77* (18), 3865–3868. <https://doi.org/10.1103/PhysRevLett.77.3865>.
- (26) Wang, L.; Maxisch, T.; Ceder, G. Oxidation Energies of Transition Metal Oxides within the

- Γ -GGA+U Framework. *Phys. Rev. B* **2006**, *73* (19), 195107. <https://doi.org/10.1103/PhysRevB.73.195107>.
- (27) Finger, L. W.; Hazen, R. M. Crystal Structure and Isothermal Compression of Fe₂O₃, Cr₂O₃, and V₂O₃ to 50 Kbars. *J. Appl. Phys.* **1980**, *51* (10), 5362–5367. <https://doi.org/10.1063/1.327451>.
- (28) Sharma, P.; Jang, J.-W.; Lee, J. S. Key Strategies to Advance the Photoelectrochemical Water Splitting Performance of α -Fe₂O₃ Photoanode. *ChemCatChem* **2019**, *11* (1), 157–179. <https://doi.org/10.1002/cctc.201801187>.
- (29) Zhang, H.; Li, D.; Byun, W. J.; Wang, X.; Shin, T. J.; Jeong, H. Y.; Han, H.; Li, C.; Lee, J. S. Gradient Tantalum-Doped Hematite Homo Junction Photoanode Improves Both Photocurrents and Turn-on Voltage for Solar Water Splitting. *Nat. Commun.* **2020**, *11* (1), 4622. <https://doi.org/10.1038/s41467-020-18484-8>.
- (30) Jang, J.-W.; Du, C.; Ye, Y.; Lin, Y.; Yao, X.; Thorne, J.; Liu, E.; McMahon, G.; Zhu, J.; Javey, A.; Guo, J.; Wang, D. Enabling Unassisted Solar Water Splitting by Iron Oxide and Silicon. *Nat. Commun.* **2015**, *6* (1), 7447. <https://doi.org/10.1038/ncomms8447>.
- (31) Roy, S.; Botte, G. G. Perovskite Solar Cell for Photocatalytic Water Splitting with a TiO₂/Co-Doped Hematite Electron Transport Bilayer. *RSC Adv.* **2018**, *8* (10), 5388–5394. <https://doi.org/10.1039/C7RA11996H>.
- (32) Morales-Guio, C. G.; Mayer, M. T.; Yella, A.; Tilley, S. D.; Grätzel, M.; Hu, X. An Optically Transparent Iron Nickel Oxide Catalyst for Solar Water Splitting. *J. Am. Chem. Soc.* **2015**, *137* (31), 9927–9936. <https://doi.org/10.1021/jacs.5b05544>.
- (33) Gurudayal; Sabba, D.; Kumar, M. H.; Wong, L. H.; Barber, J.; Grätzel, M.; Mathews, N. Perovskite–Hematite Tandem Cells for Efficient Overall Solar Driven Water Splitting. *Nano Lett.* **2015**, *15* (6), 3833–3839. <https://doi.org/10.1021/acs.nanolett.5b00616>.
- (34) Gurudayal; John, R. A.; Boix, P. P.; Yi, C.; Shi, C.; Scott, M. C.; Veldhuis, S. A.; Minor, A. M.; Zakeeruddin, S. M.; Wong, L. H.; Grätzel, M.; Mathews, N. Atomically Altered Hematite for Highly Efficient Perovskite Tandem Water-Splitting Devices. *ChemSusChem* **2017**, *10* (11), 2449–2456. <https://doi.org/10.1002/cssc.201700159>.
- (35) Urbain, F.; Tang, P.; Smirnov, V.; Welter, K.; Andreu, T.; Finger, F.; Arbiol, J.; Morante, J. R. Multilayered Hematite Nanowires with Thin-Film Silicon Photovoltaics in an All-Earth-Abundant Hybrid Tandem Device for Solar Water Splitting. *ChemSusChem* **2019**, *12* (7), 1428–1436. <https://doi.org/10.1002/cssc.201802845>.
- (36) Yoon, K.-Y.; Park, J.; Jung, M.; Ji, S.-G.; Lee, H.; Seo, J. H.; Kwak, M.-J.; Il Seok, S.; Lee, J. H.; Jang, J.-H. NiFeOx Decorated Ge-Hematite/Perovskite for an Efficient Water Splitting System. *Nat. Commun.* **2021**, *12* (1), 4309. <https://doi.org/10.1038/s41467-021-24428-7>.

Publication list

1. **K-Y Yoon**, J Park, MJ, H Lee, JH Seo, M-J Kwak, JH Lee, J-H Jang. Unveiling the role of the Ti dopant and viable Si doping of hematite for practically efficient solar water splitting. *ACS Catal.* 12:5112-5122 (2022), **selected as a cover.**
2. **K-Y Yoon**, J Park, MJ Jung, S-G Ji, H Lee, JH Seo, M-J Kwak, SI Seok, JH Lee, J-H Jang. NiFeOx decorated Ge-hematite/perovskite for an efficient water splitting system. *Nat. Commun.* 12:4309 (2021).
3. **K-Y Yoon**, H-J Ahn, M-J Kwak, S-I Kim, JH Park, J-H Jang. A selectively decorated Ti-FeOOH co-catalyst for a highly efficient porous hematite-based water splitting. *J. Mater. Chem. A.* 4:18730-18736 (2016).
4. **K-Y Yoon**, H-J Ahn, M-J Kwak, P. Thiagarajan, J-H Jang. Graphene Quantum Dot-Protected Cadmium Selenide Quantum Dot-Sensitized Photoanode for Efficient Photoelectrochemical Cells with Enhanced Stability and Performance. *Adv. Optical Mater.* 3:907-912 (2015).
5. **K-Y Yoon**, J-S Lee, KH Kim, C-H Baek, S-I Kim, J-B Kim, J-H Jang. Hematite-Based Photoelectrochemical Water Splitting Supported by Inverse Opal Structures of Graphene. *ACS Appl. Mater. Interfaces.* 6:22634-22639 (2014).
6. J Park, **K-Y Yoon**, M-J Kwak, J-E Lee, J Kang, J-H Jang. Sn-controlled co-doped hematite for efficient solar-assisted chargeable Zn-Air batteries. *ACS Appl. Mater. Interfaces.* 13:54906-54915 (2021).
7. J Park, **K-Y Yoon**, T Kim, H Jang, M-J Kwak, JY Kim, J-H Jang. A highly transparent thin film hematite with multi-element dopability for an efficient unassisted water splitting system. *Nano Energy.* 76:105089 (2020).
8. H-J Ahn, **K-Y Yoon**, M-J Kwak, JH Park, J-H Jang. Boron-doping of Metal-Doped Hematite for Reduced Surface Recombination in Water Splitting. *ACS Catal.* 8:11932-11939 (2018).
9. A. Ramadoss, **K-Y Yoon**, M-J Kwak, S-I Kim, S-T Ryu, J-H Jang. Fully flexible, lightweight, high performance all-solid-state supercapacitor based on 3-Dimensional-graphene/graphite-paper. *J. Power Sources.* 337:159-165 (2017).
10. H-J Ahn, **K-Y Yoon**, M-J Kwak, J-H Jang. Ti-doped SiO_x Passivation Layer for Greatly Enhanced Performance of Hematite Based Photoelectrochemical System. *Angew. Chem. Int. Ed.* 55:9922-9926 (2016).
11. H-J Ahn, **K-Y Yoon**, M-J Kwak, J-S Lee, P. Thiagarajan, J-H Jang. MoS_x supported hematite with enhanced photoelectrochemical performance. *J. Mater. Chem. A.* 3:21444-21450 (2015).
12. C Hwang, M-J Kwak, J Jeong, K Baek, **K-Y Yoon**, C An, J-W Min, J Kim, J Lee, SJ Kang, J-H Jang, H-K Song. Critical void dimension of carbon frameworks to accommodate insoluble products of lithium-oxygen batteries. *ACS Appl. Mater. Interfaces.* 14:492-501 (2022).
13. J Hwang, S-J Ha, A Ramadoss, **K-Y Yoon**, J-H Jang. Stacking-free porous graphene network for high capacitive performance. *ACS Appl. Energy Mater.* 3:4348-4355 (2020).
14. M-J Kwak, A. Ramadoss, **K-Y Yoon**, J-H Park, P. Thiagarajan, J-H Jang. Single-step Synthesis of N-doped Three-Dimensional Graphitic Foams for High Performance Supercapacitors. *ACS Sustainable Chem. Eng.* 5:6950-6957 (2017).
15. KH Kim, I-H Kim, **K-Y Yoon**, JY Lee, J-H Jang. α-Fe₂O₃ on Patterned Fluorine Doped Tin Oxide for Efficient Photoelectrochemical Water Splitting. *J. Mater. Chem. A.* 3:7706-7709 (2015).
16. H-J Ahn, M-J Kwak, J-S Lee, **K-Y Yoon**, J-H Jang. Nanoporous Hematite Structures to Overcome Short Diffusion Lengths in Water Splitting. *J. Mater. Chem. A.* 2:19999-20003 (2014).

Acknowledgment

먼저 박사과정 동안 부족한 저에게 많은 기회를 주시고, 가르침을 주신 장지현 교수님께 진심으로 감사드립니다. 또한 바쁘신 와중에도 귀중한 시간을 내어서 논문 심사에 참여해주신 석상일 교수님, 류정기 교수님, 이준희 교수님, 장지욱 교수님께도 감사의 말씀을 드립니다. 유니스트에서 박사학위를 하며 기쁜 일도 있었고 힘든 일도 있었지만 그럴 때마다 항상 같이 응원해줬던 졸업하신 선배님들 포함 우리 연구실 사람들, 이정수 교수님, 안효진 박사님, 김선이 박사님, 김성욱 박사님, 김광현 박사, 종철이형, 명준, 지훈, 경남, 성지, 주형, 진호, 민경이에게도 정말 감사하다고 전하고 싶습니다. 또한 공부를 할수록 점점 부족한 자신을 발견할 때마다 좌절하던 저에게 정말 많은 조언을 해 주셨던 송우진 교수님, 정민수 교수님, 황치현 박사님, 이호식 박사님에게도 감사드립니다. 유니스트에 2013 년에 대학원생으로 입학하여 2022 년 박사학위를 수여하기까지 9 년이라는 시간이 걸렸습니다. 어려운 시간들도 많았지만 하나씩 새로운 것을 배워가며 제가 꿈꿔왔던 연구하는 삶을 살아본 것이 지금 돌아보면 정말 행복한 시간이었던 것 같습니다. 무엇보다 제가 연구자로서 살아볼 수 있는 기회를 주시고 연구에 대한 가르침은 물론 나아가는데 필요한 많은 지혜를 알려주신 장지현 교수님에게 다시한번 감사의 말씀을 드리며 평생 잊지 않고 살도록 하겠습니다.

마지막으로 누구보다 저를 믿고 지지해 주셨던 아버지, 어머니 그리고 동생에게 감사하다는 말을 하고 싶습니다. 특히 박사학위를 한다는 핑계로 그동안 제 동생 정용이에게 너무 많은 짐을 떠넘겼던 거 같아 정말 미안하고 그동안 고생 많았다는 말을 전하고 싶습니다. 저는 이제 박사학위를 끝내고 이제 새로운 출발을 하려고 합니다. 제가 선택한길이 언젠가는 후회가 될 수 있겠지만 그건 어떤 선택을 하던 똑같은 거라 생각합니다. 그래서 제가 한 선택들이 최대한 후회가 되지 않도록 다시한번 정말 열심히 살아볼 예정입니다. 나중에 모든 분들과 웃으며 다시 만날 수 있는 그날이 올때까지 저는 최선을 다하며 나아가보도록 하겠습니다.

다시한번 학위를 마칠 수 있게 도와주신 많은 분들께 진심으로 감사의 말씀을 드립니다.